

# TESIS DOCTORALES

INSTITUTO ESPAÑOL  
DE OCEANOGRAFÍA

## Vertical velocities at an ocean front

Pedro Joaquín Vélez Belchí

Centro Oceanográfico de Canarias  
INSTITUTO ESPAÑOL DE OCEANOGRAFÍA  
Avenida Tres de Mayo, 73. E-38005 Santa Cruz de Tenerife, España  
Correo electrónico: [pedro.velez@ca.ieo.es](mailto:pedro.velez@ca.ieo.es)

*Recibido en marzo de 2007. Aceptado en febrero de 2008*





**UNIVERSIDAD DE LAS  
ISLAS BALEARES**

DEPARTAMENTO DE FÍSICA

**TESIS DOCTORAL**

---

**VERTICAL VELOCITIES AT  
AN OCEAN FRONT**

---

**PEDRO JOAQUÍN VÉLEZ BELCHÍ**

PALMA DE MALLORCA, 2006



**UNIVERSIDAD DE LAS  
ISLAS BALEARES**

DEPARTAMENTO DE FÍSICA

---

## **VERTICAL VELOCITIES AT AN OCEAN FRONT**

---

MEMORIA PRESENTADA EL 15 DE DICIEMBRE DE 2005 AL DEPARTAMENTO DE FÍSICA DE LA UNIVERSIDAD DE LAS ISLAS BALEARES PARA OPTAR AL TÍTULO DE DOCTOR EN FÍSICA, Y DEFENDIDA EL 26 ABRIL DE 2006 CON CALIFICACIÓN DE EXCELENTE *CUM LAUDE*.

REALIZADA EN EL IMEDEA (CSIC-UIB) POR:

**PEDRO JOAQUÍN VÉLEZ BELCHÍ**

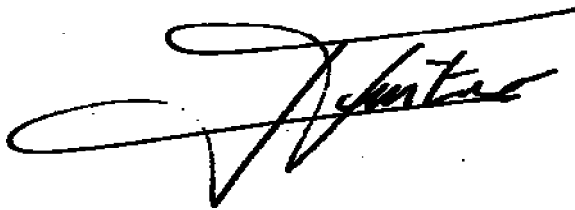
Y DIRIGIDA POR:

DR. D. JOAQUÍN TINTORÉ SUBIRANA, PROFESOR DE INVESTIGACIÓN DEL  
CONSEJO SUPERIOR DE INVESTIGACIONES CIENTÍFICAS

PALMA DE MALLORCA, 2006

D. Joaquín Tintoré Subirana, Profesor de Investigación del Instituto Mediterráneo de Estudios Avanzados (CSIC-UIB),

**CERTIFICA:** que la presente memoria, titulada "**Vertical Velocities at an ocean front**", y presentada por D. Pedro Joaquín Vélez Belchí al Departamento de Física de la Universidad de las Islas Baleares para obtener el título de Doctor, ha sido realizada bajo su dirección.



Fdo. Joaquín Tintoré Subirana

En Palma de Mallorca, a 15 de Diciembre de 2005



A BELÉN Y ABRIL,  
A MIS PADRES Y HERMANOS,  
SIN CUYO APOYO  
NUNCA HUBIESE ACABADO  
ESTA TESIS



LANZA PRIMERO TU CORAZÓN  
Y TU CABALLO SALTARÁ EL OBSTÁCULO.  
MUCHOS DESFALLECEN ANTE EL OBSTÁCULO,  
SON LOS QUE NO HAN LANZADO  
PRIMERO EL CORAZÓN.

*Noel Clarasó*



## AGRADECIMIENTOS

A quien primero quiero agradecer su tiempo, paciencia y dedicación es a Joaquín Tintoré, ya que él, conjuntamente con una serie de circunstancias, hizo que convirtiera el Mar en mi pasión, y más tarde en mi trabajo. Su confianza en mí, hizo también posible que acabara esta tesis. De los años que viví en Baleares tengo la amistad de Alberto Álvarez, Benjamín Casas, Fabrice Ardhuin, Jean Micheal Pinot, Marga Riera, Vicente Fernández y Ananda Pascual, que convirtieron aquellos años en una época inolvidable, y a quien agradezco igualmente su paciencia y apoyo. No puedo dejar de dar las gracias a Romualdo Romero, de la Universidad de las Islas Baleares, por las, casi en el olvido, discusiones sobre la dinámica cuasi-geostrófica y la evolución en latitudes medias; y a Damià Gomis, por compartir sus conocimientos en el campo del análisis objetivo.

From the other side of the Atlantic, I would specially like to thanks Bob Haney for having always time for a scientific discussion, about any topic, the mechanisms of the thermohaline circulation, ocean modeling, mesoscale dynamics, ... but also for being, together with his wife Olivera, my family during the very good times I lived in the States. From those times, I would also like to thanks Kurt, for his English lessons and Dan Eleuterio for his friendship and hospitality.

Thanks John Allen for your time during the many discussions we had about the quasigeostrophic and semigeostrophic theories, as well as for the great amount of patience during my first summer in UK, including Stonehenge.

A quien debo mucho de lo que hace falta, y se necesita para escribir una tesis, y que por tanto agradezco, es a mis compañeros y amigos Federico López, Cesar González-Pola, José Luís López-Jurado, José Antonio Cordero, Pepe González, Rosa Delgado de Molina, Javier Fariña, Carlos García, Santiago Marrero, Ángeles Rodríguez, Manolo Vargas, Gregorio Parrilla, Alberto García, Xisco Alemany,... que hacen del Instituto Español de Oceanografía un excelente lugar para trabajar.

También quiero dar las gracias a todo el equipo que trabajó en el proyecto Omega, y bajo el cual se recopilaron los datos que he usado para elaborar las conclusiones aquí expuestas, entre ellos David Smeed, Nick Crisp, ...

Y por supuesto, a la/s persona/s que desde el Ministerio de Educación me adjudicaron la beca FPI con la que inicié mis andanzas por este mundillo, donde ni siquiera me hubiera asomado si Teo Roca no me hubiera orientado.

Durante el largo proceso de elaboración de los resultados presentados en esta tesis han sido innumerables las personas que han contribuido, con su buen hacer, a que de una manera u otra, esta aventura llegara a buen puerto, pero nombrarlas aquí requeriría casi los mismos capítulos que esta tesis, de modo que los mantendré en mi recuerdo.

Pero sin lugar a dudas, quienes han sido, y son, imprescindibles son mis padres, Juani y Joaquín, mis hermanos, Cesar, Irma y Lara; así como Belén Peyró y Abril Peyró. A todos ellos simplemente les agradezco estar, incondicionalmente, en todo momento.

## Contents

<i>Abstract and keywords</i>	12
<b>Resumen y palabras clave</b>	13
<b>A. Introduction</b>	14
<b>A.1 Dataset</b>	25
<b>A.1.1 Satellite imagery and sea level data</b>	25
<b>A.1.2 Hydrographic data</b>	28
<b>A.1.3 Float dat</b>	29
<b>B. Hydrographic conditions of an intense oceanic front: the western Alborán Sea</b>	31
<b>B.0 Abstract</b>	32
<b>B.1 Introduction</b>	33
<b>B.2 Circulation and waters masses in the western Alborán Sea</b>	36
<b>B.2.1 Initial conditions</b>	36
<b>B.2.2 WAG migration</b>	44
<b>B.2.3 Presence of North Atlantic Central Waters</b>	51
<b>B.2.4 Float data</b>	55
<b>B.2.5 Sea level and pressure changes</b>	57
<b>B.3 Discussion</b>	60
<b>B.4 Conclusions</b>	61
<b>C. Analysis methods</b>	63
<b>C.0 Abstract</b>	64
<b>C.1 Introduction</b>	65
<b>C.2 Optimal statistical interpolation formulation</b>	67
<b>C.2.1 Scale selection</b>	71
<b>C.2.2 Parameters used in optimal interpolation throughout this study</b>	72
<b>C.3 Sensitivity study</b>	77
<b>C.4 Conclusion</b>	89
<b>D. Three-dimensional circulation associated with an intense oceanic front: the western Alborán Sea</b>	92
<b>D.0 Abstract</b>	93
<b>D.1 Introduction</b>	94
<b>D.2 Two dimensional circulation and vorticity</b>	94

<b>D.3 Vertical velocity</b>	102
<b>D.3.1 Omega equation</b>	102
<b>D.3.1.1 First survey</b>	106
<b>D.3.1.2 Time evolution of the vertical velocity field</b>	109
<b>D.3.2 Digital filtering initialization</b>	114
<b>D.3.2.1 Boundary conditions</b>	114
<b>D.3.2.2 Spin up</b>	118
<b>D.3.2.3 Results</b>	119
<b>D.4 Three-dimensional circulation</b>	121
<b>D.5 Discussion and conclusions</b>	125
<b>E. Lagrangian vertical velocity data</b>	128
<b>E.0 Abstract</b>	129
<b>E.1 Introduction</b>	130
<b>E.2 Results</b>	132
<b>E.2.1 General description</b>	132
<b>E.2.2 Comparison between the measured and diagnosed vertical velocity</b>	138
<b>E.3 Conclusions</b>	142
<b>F. Conclusions</b>	144
<b>List of tables and figures</b>	150
<b>References</b>	153

## Abstract and keywords

Mesoscale features are crucial to understanding marine ecosystems, given that the associated motions determine upper-ocean biogeochemical fluxes. To estimate these fluxes correctly, as well as the relative importance of the various processes involved, ageostrophic velocities, including vertical velocity, which connects the deep ocean to the upper layer, should be accurately determined. Unfortunately, ageostrophic velocities cannot be directly measured, and therefore indirect methods must be used.

The aim of the present doctoral thesis is to establish estimates of the vertical velocities associated with intense mesoscale features, considering their evolution over time and ascertaining the degree of validity of the method most commonly used to diagnose, from routine CTD and ADCP data, vertical motion at mesoscale: the Q-vector form of the quasi-geostrophic omega equation. The study has been carried out in the western Alborán Sea, an ideal place to study mesoscale processes, since the convergence between Mediterranean and Atlantic water masses found in the area gives rise to intense density fronts and energetic mesoscale features, such as two semi-permanent anticyclonic vortices: the western and the eastern Alborán gyres. The intense density front is present in the upper 200 dbar, accompanied by gradients of up to  $2\sigma_t$  in 20 km, whereas the associated velocity jet reaches velocities up to 120 cm/s. In this energetic area, the vertical motion obtained, mainly a consequence of the differential advection of vorticity, ranged between 60 m/day and  $-100$  m/day. To address the uncertainty of the computed vertical motion associated with the aliasing of unresolved scales, a sensitivity study of the computed fields to changes in the parameters of the objective analysis was carried out. This sensitivity study showed that the diagnosis presents large uncertainties related to the aliasing of unresolved scales, very important in those cases where the areas of highest advection of vorticity are at the boundaries of the sampled domain. Comparison between the two techniques used to obtain vertical velocities, the Q-vector form of the quasi-geostrophic omega equation and a digital filtering initialization of a primitive equation model, provided an estimate of the error due to the theoretical approach, with differences around 7 m/day, smaller than the uncertainty due to the sampling and observational errors. The fields determined are consistent with the first direct Lagrangian observations of vertical velocity ever done at mesoscale. The correspondence between the diagnosed fields and the estimates from the quasi-isopycnal floats shows that the diagnosed fields give the correct order of magnitude of the vertical motion, and similar spatial and temporal scales for the upwelling and downwelling patches.

The most significant result obtained is that the Q-vector form of the omega equation makes it possible to ascertain correctly, from routinely observed density fields, the sign, order of magnitude, and size of the upwelling and downwelling patches. However, derived magnitudes, such as biogeochemical fluxes, should be interpreted very carefully, since the uncertainty in the diagnosed vertical velocities, due to the aliasing of the unresolved scales, could be critical in some cases.

**Keywords:** Marine ecosystems, mesoscale, vertical velocity, Alborán Sea, ocean fronts, eddies, upwelling, upper ocean, fertilization, baroclinic motion, water masses, vorticity, advection, omega equation, euphotic layer.

## Resumen y palabras clave

### Velocidades verticales en un frente oceánico

La comprensión de los ecosistemas marinos requiere conocer el papel que desempeñan las estructuras oceánicas de mesoescala, como frentes, meandros, remolinos y filamentos, ya que los movimientos asociados a ellas ejercen una influencia clave en los flujos biogeoquímicos de la capa superficial oceánica. Para evaluar correctamente estos flujos es necesario determinar las velocidades ageostróficas, y en particular la componente vertical de las mismas, que conecta el océano profundo con la capa eufótica.

El propósito de esta tesis es estimar las velocidades verticales asociadas a estructuras de mesoescala atendiendo a su evolución temporal y evaluar la validez de la ecuación omega en su formulación con el vector  $Q$ , comúnmente usada para la determinación de velocidades verticales a partir de datos obtenidos en campañas oceanográficas. Las velocidades verticales se han obtenido recurriendo a dos técnicas: el uso de la ecuación cuasi-geostrófica omega en su formulación con el vector  $Q$  y la aplicación de un filtrado digital a los campos de densidad asimilados a un modelo numérico de ecuaciones primitivas. Ambos métodos se han empleado en el mar de Alborán, emplazamiento idóneo para el estudio de procesos de mesoescala. En esta energética zona, caracterizada por un frente en densidad observado en los primeros 200 dbar que alcanza gradientes de hasta  $2\sigma_t$  en 20 km y comporta una corriente asociada que adquiere velocidades superiores a los 120 cm/s, el movimiento vertical (principalmente relacionado con la advección diferencial de vorticidad) registró valores comprendidos entre  $-100$  m/día y  $60$  m/día. El impacto que las escalas espaciotemporales no resueltas producen en los campos de velocidad vertical ha sido investigado evaluando la sensibilidad que demuestran los campos diagnosticados frente a cambios en las variables del análisis objetivo, encontrándose que la incertidumbre asociada a las escalas no resueltas es mayor que el error debido a la aproximación teórica, estimado en cerca de  $7$  m/día y obtenido de la comparación entre los respectivos campos derivados de la ecuación omega y del filtrado digital. Los resultados muestran que los métodos de diagnóstico originan grandes incertidumbres asociadas a las escalas no resueltas, críticas cuando las áreas de advección de vorticidad se encuentran en los bordes del dominio muestreado. Las comparaciones realizadas entre los campos de velocidad vertical determinados a partir de la ecuación omega y de las medidas directas obtenidas con boyas lagrangianas revelan que las escalas espaciotemporales de ambos son similares y con el orden de magnitud correcto. El resultado más significativo indica que la ecuación omega en su formulación con el vector  $Q$  permite determinar fielmente, a partir de los campos de densidad, el orden de magnitud y el signo de la velocidad vertical, así como las escalas espacio-temporales que caracterizan las zonas de afloramiento y surgimiento. Sin embargo, las magnitudes derivadas de la velocidad vertical, como los flujos biogeoquímicos, deben ser interpretadas con extrema cautela, ya que la incertidumbre que origina la alteración producida por las escalas espacio-temporales no resueltas puede ser crítica.

**Palabras clave:** Ecosistemas marinos, mesoescala, velocidad vertical, mar de Alborán, frentes oceánicos, afloramiento, remolinos, fertilización, movimiento baroclino, masas de agua, vorticidad, advección, ecuación omega, mar Mediterráneo, capa eufótica.



---

## **A.-INTRODUCTION**

---

**D**riven by the sun radiation and its asymmetrical distribution on the earth surface, the ocean and the atmosphere work as a large heat engine that dissipates the zonal available potential energy created by the differential solar heating of the Earth's surface. Thus, the imbalances created by the sun, warming more the tropics than the poles, and manifested through density differences, are removed by the gravitational force but constrained by the effects of the earth's rotation. The available potential energy  $[A_z]$  is transformed into eddy available potential energy  $[A_E]$ , and then converted to eddy kinetic energy  $[K_E]$ , to be finally lost by friction  $[D_E]$ . The conversions  $[A_z, A_E]$  and  $[A_E, K_E]$  represent the baroclinic processes and constitute the principal route for the energy conversions in both the ocean and the atmosphere. This conversion occurs when waves situated within a meridional temperature gradient move warm air or water poleward and cold air or water equatorward. The available zonal potential energy also contributes, in a much lesser extent, to the kinetic energy of the zonal flow  $[K_z]$ , consequently, frictional losses by the zonal flow are relatively small  $[D_z]$ . The conversion between zonal and eddy kinetic energy  $[K_z, K_E]$ , by means of barotropic instability, is a minor component in the atmosphere/ocean heat engine.

The physical mechanism that transforms the available potential energy into eddy kinetic energy is called baroclinic instability and is displayed through the generation of eddies, either cyclonic or anticyclonic. In the atmosphere, the critical scale where this conversion occurs is the internal deformation radius, where the force due to the pressure gradient and the Coriolis force are nearly in balance. This scale is likewise referred by the meteorologist as the synoptic scale, since it includes the mid-latitude cyclones and anticyclones, which are the major features of the daily weather maps, and therefore have been widely studied in the atmosphere [Carlson, 1991; Peixoto and Oort, 1992].

In the ocean, the critical scale where the  $[A_z, A_E]$  and  $[A_E, K_E]$  conversions occurs, and where baroclinic instability exists, is the internal Rossby deformation radius, it is called the mesoscale, the ocean analogous to the atmospheric synoptic scale.

The variability at the oceanic mesoscale goes from tens to hundreds of kilometers and from weeks to months and is known as the oceanic weather. It develops more energy than any other movement in the ocean. Among the mesoscale features are fronts, eddies, meanders, filaments, etc [Gill, 1982]. Fronts, in general, are boundaries between different water masses, thereby characterized by large density gradients, and by high along front geostrophic currents. Fronts and eddies in the ocean are intimately related: eddies are produced at fronts, by baroclinic or barotropic instability, while the deformation fields associated with eddies can lead to frontogenesis.

The characteristic spatial and temporal scales for the oceanic mesoscale motions, the Rossby radius, match typical open ocean ecosystem scales, suggesting that mesoscale oceanic features have an important role in regulating biogeochemical cycles in the upper ocean ecosystems [Strass, 1992; Siegel *et al.*, 1999]. In a biological sense, the deep and the upper ocean can be considered complementary; in the ocean upper layer the presence of light permits life, while the deep layers are usually rich in nutrients. Phytoplankton requires nutrients, for grow and development, in the euphotic layer, where photosynthesis is possible. The relevance of the circulation at mesoscale in ecosystem dynamics comes from the fact that they connect the deep ocean to the upper layer. At mesoscale, currents are in nearly hydrostatic balance and almost geostrophic in their momentum balance, some simple scaling arguments state that these currents are predominantly horizontally with little connection between the upper and the deep ocean. However, the fast spatial and temporal variability associated with mesoscale currents create divergence and convergence and consequently intense vertical motions. These vertical motions, part of the ageostrophic circulation, are the necessary requirement to ensure that the changes in the density field during time evolution keep the thermal wind balance valid, keeping small the deviations from the

geostrophic balance [Gill, 1982; Carlson, 1991; Peixoto and Oort, 1992]. Vertical velocities in the ocean are mostly associated either with the existence of a non-transient atmospheric wind forcing, the well-known upwelling areas, or with the presence of mesoscale features. The vertical velocities found at mesoscale are of the order of several tens of meters per day, an order of magnitude higher than the highest vertical velocities usually observed in upwelling areas.

Except some small areas, the open ocean can be considered as a biological desert [Williams and Follows, 1998], and explaining the observed levels of phytoplankton primary production in the nutrient-poor parts of the oceans with the traditional interpretations, vertical diffusion, atmospheric inputs of nitrogen, and lateral input of nitrate from upwelling regions is unconvincing. However, the upward pumping of nutrients by the action of mesoscale structures could sustain part of the observed levels of primary production in nutrient-poor parts of the ocean. Although there is controversial about the relative importance of the various mechanism involved due to the differences in the structure and in the methods for calculating the fluxes of nutrients [Oschlies and Garcon, 1998; McGillicuddy et al., 1998; Williams and Follows, 1998]. Probability due to the inability to estimate correctly the fluxes associated with single mesoscale features [Martin and Richards, 2001], or by the fact that mesoscale is not fully resolved in large-scale biogeochemical models and significant vertical flux of nitrate may currently be missed due to the inability to resolve sub-mesoscale upwelling [Martin and Pondaven, 2003]. Concentration onto the euphotic zone associated with mesoscale eddies and fronts has also been demonstrated [Bakun, 1996; Vélez-Belchí et al., 2002]. Mesoscale processes are also crucial to understand ocean dynamics, since the departures from the geostrophic balance are the first forcing in ocean dynamics time-evolution and the associated transport of heat and freshwater have large impact on the large scale circulation.

In spite of the importance of the ageostrophic circulation and its vertical component it cannot be directly measured because the resolution of shipboard ADCPs is lower than

1 cm/s while the stronger mesoscale ageostrophic velocities are one order of magnitude smaller.

Estimations of vertical velocities can be obtained using pressure records from isopycnal floats; however, these measurements are not available in routine hydrographic studies. Therefore, indirect methods for estimating the ageostrophic secondary circulation from observed fields are needed. The quasi-geostrophic (QG) theory gives the possibility of estimating vertical velocity from density data [*Hoskins et al.*, 1978; *Hoskins et al.*, 1985a; *Holton*, 1992]. In such theoretical framework the slow evolution of mesoscale features is driven by the geostrophic advection of density and momentum. This advection modifies the initial fields and the geostrophic and hydrostatic balance could be violated. However, the ocean at scales larger than the Rossby radius is almost in geostrophic and hydrostatic balance and the density field must be modified through the vertical velocity field to ensure that the changes in the density during the time evolution of the mesoscale features keep the thermal balance valid.

Vertical velocities diagnosed with this theoretical approach have been used to study many ocean and ecosystem processes. *Leach* [1987] solved a two dimensional version of the omega equation to estimate vertical motions and found that the patterns of sinking and rising motions were those characteristic of a unstable baroclinic wave, accompanied by maximum values in the range  $\pm 2$  m/day.

During the last fifteen years the QG formulation has been used by several authors in different regions of the world's ocean. In the Alborán Sea *Tintoré et al.* [1991], using an objective analysis technique for quantitative scale separation, were the first to found that the magnitude of vertical motions depends on the horizontal scale of the instabilities, showing that the vertical motion associated with the mesoscale eddies is an order of magnitude higher than the vertical motion associated with the large-scale structure. *Pollard and Regier* [1992], with data sampled at the Sargasso Sea, southwest of Bermuda, solved a two dimensional (latitude-pressure plane) version of

the omega equation; they found vertical velocities up to 40 m/day with net diffusion of properties across the thermocline. In the North Atlantic intergyre front, *Fiekas et al.* [1994] found that vertical velocities up to 5 m/day appeared as the signature of secondary instabilities. The cells of alternative upwelling and downwelling, associated with the subsidiary ridges and troughs along the jet, were arranged in the classical signature of baroclinic instability and therefore ascertained that the vertical velocity permitted to understand the incipiently unstable character of the large-scale. In the Channel of Ibiza, Western Mediterranean Sea, *Pinot et al.* [1995] quantified the three-dimensional circulation of an eddy/front system with the quasi-geostrophic omega equation; they found vertical velocities up to 4 m/day, forced by the curvature induced by an eddy adjacent to a front. The authors evidenced the impact of mesoscale frontal upwelling on the fertilization of the surface layer. In the western Alborán Sea, *Viúdez et al.* [1996b] used the quasi-geostrophic omega equation to obtain vertical velocities, 20 m/day, mainly associated with mesoscale features. The authors validated the results with potential vorticity conservation, hypothesizing that the ageostrophic circulation was necessary for the maintenance of the large gyres found in the Alborán Sea. *Rudnick* [1996] solved, in the Azores Front, a version of the omega equation where stratification was allowed to vary horizontally; establishing that there was tendency for the dense water at the north of the front to be downwelled, while the warmer water at the south was upwelled. The computed vertical heat fluxes, with warming of the upper water column and cooling beneath, indicated that the vertical circulation tended to stratify the upper ocean. In the Iceland-Færoes front, *Allen and Smeed* [1996a] computed, using data from two high-resolution surveys, vertical velocities using the Q-vector form of the omega equation, elucidating the behavior of an eddy that propagated northeastward with strong vertical velocities, up to 100 m/day, ahead and behind the vortex. To describe the three-dimensional circulation associated to the mesoscale motions in the California current *Shearman et al.* [1999] used the Q-vector form of the omega equation, finding maximum vertical speeds of 45 m/day. The  $w$  field was characterized

by a large-scale pattern due to the cyclonic meander and by smaller upwelling and downwelling cells aligned along the core of the jet and associated with its meanders. The three-dimensional trajectories of water parcels along geostrophic streamlines, accompanied by net vertical velocities of 7-15 m/day, had maximum vertical velocities in the regions of maximum change in relative vorticity, an indication of potential vorticity conservation. To study the supply of nutrients into the euphotic zone *Martin and Richards* [2001] calculated vertical velocities in an eddy at the Northeast Atlantic, demonstrating that the ageostrophic upwelling due to perturbations in the rim of an eddy, in addition to the wind-induced Ekman pumping, produced significant flux of deep nutrients into the surface waters of the eddy. These authors realized, by the first time, that the sampling imposed strong uncertainties in the ascertainment of the vertical motion and therefore on the net vertical nutrient fluxes. The importance of the secondary ageostrophic circulation in understanding the subduction at the Antarctic Polar Front was established by *Garabato et al.* [2001], who determined vertical velocities using the omega equation. The relationship between the mesoscale vertical motion and the slope of the size-abundance spectrum of phytoplankton in a frontal ecosystem was studied by *Rodriguez et al.*, [2001] with vertical velocity diagnosed using the omega equation. *Pascual et al.* [2004], at the Palamos Canyon, northwestern Mediterranean Sea, estimated vertical velocities up to 10 m/day that were used to explain the propagating character of the meanders found at the Palamos Canyon. The importance of synopticity in the uncertainty of the computed  $w$  was also stated by these authors.

The reliability of the omega equation, as a method for estimating vertical velocities from density data and hence the reliability of biogeochemical fluxes computed making use of the vertical velocities determined from the omega equation was firstly analyzed, with model simulations, in the works of *Pinot* [1996] and *Strass* [1994]. These authors found that the Q-vector version of the omega equation was able to resemble the vertical

velocity field obtained from model simulations. However, it should be reminded that models do not have the continuum spectrum which includes all the spatial-scales found in the real ocean and therefore the observational error that includes the aliasing by unresolved scales was not fully taken into account in these studies. For that reason it is still necessary to study the influence of non-sampled scales in the determination of vertical velocities, problem that arise when the sampling is carried out in the true ocean, where the continuum of spatial scales is found.

Besides the QG formulation, several methods have been used to compute vertical velocities. A dynamical method for initializing a primitive equations model was firstly used by *Viúdez et al.* [1996a] in the Alborán Sea. The vertical velocities estimated using this density dynamical assimilation showed reduced magnitude, although similar patterns to those obtained via the QG approach. The reduced magnitude in the QG computations was explained in terms of the limitations of the QG theory, mostly the lack of ageostrophic advection of geostrophic vorticity and geostrophic advection of ageostrophic vorticity. In a filament associated with the California current, in the California coastal transition zone, *Haney and Hale* [2001] demonstrated the use of dynamical assimilation into a primitive equation model as a plausible alternative to QG determination in mesoscale dynamics. Several different methods to calculate vertical velocities were used by *Shearman et al.* [2000] in a cyclonic jet meander of the California current: the Q-vector of the quasi-geostrophic omega equations, two equations derived from iterated geostrophic intermediate models, an omega equation derived from balance equations and assimilation into a primitive equation model. All methods yield similar patterns and scales for the vertical velocity fields, but showed reduced magnitude if compared with the quasi-geostrophic estimations. The horizontal velocities diagnosed from the intermediate models showed also differences in magnitude, demonstrating the importance of the gradient wind balance in flows having strong curvature.



To address the importance of mesoscale processes in marine ecosystem and in the air-sea interaction, identifying the relative importance of the various processes involved, it is necessary to have accurate vertical advective biogeochemical fluxes and, therefore, accurate vertical velocities with its associated uncertainties. The first statement about the influence of the uncertainties in the vertical velocity, on second step calculations as biogeochemical fluxes was pointed out in a study carried out by with data sampled on an eddy at the North Atlantic by *Martin and Richards* [2001]. These authors recognized that the track spacing of the survey precludes an exact calculation of streamline distortion for the sampled eddy and hence all that could really be done was to produce broad estimation of the likely vertical velocities and thus of the nutrient fluxes. The first tentative to estimate the uncertainty in vertical velocities determined by indirect methods was recently done by *Gomis et al.* [2005]. These authors carried out a theoretical and numerical study of the accuracy of the dynamical fields inferred from one of the high-resolution hydrographic surveys carried out in the western Alborán Sea. For the vertical velocity the fractional error (ratio of the total rms error to the standard deviation of the anomaly field) is between 6%-10% in a small inner domain, exceeding 20% half a way between the centre of the domain and the lateral boundaries. The importance of the error associated with non-synoptic surveys was addressed by *Gomis and Pedder* [2005], they found that the along-front sampling, in slow propagating waves, resulted in fractional error of about 15% for dynamic height and more than 50% for relative vorticity and vertical velocity. These studies should be considered as lower bounds for the observational and sampling error, since the authors assumed a precise knowledge of the correlation model and of the mean.

In spite of the need of accurate estimates of vertical velocity, there is only one comparison of diagnosed vertical velocities and in-situ direct measurements. In that study, carried out by *Lindstrom and Watts* [1994], vertical velocities obtained by three methods were compared: time derivatives of pressure records from isopycnal floats;

the quasi-geostrophic heat equation applied to temperature changes from moored currentmeters; and the quasi-geostrophic vorticity applied to a time-evolving stream function obtained from inverted echo sounder data. The authors found good agreement between the three methods, especially at scales longer than 16 days. To determinate  $w$ , the omega equation was not used, instead the authors used the quasi-geostrophic equation of heat and vorticity given that the dataset comprised time evolving fields that were collected within an intensive multi-institutional study that lasted two years and hence provided an exhaustive time and space coverage for the different estimations of  $w$  that routine CTD/SeaSoar surveys do not provide.

The uncertainty in the estimations of vertical velocities at an ocean front, and the validity of the estimated vertical velocity fields for further calculations as biogeochemical fluxes is still an open question. Accordingly, the purpose of this thesis is to establish estimates of the vertical velocities associated with intense mesoscale features, attending to its time evolution and ascertaining the degree of validity of the most common method used to diagnose, from routine CTD and ADCP data, vertical motion at mesoscale, the Q-vector form of the quasi-geostrophic omega equation. These questions are approached throughout the following stages. First, to understand the dynamical situation found, and its importance for establishing strong secondary circulation, a hydrographic description of the surveys is included. Second, the influence of the unresolved scales onto the computation of the vertical velocities is investigated by means of a sensitivity study of the computed vertical velocities to changes in the objective analysis parameters. Third, the vertical velocity is diagnosed, describing the spatial and temporal variability of the dynamical situation found, including the three dimensional circulation, thanks to the four consecutive surveys available. Fourth, the uncertainty due to the theoretical approach is explored analyzing the differences between two techniques used to obtain the vertical velocity field, the quasi-geostrophic omega equation and an assimilation into a primitive equation ocean model. Finally, the

previous steps are completed with the comparison between the vertical motion diagnosed and measurements of the true vertical motion obtained using quasi-isopycnal lagrangian floats.

The study has been carried out with data obtained in the Western Alborán Sea, given that this area is a very appropriated place to study ageostrophic secondary circulation since in there two quite different waters masses are found, the denser Mediterranean waters and the lighter Atlantic waters. They met in an intense frontal region, populated with mesoscale features, which include, among others, two anticyclonic quasi-permanent vortices: the western Alborán gyre (WAG) and the eastern Alborán gyre (EAG).

To meet the objectives, this thesis is organized as follows: the remainder of this chapter *A.-Introduction* is devoted to describe the data set, chapter *B.-Hydrographic conditions of an intense oceanic front: the Western Alborán Sea* presents the hydrographic description of the western Alborán Sea, emphasizing the different dynamical conditions found during the sampling and attending to its causes. Chapter *C.-Analysis methods* describes the results found in the sensitivity study carried out to find the impact of the unresolved scales on the estimated vertical motion. The vertical motion obtained from two different methods is described in chapter *D.-Three-dimensional circulation associated with an intense oceanic front: the Western Alborán Sea*, paying attention to its time evolution and to the three dimensional circulation. The physical mechanisms that produce the vertical velocities are analyzed, as well as the differences between both fields, explaining them in terms of the approximations under the QG theory. This chapter is essential to undertake the comparison with lagrangian in-situ data that is addressed in chapter *E.-Lagrangian vertical velocity data*. Finally, chapter *F.-Conclusions* review the conclusion presented in each chapter, relating them back to the thesis questions, and including ideas for future studies.

## A.1 DATASET

During the first two weeks of October 1996, a field experiment was carried out on board the Spanish R/V Hespérides in the western Alborán Sea (see table A.I). Sea surface temperature images were used to locate the region of interest: the northern edge of the western gyre in the Alborán Sea. The first small-scale survey was completed between the 1<sup>st</sup> and the 4<sup>th</sup> October. To resolve both the spatial and temporal variability of the upper 300 m, three small-scale surveys were carried out in the same area; survey 2: October 6<sup>th</sup>-9<sup>th</sup>; survey 3: October 9<sup>th</sup>-11<sup>th</sup> and survey 4: October 11<sup>th</sup>-14<sup>th</sup>. figure A.1 shows SST images of the Alborán Sea for each hydrographic survey, the WAG and the AJ are clearly identified.

Survey 1	1996 Oct 1 <sup>st</sup> , 17:30	1996 Oct 4 <sup>th</sup> , 13:45
Survey 2	1996 Oct 6 <sup>th</sup> , 20:15	1996 Oct 9 <sup>th</sup> , 01:35
Survey 3	1996 Oct 9 <sup>th</sup> , 07:00	1996 Oct 11 <sup>th</sup> , 11:28
Survey 4	1996 Oct 11 <sup>th</sup> , 16:48	1996 Oct 14 <sup>th</sup> , 20:15

**Table A.I.** Starting and ending dates for each survey

### A.1.1 Satellite imagery and sea level data

Daily sea surface temperature images were obtained from the German DLR agency between October 1<sup>st</sup> and December 1<sup>st</sup> 1996. The images are daily composites of NOAA multichannel scenes.

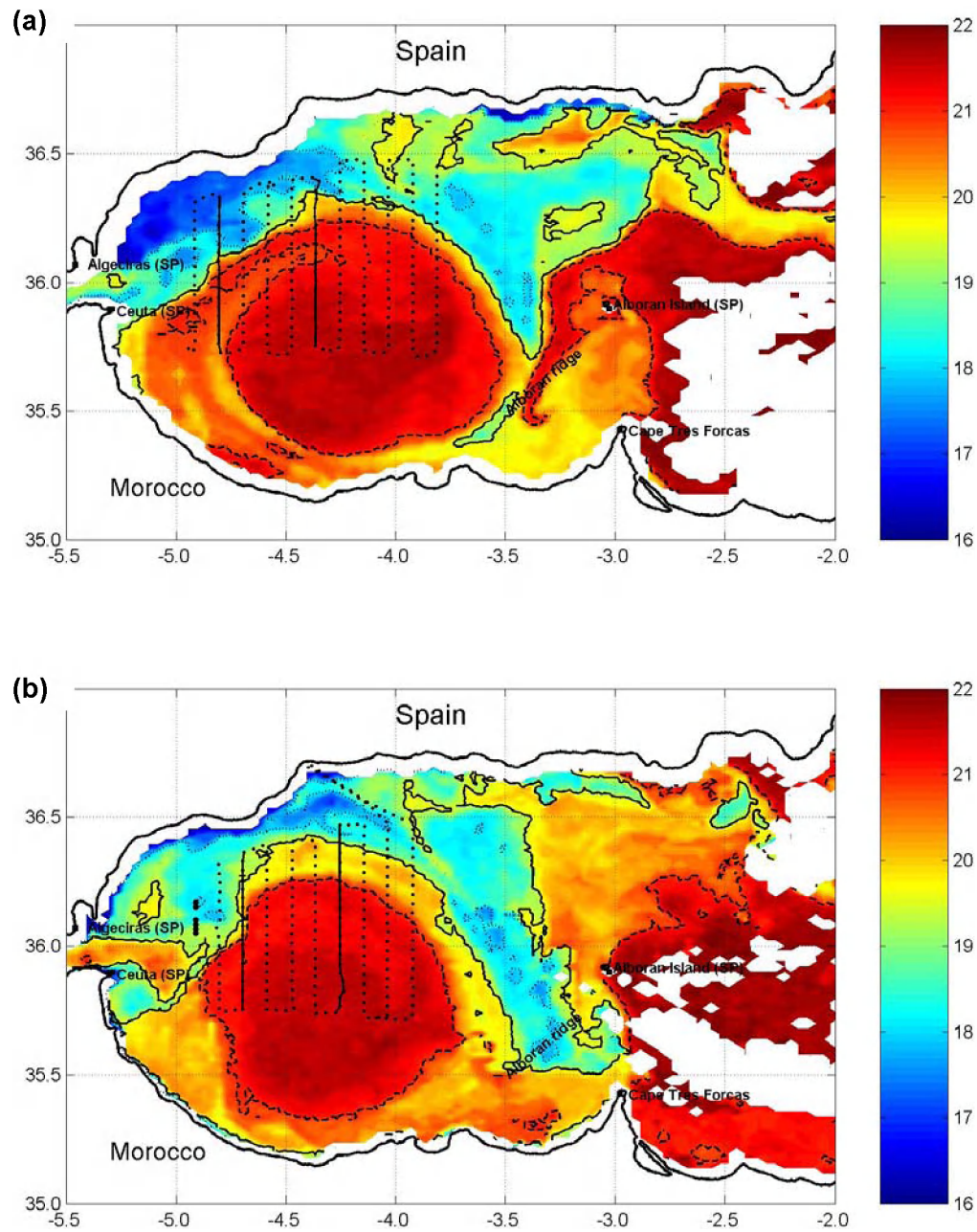


**Figure A.1.** Sea surface temperature (SST) for the western Alborán sea on the first day of (a) survey 1 (October 3<sup>rd</sup> 1996), (b) survey 2 (October 6<sup>th</sup> 1996), (c) survey 3 (October 9<sup>th</sup> 1996) and (d) survey 4 (October 11<sup>th</sup> 1996). The dotted contour corresponds to the 18°C isotherm, the thick contour to the 19.5°C isotherm and the dashed one to the 21°C. The track of each survey is overlaid. The circles in the westernmost section of survey 2 indicate the launching positions of the six recovered floats. The second (4.8°W) and sixth (4.36°W) sections, are indicated with a thicker line in surveys 1, 2 and 3. The geographical locations mentioned in the text are included.



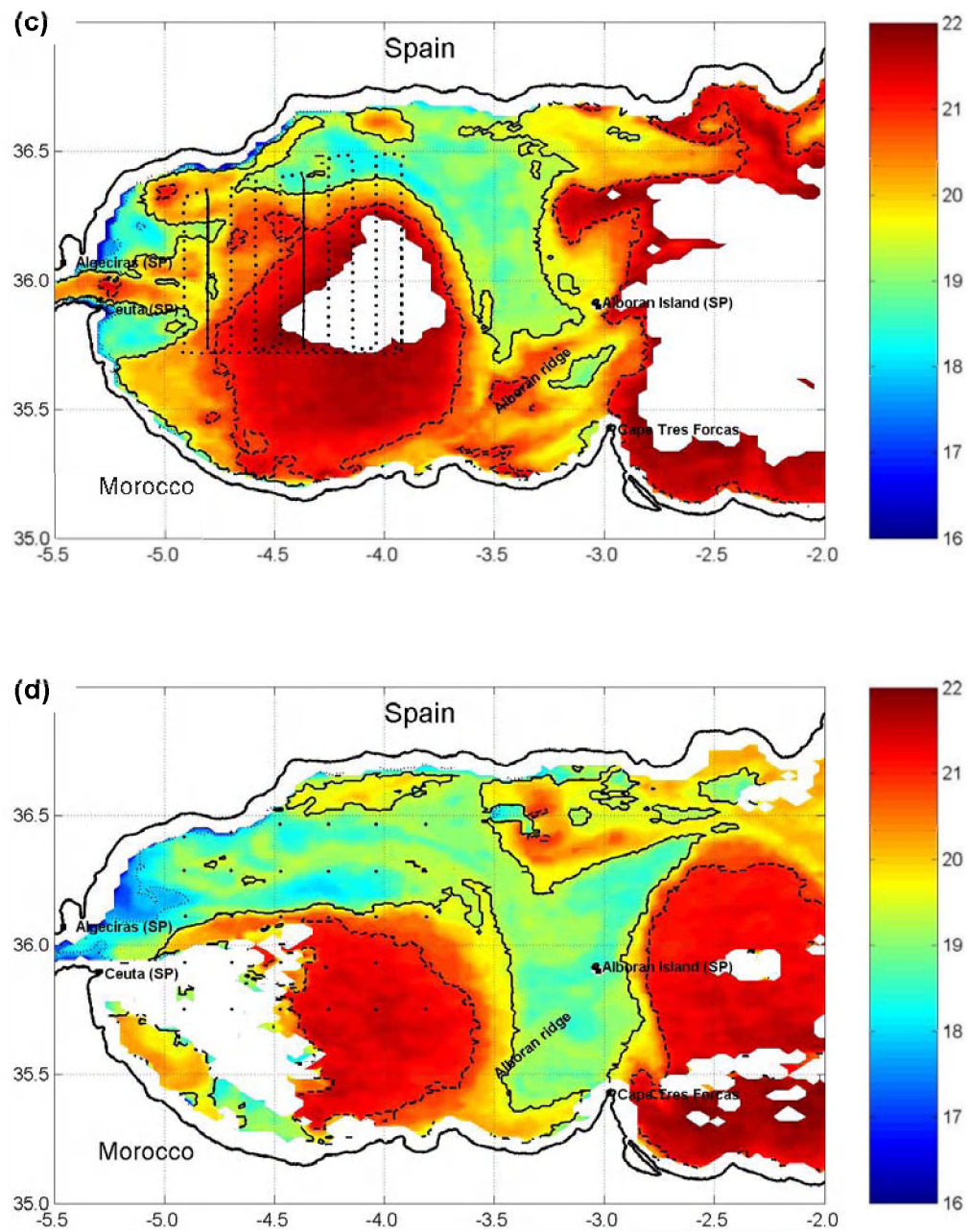


Figure A.1. (continued).

Hourly sea level data at Ceuta (south shore of the Gibraltar Strait) and Algeciras (north shore of the Gibraltar Strait) were obtained from the tidal network of the 'Instituto Español de Oceanografía'. To compute the sea level difference, the hourly data was filtered to eliminate the tidal signal, and sub-sampled in order to have daily values. Sea level pressure data at Ceuta were obtained from the 'Instituto Nacional de Meteorología'.

### **A.1.2 Hydrographic data**

The first three surveys were sampled using a SeaSoar, a towed undulating CTD system. The SeaSoar completed an undulation cycle from the surface down to 350 dbar every 8 km, at a speed of 8 knots. The raw CTD data were calibrated with the ship's thermosalinograph and with water samples taken at the surface. The calibrated data were averaged into 8 dbar vertical bins with an along-track resolution of 4 km. Each survey took less than three days to be complete and covered a rectangular area of about 80Km by 100 Km and centered at 4.4°W, 36°N. The SeaSoar surveys included 10/11 meridional sections 70/80 Km long and spaced 10 km in the zonal direction. The first and the third survey had 11 legs, but the second one only had nine since the legs at the eastern and western side were not run. The fourth survey consisted of a regular CTD grid with stations 20 km apart. The shipboard 150 kHz RDI ADCP was used throughout the cruises to determine accurately water velocity along the ship's track. The use of differential GPS navigation yielded a clear improvement in the absolute velocity vectors [Allen *et al.*, 1997]. Unfortunately, ADCP velocities are not available for the fourth survey. In order to compare Atlantic transports between the SeaSoar surveys we have chosen the section nearest to the strait common for the three surveys (see figure A.1). A complete description of the SeaSoar and ADCP data processing can be found in [Vélez-Belchí *et al.*, 1997; Allen *et al.*, 1997]. The dynamic height has been computed from the individual density profiles through the integration of the specific volume anomaly relative to 250 dbar. A depth between 200 dbar and 250 dbar has been commonly used in the Alborán Sea as the level of no motion [Lanoix,

1974; Perkins *et al.*, 1990], given that it separates the eastward flowing AW from the westward propagating MW. This assumption is adequate within the uncertainties of the ADCP velocities, as corroborated later in chapter B., where the ADCP velocities at 200 dbar for the first three surveys are shown (maximum non noisy-values are of the order of 2 cm/s). The geostrophic velocity has been calculated from the geostrophic balance equations, together with the assumption of no motion at 250 dbar.

$$\begin{aligned} f u_g &= -\frac{1}{\rho_0} \frac{\partial p}{\partial y} = -\frac{\partial \Phi}{\partial y} \\ f v_g &= \frac{1}{\rho_0} \frac{\partial p}{\partial x} = \frac{\partial \Phi}{\partial x} \end{aligned} \quad (1)$$

Considering the thermal wind equation (1) the geostrophic velocities were obtained, using centered finite differences, from the gridded geopotential field.

### A.1.3 Float data

In addition to the ship-based observations, ten neutrally buoyant lagrangian floats were deployed to provide direct estimates of vertical velocity, temperature, and pressure every 30 minutes. These floats register vertical excursion of isopycnals and any vertical motion of water parcels across isopycnals. They were ballasted to be at 100 dbar at the launching position, the depth where maximum vertical motion was expected. For such purpose, the densities of the floats were calibrated to be in equilibrium with the in-situ density at 100 dbar found during the Alborán92 cruise [Viúdez *et al.*, 1996b]. The mean drifting level for the floats was 108 dbar, with excursions from 73 dbar to 148 dbar. The floats were tracked by triangulation with the help of five subsurface acoustic sources moored in the Alborán Sea. On the evening of October 5<sup>th</sup> 1996, the floats were launched in the core of the Atlantic jet, along the meridian 4.88°W and a mile apart between 36.05°N and 36.18°N (figure A.1). After 40 days, the floats came to the surface and started to transmit through the ARGOS system. From the initial set just six were recovered, two floats (8 and 15) went ashore the Moroccan coast and the data were lost. The six floats recovered (00, 88, 97, 99, 11 and 10) were located 60 times



per day (every 24 minutes) measuring in-situ temperature, pressure and float rotation. Although the floats were not launched in clusters, right after the deployment the floats grouped in pairs, each pair following a similar trajectory. Floats 10 and 11 make up the first pair, 88 and 99 the second, and 00 and 97 the third one. The float data was filtered using a low-pass Godin filter  $(A_{60}^2 A_{61}) / (60^2 \cdot 61)$  [Emery and Thomson, 1998] to remove the semidiurnal signal, mainly tidal, from the 30-min data; the cut-off period for the filter used is 0.96 days.

---

**B.-HYDROGRAPHIC CONDITIONS  
OF AN INTENSE OCEANIC FRONT:  
THE WESTERN ALBORÁN SEA**

---

## B.0 ABSTRACT

In the Western Alborán Sea light, Atlantic waters and dense Mediterranean waters meet, giving rise to intense density fronts and energetic mesoscale features such as two semi-permanent anticyclonic vortices: the western and eastern Alborán gyres. The circulation in the Alborán Sea varies strongly in time, with episodes where neither the western Alborán gyre nor the eastern Alborán gyres are present. Here, we describe the three-dimensional structure and the dynamical conditions found in the western Alborán Sea during October 1996. During the first survey, the western Alborán Sea was occupied by the WAG, and surrounding it, the Atlantic jet; while the following surveys showed the WAG drifting eastward, beginning a WAG migration event, as confirmed fifteen days later by the lagrangian floats and the SST images. Associated with these hydrographic conditions there was a strong density front in the upper 200 dbar, with gradients up to  $2\sigma_t$  in 20 Km; whilst the velocity jet with velocities reached 120 cm/s. One month later a new gyre was formed to replace the old one. A change, between the first and the second survey, in the Atlantic inflow through the Strait of Gibraltar has been observed with the help of the ADCP velocities, SST images, and the TS properties of the sampled waters. The relationships between this change in the Atlantic inflow, a drop in the atmospheric pressure at Ceuta, the tidal regime and the WAG migration are also discussed. The existence of a high-resolution sampling in space, together with the possibility of addressing the temporal variability have allowed to describe, in detail and for the first time, the time evolution of the three dimensional thermohaline structure of the Western Alborán Sea during a WAG migration event, relating the migration to changes in the inflow through the Strait of Gibraltar. Moreover, the strong dynamical conditions found in the western Alborán Sea establish favorable conditions to strong secondary ageostrophic circulation for high vertical velocities, as will be described in forthcoming chapters.

## B.1 INTRODUCTION

The Alborán Sea plays an important role in modulating the Atlantic waters along their path through the Mediterranean Sea, and thereby the overall circulation of the Mediterranean Sea, since the Alborán Sea is the westernmost Mediterranean sub-basin, connecting the Mediterranean Sea with the Atlantic Ocean through the Strait of Gibraltar. The large-scale dynamics of the Alborán Sea can be outlined as follows: the inflowing Atlantic waters form a wave-like front that extends from the Strait of Gibraltar to the Algerian coast [Lanoix, 1974; *Donde Va? Group*, 1984; *La Violette*, 1986; *Parrilla et al.*, 1986; *Tintoré et al.*, 1988; *La Violette*, 1990]. The Atlantic Jet (AJ), formed by Atlantic waters, and its associated density front separates the denser Mediterranean waters (MW) in the north from the lighter modified Atlantic waters (MAW) in the south. The southern modified Atlantic waters form the western Alborán gyre (WAG) and the eastern Alborán gyre (EAG), two anticyclonic vortices separated by the Alborán ridge [Viúdez *et al.*, 1996b]. Lanoix [1974] already described a well-developed WAG, while the eastern Alborán basin was occupied by an anticyclonic vortex. This work suggested the existence of a stable WAG and a more elusive EAG. However, *Herburn and La Violette* [1990] showed that both gyres had time variability. Several later studies confirmed that the general circulation scheme depicted above is far from being stable and undergoes variability at very different time and length scales. For instance, *Tintoré et al.* [1991] showed the existence of intense mesoscale variability along the rim of the WAG, with intense vertical motions associated with the strong density fronts found in the area [Viúdez *et al.*, 1996b; Vélez-Belchí and Tintoré, 2001]. *La Violette* [1984] described how sub-mesoscale features were advected along the path of the AJ, while *Lafuente et al.* [1998] described the advection of a mesoscale structure from the north of the basin to its southern part. Likewise, large-scale variability modifies the overall structure of the Alborán Sea, with episodes where neither the EAG nor the WAG are present. Events with strong impact on the large-scale circulation of the Alborán Sea are

the eastward WAG migrations. In these events, the WAG begins to drift eastward; without the high pressure of the WAG, the AJ turns to the right, following the Moroccan coastline, and developing a new WAG near of the strait. Meanwhile, the old WAG continues its eastward migration. In spite of the importance of these events on the large-scale variability of the western Alborán Sea, there are only two studies where they have been described. In the first one, [Viúdez *et al.*, 1998], the event is just described using a series of SST images from October 22<sup>nd</sup> to December 1<sup>st</sup> 1996. More recently, Vargas-Yáñez *et al.* [2002] used SST images to follow a similar evolution of the Alborán Sea circulation in autumn 1997, using a CTD transect along 3°W and current-meter measurements south of the Alborán Island to confirm that the old WAG went through the Tres Forcas Ridge during the three gyre episode.

Some of the previously described WAG disappearances can also be interpreted as snapshots of eastward WAG migration events. Specifically, Cheney and Doblar [1982] found that during a survey in October 1977, the WAG was displaced to the east and a smaller anticyclonic gyre was placed southeast of Ceuta, while the survey carried out ten days later showed a fully developed WAG at its usual position, thus indicating a migration of the old WAG. Following the work by Crepon [1965], these authors interpreted the anomalous situation as being due to the westerly winds in Gibraltar and the decrease of pressure in the western Mediterranean. In April 1980, and after a drop in the atmospheric pressure over the western Mediterranean, a similar situation was observed by Parrilla [1984].

WAG migrations events need to be understood since they are closely related to gyre formation and therefore to the overall Alborán Sea dynamics. Some mechanisms have been proposed to explain WAG disappearances, among others, hydrodynamic instability [Speich *et al.*, 1996] and mixing, which increase the size of the WAG [Viúdez *et al.*, 1998]. However, those mechanisms should show periodic WAG disappearances, a behavior, to our knowledge, not observed.

Regarding the time variability of the whole Alborán Sea, the results shown by *Vargas-Yáñez et al. [2002]* and the careful review of references done by those authors show agreement in that the Alborán Sea presents both annual and semi annual variability; where the atmospheric forcing seems to play an important role. The two-gyre system (WAG and EAG) is the dominant pattern in summer, and the coastal mode is more likely to exist in winter, spring and autumn being transition periods. *Viúdez et al. [1998]*, using altimeter data, also found an annual and semi-annual cycle in the Alborán Sea.

The objectives of this chapter are twofold. Firstly, the three-dimensional structure of the western Alborán sea during October 1996 will be described, including the sharp density front found and the high velocities associated with the AJ and the WAG. The intense geostrophic circulation found is an appropriate framework for significant secondary ageostrophic circulation, and hence for the establishment of high vertical motions, the main objective of this thesis. To understand the time variability of the vertical velocity fields it is necessary to have a precise knowledge of the time evolution of the hydrodynamic features. Moreover in the present case, where the time evolution in the western Alborán Sea during the first fortnight of October 1996 was governed by a change in the inflow through the strait of Gibraltar, rather than due to the slow QG evolution. The temporal evolution will be addressed throughout a description of the eastward migration of the WAG. To our knowledge, this is the first time that this phenomenon is covered in detail. The repetition of hydrographic surveys allowed us to describe the three-dimensional structure of the WAG and its time evolution during the initial phase of the WAG migration, confirming that the evolution observed in the SST images affected the whole water column. The description of the three gyre circulation after the migration event began is carried out with the help of float data and SST images. The results presented here will help to establish autumn as the transition between the two circulation patterns found in the western Alborán Sea and will support the idea that the atmospheric and tidal forcing are the mechanisms behind the WAG migrations events.

The remainder of this chapter is organized as follows: section B.2 provides a description of the circulation and water masses in the western Alborán Sea during the first fortnight of October 1996. The hypotheses regarding the two mechanisms, tidal and atmospheric forcing, that triggers the WAG migration are discussed in section B.3. Finally, the conclusions are presented and summarized in section B.4.

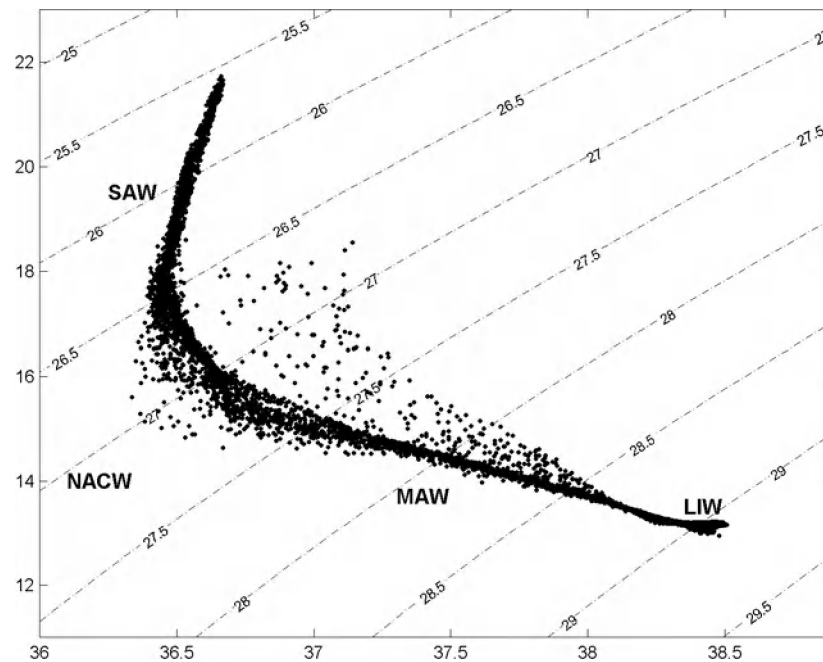


**Figure B.1.** Potential temperature and salinity diagram for the first survey in the 0-350 dbar range. The isolines of potential density are overlaid for reference.

## B.2 CIRCULATION AND WATERS MASSES IN THE WESTERN ALBORÁN SEA

### B.2.1 Initial conditions

Four differentiated water masses were found in the western Alborán sea during fall 1996, as can be observed in figure B.1, where all potential temperature and salinity measurements obtained from the first survey are shown. The lighter waters were the Surface Atlantic waters (SAW), characterized by a quasi-homogenous salinity layer ( $S \approx 36.6$ ) accompanied with a constant temperature gradient. The salinity minimum that separates the SAW from the underlying mixture of Atlantic-Mediterranean waters is

characteristic of North Atlantic Central Waters (NACW) [Gascard and Richez, 1985]. During the first survey, the subsurface salinity minimum was as low as 36.34, but in the followings surveys it freshened up to 36.05. This subsurface salinity minimum is progressively lost by mixing, first within the strait of Gibraltar and afterwards in the Alborán Sea. Cano [1978] made a classification of the different  $\theta S$  diagrams found in the Alborán Sea, depending on the amount of NACW. Those diagrams with larger amount of NACW were considered as representative of waters recently advected through the Strait of Gibraltar. The presence of NACW in areas far away from the strait is considered as an indication of an increase of the flow. Here, the subsurface minimum of salinity will be used as the fingerprint of NACW and as an indicator of the origin of the water masses, since it will indicate if the waters have recirculated or if they have been recently advected through the Strait of Gibraltar. The SAW and the NACW, together with the interface between them, have been called Atlantic waters (AW) and are present in the top 200 dbar of the western Alborán Sea. Below these Atlantic waters, the  $\theta S$  diagram shows a linear relationship between potential temperature and salinity that is consequence of its origin: a mixture of Atlantic and Mediterranean waters called modified Atlantic waters (MAW). Levantine intermediate waters (LIW) were also observed. LIW is characterized by a local maximum in temperature and salinity, the  $\theta S$  diagram shows both maxima, with values in salinity up to 38.51. The overall circulation in the Alborán Sea is suggested by the SST image for October 3<sup>rd</sup> 1996 (figure A.1): there is a bowl of warm surface waters ( $T > 21^\circ\text{C}$ ) that constitutes the western Alborán gyre, its anticyclonic circulation is confirmed by the ADCP and hydrographic data. The bowl of warm waters at the eastern side of the Alborán ridge constitutes the eastern Alborán gyre. The Atlantic jet is located at the northern side of the WAG, characterized by colder surface Atlantic waters ( $T < 19.5^\circ\text{C}$ ), its path continues eastward, following the rim of the EAG.



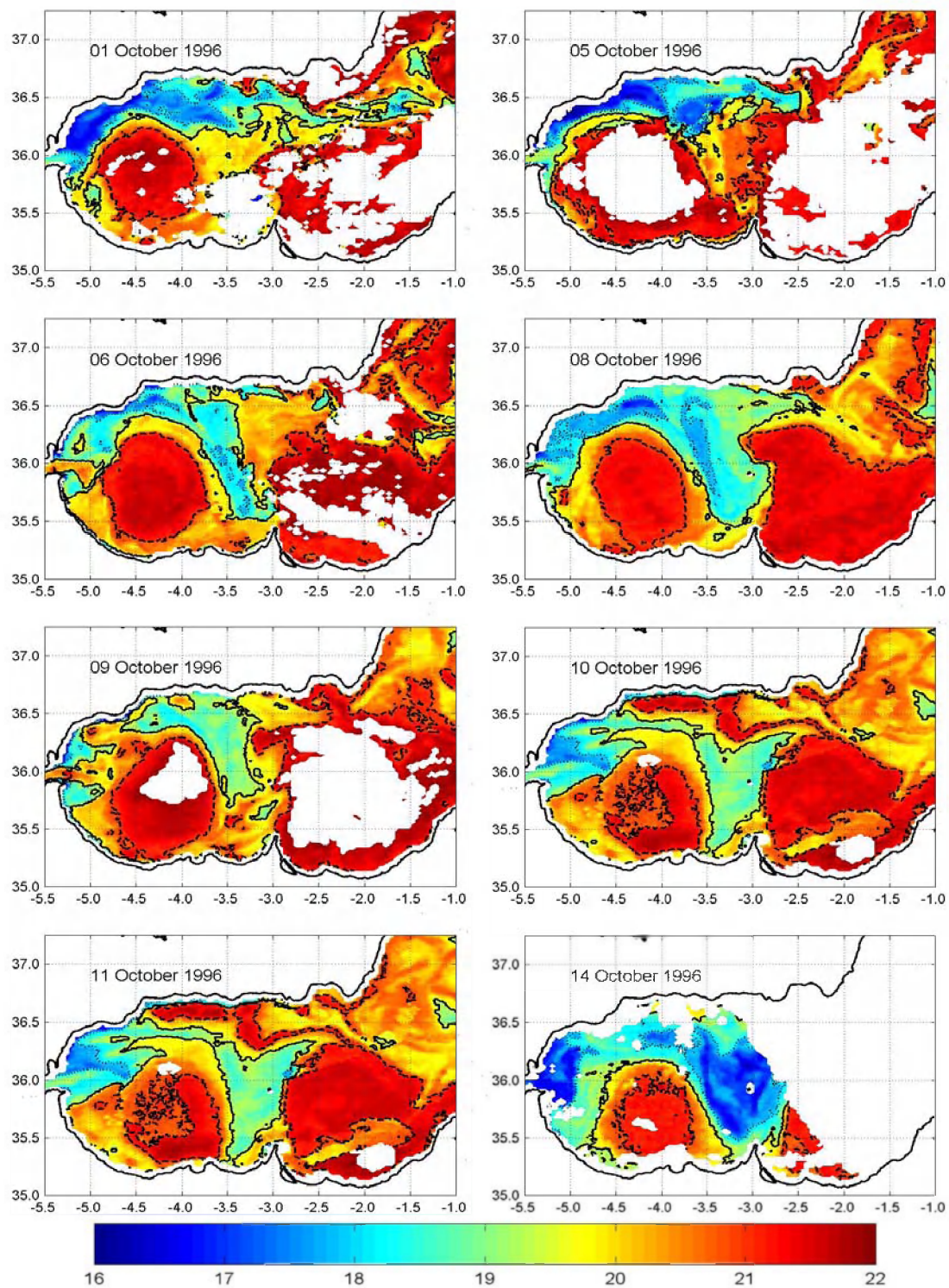


**Figure B.2.** Daily composites of SST from selected days, between October 1<sup>st</sup> and November 30<sup>th</sup> 1996. The dotted line corresponds to the 18°C isotherm, the thick line to the 19.5°C isotherm and the dashed line to the 21°C.



VERTICAL VELOCITIES AT AN OCEAN FRONT

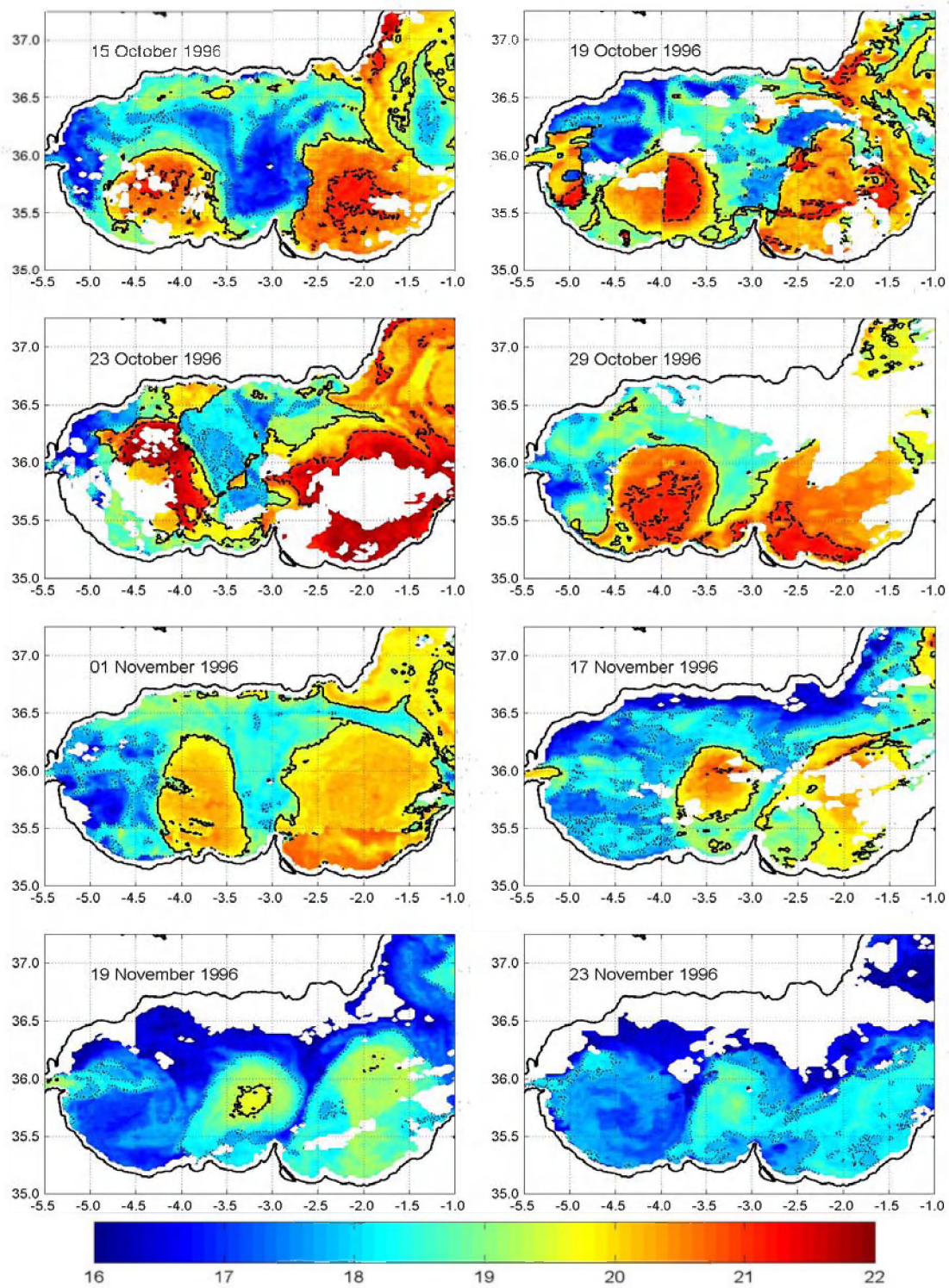


Figure B.2. (continued).

The SST for the starting day of the first survey (October 1<sup>st</sup> in figure B.2) shows the situation that can be considered as typical for the western Alborán Sea. Cold waters, ranging between 18 and 19.5°C, get into the Alborán Sea, surrounding and feeding the WAG. Warm waters of Atlantic origin ( $T > 21^\circ\text{C}$ ,  $S < 36.6$ , see figure B.3) are found in the inner part of the gyre, due to the longer residence time and isolation of recirculating waters.

S<	Ss1	Ss2	Ss3
36.30	0.00 (0.00)	1.33 (1.06)	1.32 (1.28)
36.35	0.00 (0.00)	1.36 (1.07)	1.32 (1.28)
36.40	0.87 (0.47)	1.36 (1.07)	1.32 (1.28)
36.50	1.01 (0.58)	1.40 (1.09)	1.32 (1.28)
36.60	1.24 (0.77)	1.40 (1.09)	1.32 (1.28)
Total	1.24 (0.77)	1.40 (1.09)	1.32 (1.28)

**Table B.I.** Maximum ADCP velocities (m/s), in the top 200 dbar at section 2, for those water parcels with salinities smaller than S. Between brackets is the maximum eastward component.

A three-dimensional description of the western Alborán Sea during the first survey is obtained from the horizontal and vertical transects (figures B.3, B.4, B.5 and B.6). The dominant feature is the bowl of low salinity ( $S < 36.60$ ) light MAW that forms the WAG (figures B.3b and B.3 e), as observed in the SST images. It extends down to 200 dbar, keeping the characteristic of the Atlantic inflow: a layer with a constant vertical gradient of temperature (figures B.3c and B.3f) and almost homogenous salinity ( $S < 36.6$ ), the WAG has also a strong signature in density. The geostrophic and ADCP velocities clearly show the anticyclonic circulation of the WAG; maximum ADCP velocities are 140 cm/s at the surface (12 dbar) and 90 cm/s at 90 dbar, while in the second leg (see table B.I) the maximum velocities reach 124 cm/s. The eastward ADCP transport at the second leg is 1.41 Sv (see table B.II), a value comparable with other estimates [Perkins *et al.*, 1990].



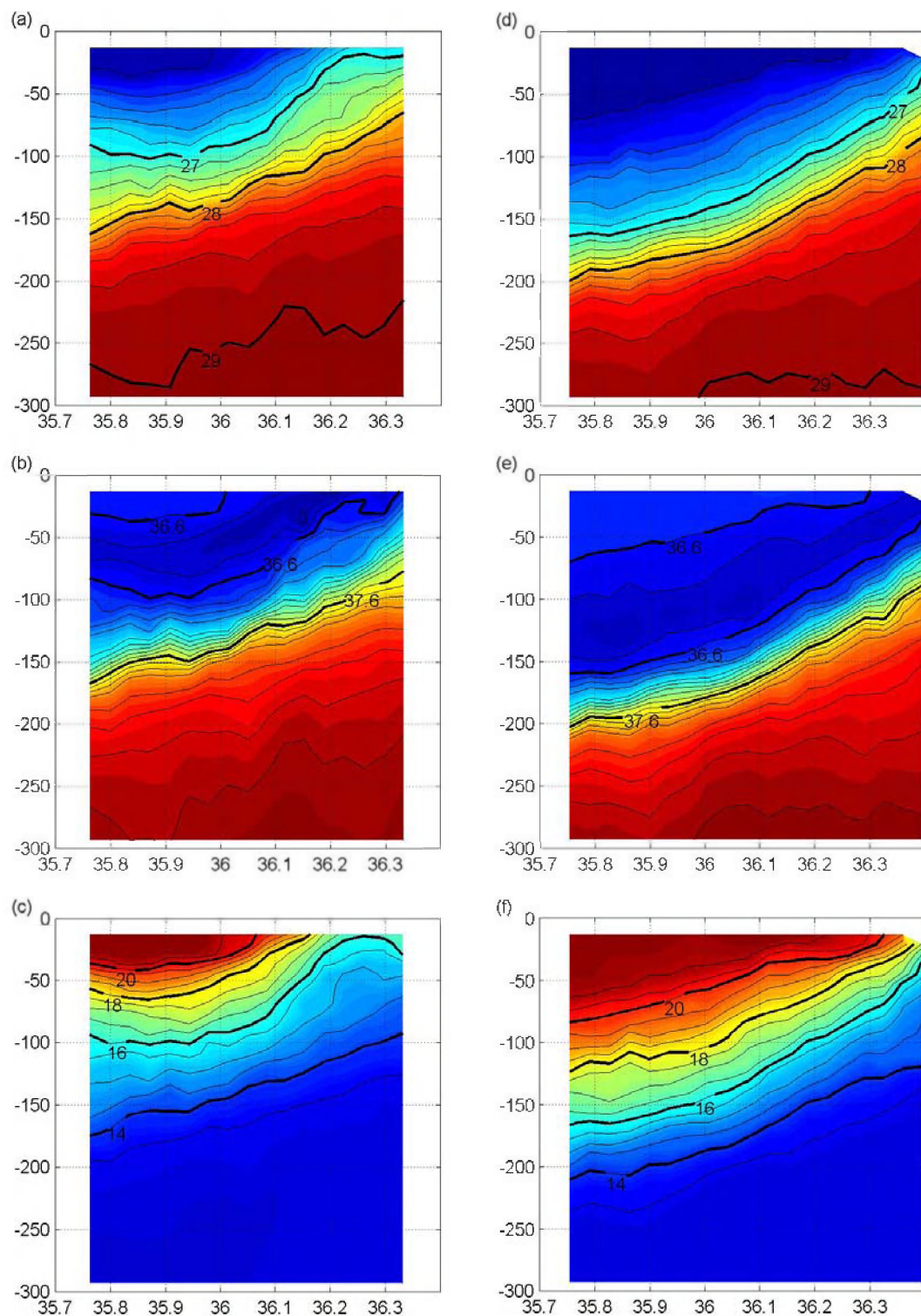


**Figure B.3.** Vertical meridional sections, for the first survey, of (a)  $\sigma_t$ , (b) salinity and (c) temperature along 4.8°W (section 2) and (d)  $\sigma_t$ , (e) salinity and (f) temperature along 4.36°W (section 6)

Separating the northern colder and saltier MW from the southern fresher and warmer MAW, there is a strong front, also observed in the vertical distributions (figure B.3). This density front is associated with the AJ and with the northern rim of the WAG, since the AJ and the WAG both coexist at 90 dbar; the AJ is distinguished from the WAG in the first two meridional legs in figure B.7a.ss1. At 4.9°W, the velocities south of 35.9°N are northward, corresponding to the WAG, while from 35.9°N to 36.2°N, the velocities are mainly northeastward, corresponding to the AJ. The doming of isotherms and isopycnals in the top 100 dbar of the westernmost legs of the first survey (figures B.3a and B.3.c) have been reported as an area of wind-driven upwelling [Cano, 1978; Sarhan et al., 2000]. This hypothesis is confirmed by the horizontal distributions and SST images. Geostrophic and ADCP velocity vectors rotate counter-clockwise northern than 36°N (figures B.6b.ss1 and B.7a.ss1), and an area of cold water ( $T < 17^{\circ}\text{C}$ ) appears in the northwestern part of the western Alborán Sea in the SST image for October 1<sup>st</sup> (figure B.2).

S<	Ss1	Ss2	Ss3
36.30	0.00	0.33	0.22
36.35	0.00	0.53	0.68
36.40	0.04	0.71	0.92
36.50	0.31	0.89	1.12
36.60	0.67	1.14	1.35
Total	1.41	1.69	2.51

**Table B.II.** Eastward ADCP Transport ( $\text{Sv}$ ), in the top 200 dbar, for those water parcels with salinities smaller than S

The subsurface salinity minimum that identifies NACW is present in both vertical sections of figure B.3, although with different values. In the section closer to the Strait (figure B.3b), the subsurface salinity minimum reaches values up to 36.37 near 36.15°N, while at 4.36°W (figure B.3e) the subsurface salinity minimum just reaches 36.41. The temperature of the water with this characteristic subsurface minimum is between 16°C-17°C (figure B.2).

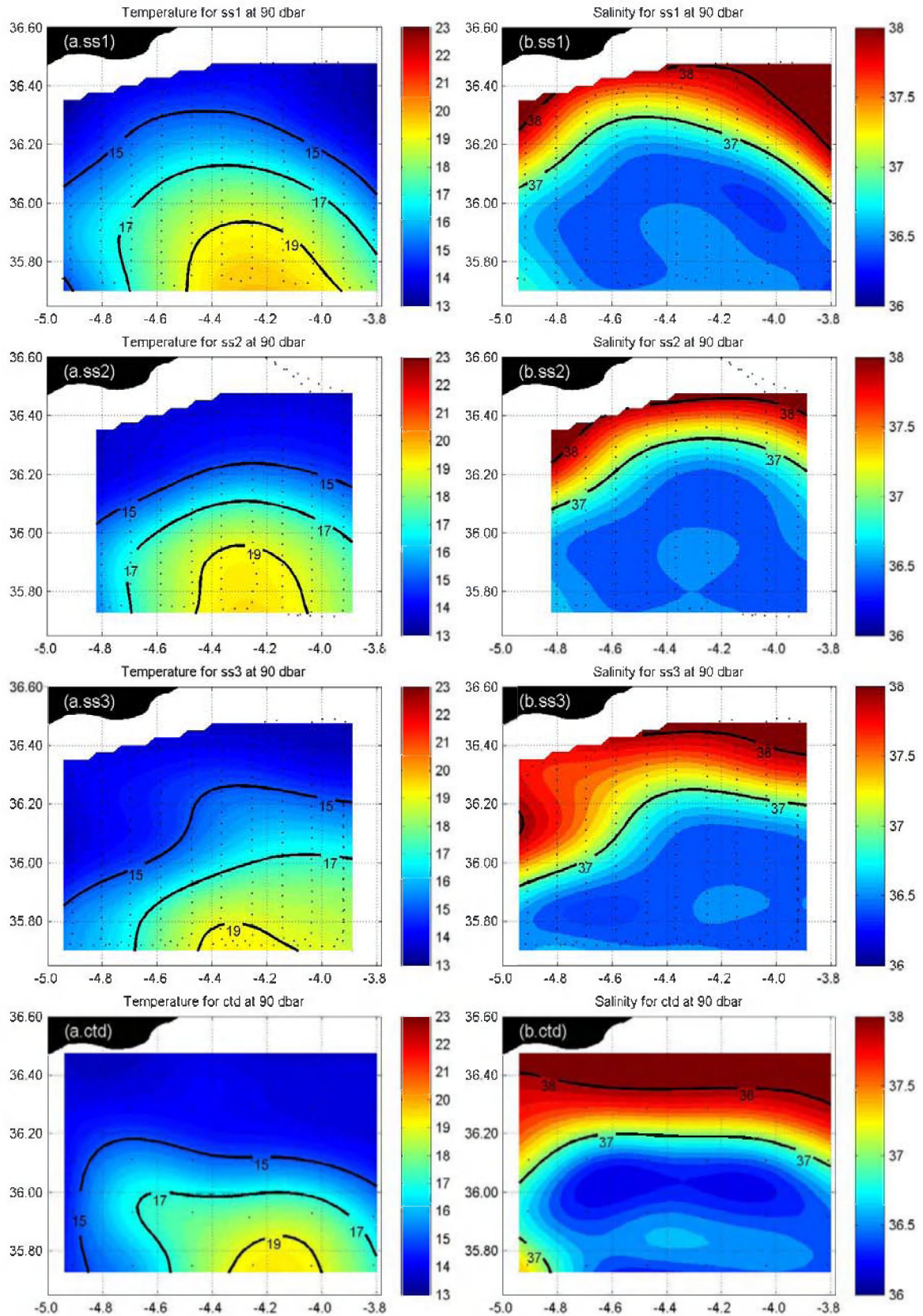


**Figure B.4.** Horizontal distributions of (a) temperature and (b) salinity for the (ss1) first, (ss2) second, (ss3) third and (ctd) fourth survey.



We have to remark that each survey was carried out right after the previous one, the use of SeaSoar allowed to complete each survey within 3-4 days, which is a short time, compared to the time scale for the large scale circulations changes of the Alborán Sea. This point has been verified by *Gomis et al.* [2001], who carried out a synopticity test for the dataset from the first survey.

### B.2.2 WAG migration

On October 6<sup>th</sup> (figure B.2), and coinciding with the beginning of the second survey, the Atlantic Jet appears well bounded by the 19.5°C isotherm, impinging directly against the WAG. While the WAG is pushed eastward, the area of cold waters to the northwest of the sampling area increased its size. The meandering of the front between the lighter MAW and the denser MW, represented by the thick line ( $T < 19.5^{\circ}\text{C}$ ) in the SST image for the October 6<sup>th</sup>, corresponds to that observed in the horizontal distributions of density and salinity (figures B.4a.ss2, B.4b.ss2 and B.5b.ss2), where both the isopycnals and the isohalines are displaced with respect to the first survey. For the second and third survey, as depicted by the horizontal distributions at 90 dbar (figure B.7), the ADCP and geostrophic velocities at 36°N have stronger eastward component, pushing the WAG and inducing the meandering of the front. The maximum eastward velocity at the second section increased from 77 cm/s (table B.I), in the first survey, to 109 cm/s in the second and 128 cm/s in the third survey. This change in magnitude was accompanied by an increase of the eastward ADCP transport (table B.II), from 1.41 Sv in the first survey to 1.69 Sv in the second and 2.51 Sv in the third survey. The meandering that began on October 6<sup>th</sup> continued during the third survey, as show by the horizontal distributions of density and geostrophic velocity (figures B.5b.ss3, B.6b.ss3). Moreover, comparison between the SST image and the 12 dbar horizontal temperature distribution (not shown) for the third survey confirms that the strong meander at 36.2°N, 4.6°W in the third survey corresponds to the warm anomalies observed in the SST image of October 9<sup>th</sup>, the start day of the third survey.

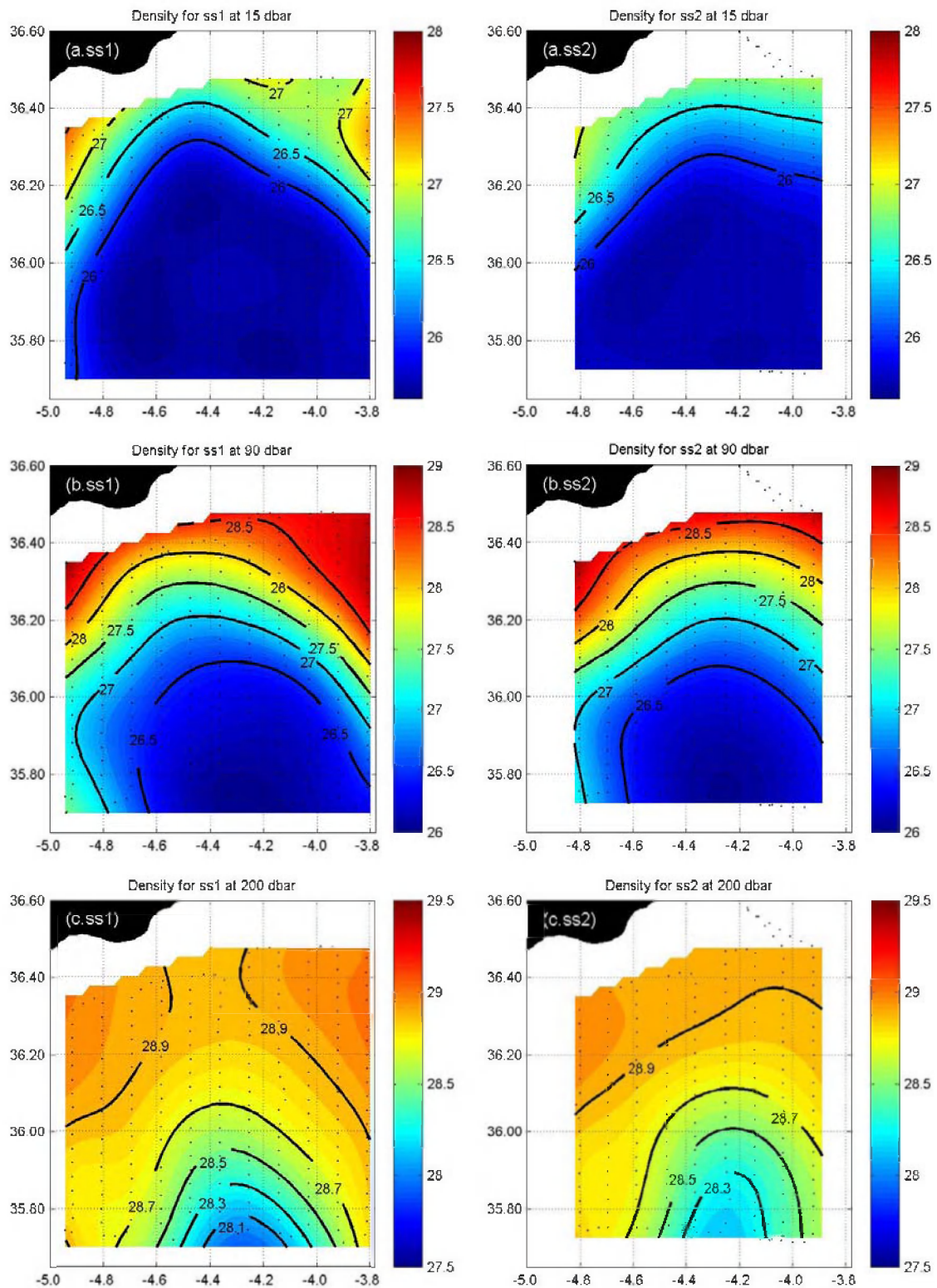


**Figure B.5:** Horizontal distributions of density ( $\text{kg/m}^3$ ) at (a) 15 dbar (b) 90 dbar and (c) 200 dbar for the (ss1) first, (ss2) second, (ss3) third survey and (ctd) fourth survey.



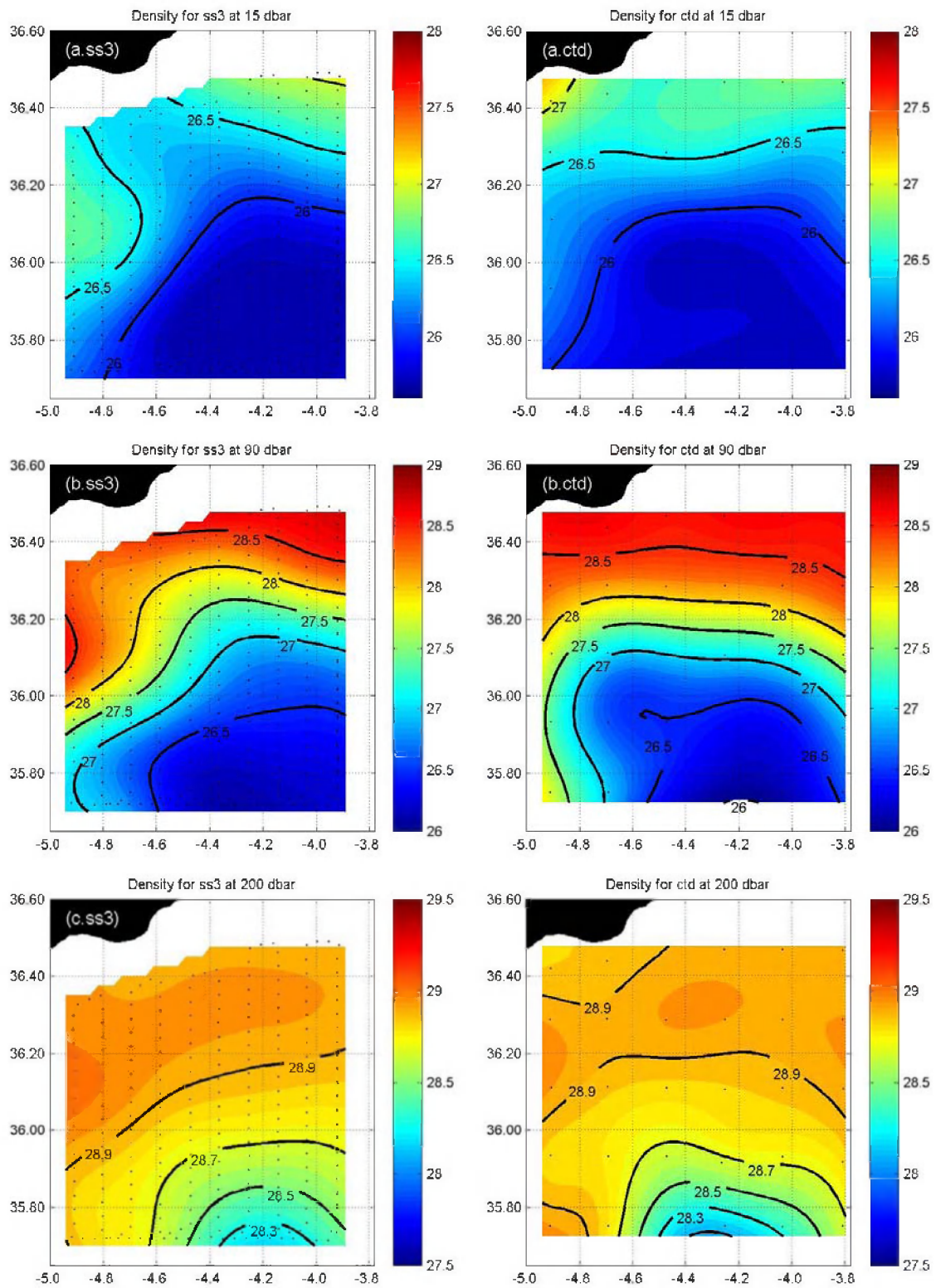
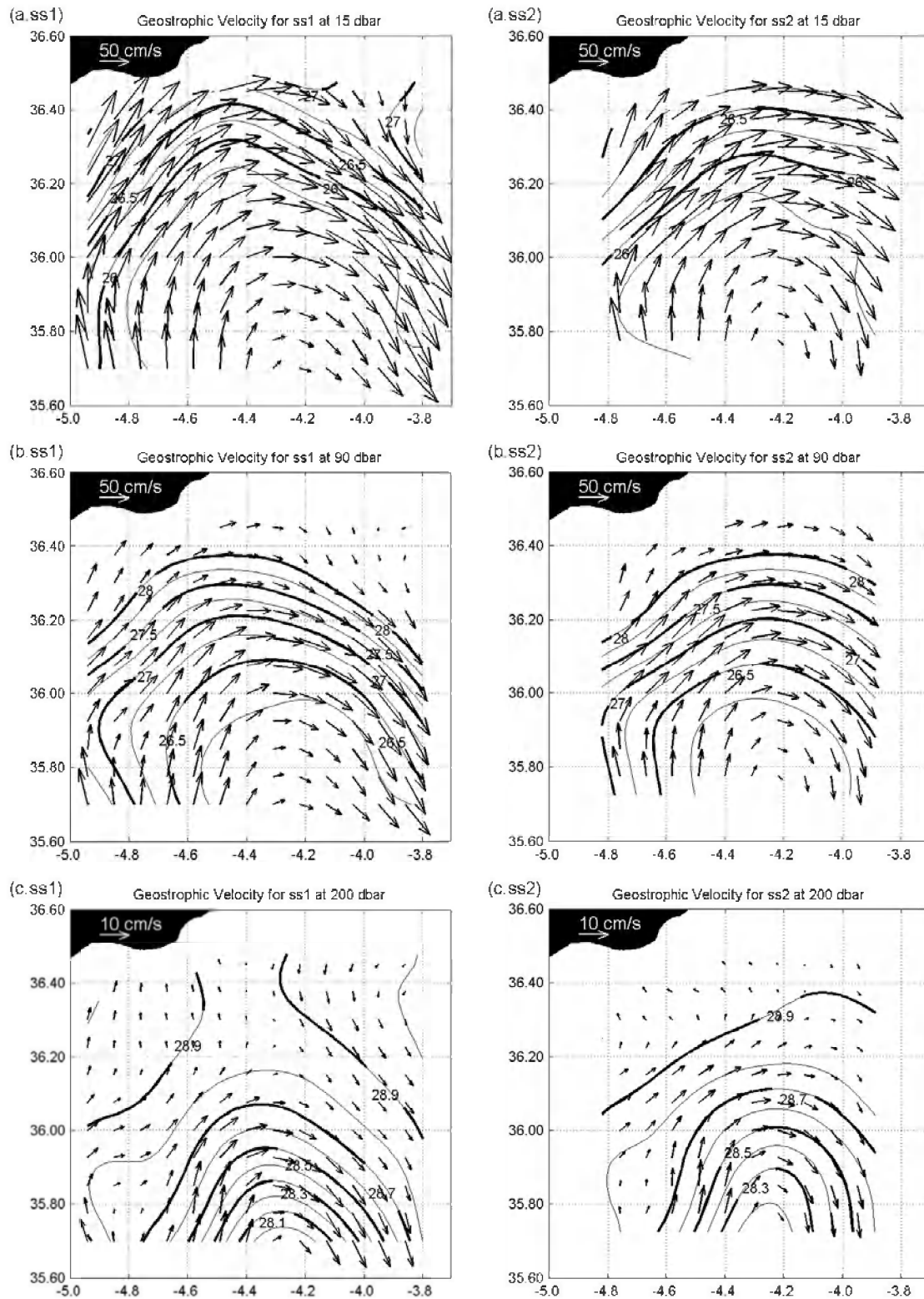


Figure B.5: (continued).



**Figure B.6.** Horizontal distributions of geostrophic velocity (cm/s) at (a) 15 dbar (b) 90 dbar and (c) 200 dbar for the (ss1) first, (ss2) second, (ss3) third survey and (ctd) fourth survey. The 26, 27 and 28 kg/m<sup>3</sup> isopycnals are overlaid for reference.



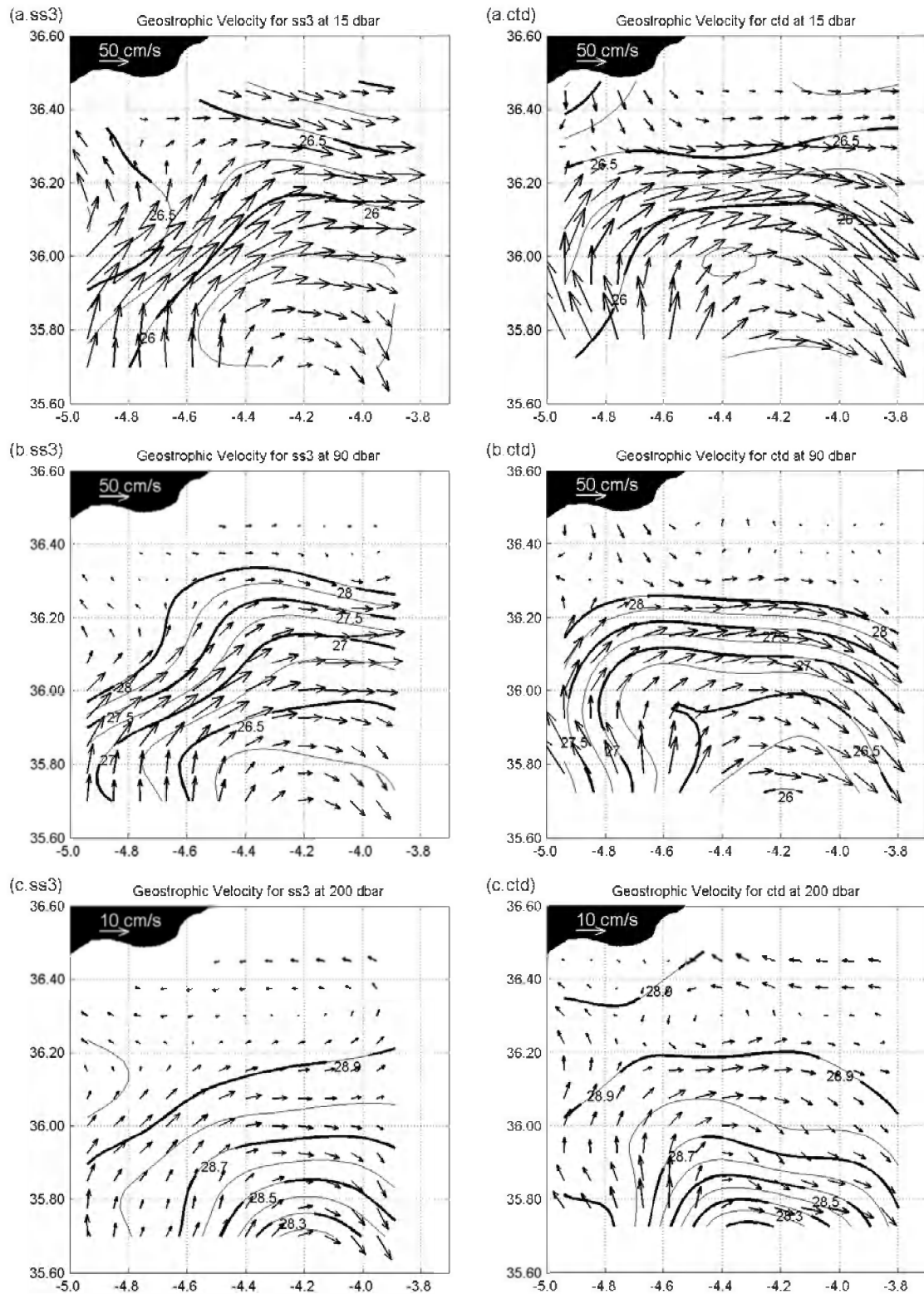
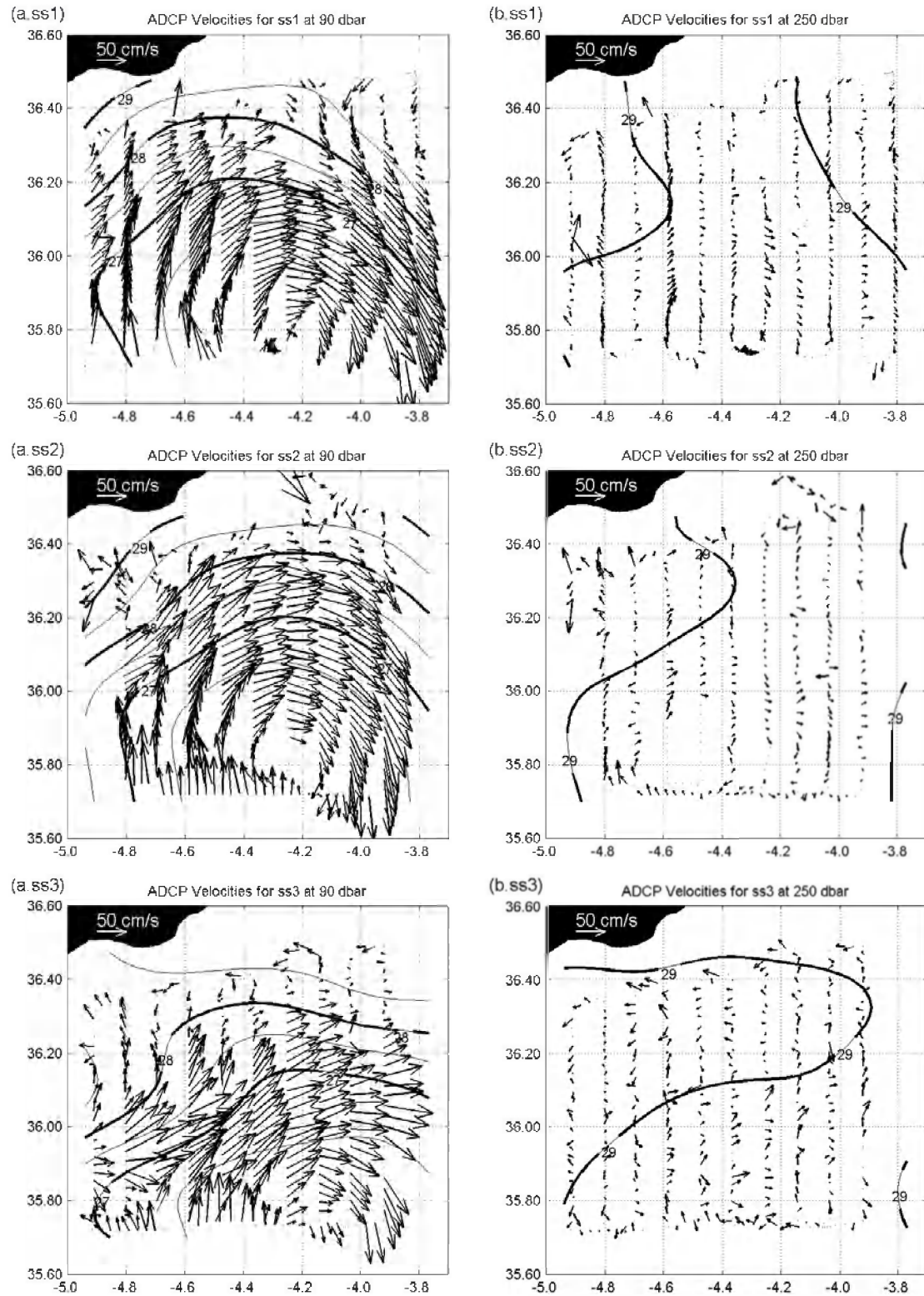


Figure B.6. (continued)

The SST image for October 11<sup>th</sup>, the start day for the last survey, shows a WAG that has been pushed eastward by the AJ. At the end of the fourth survey, the SST image for 14<sup>th</sup> October (figure B.2) shows a similar pattern. At this stage, the north side of the western Alborán Sea is occupied by a layer of waters colder than 19.5°C. This structure continues at depth, as shown in figures B.4b.ctd and B.6b.ctd, where the WAG has been displaced to the southeast. The cold water area initially found at the northwest and northern side of the WAG had increased its size. Previous authors [Sarhan *et al.*, 2000] have reported two favorable areas for upwelling or with quasi-permanent upwelling in the Alborán Sea: one to the northwest (already identified in figures B.2, B.3a, B.3b and B.3c) and the other to the south of the Malaga Bay (between 4.6°W and 4.0°W). These upwelling areas are associated with cyclonic circulation. In the case of the northwestern Alborán area, Sarhan *et al.* [2000] suggested that this upwelling was favored by southward excursions of the AJ. Figure B.2 does not allow us to establish neither the depth affected by the upwelling nor if it is linked to an area of cyclonic circulation nor if it is simply the southward advection of cold coastal waters upwelled by the wind. Comparison with figure B.6b.ss3 indicates that this is not a superficial phenomenon, since it is still visible at 90 dbar. Two cells of cyclonic vorticity (figures B.7a.ss2 and B.7a.ss3) are also identified, the first one associated with the eastern edge of the northwestern Alborán upwelling ( $\approx 36.3^\circ\text{N}$ ,  $4.9^\circ\text{W}$ ), and the second one with the Malaga upwelling ( $\approx 36.45^\circ\text{N}$ ,  $4.0^\circ\text{W}$ )

During the first fortnight of October, the SST images, the CTD and ADCP data revealed a WAG, that pushed by the AJ, drifting eastward, reducing its size and being now centered southern. The drift continued, as can be observed in the SST images for October 15<sup>th</sup> and 19<sup>th</sup>, on October 15<sup>th</sup>, the SST presents colder Atlantic waters drifting southward once they exit from the Strait of Gibraltar.



**Figure B.7.** ADCP velocities at (a) 90 dbar and (b) 200 dbar for the (ss1) first, (ss2) second and (ss3) third survey.

It is interesting to note that between October 14<sup>th</sup> and the 16<sup>th</sup> there was a decrease in atmospheric pressure at Ceuta, accompanied by a drop (decrease in the velocity into the Mediterranean Sea) in the sea level differences between Ceuta and Algeciras (figure B.10a). Although the analysis of the SST images from the October 22<sup>nd</sup> to December 1<sup>st</sup> was done in the work of *Viúdez et al.* [1998], we have included some of the SST images here for completeness, since these authors did not use any hydrographic data to confirm the time evolution described in the SST. Between October 15<sup>th</sup> and November 19<sup>th</sup> the drift continued, displacing the WAG from 4.40°W to 3.25°W, resulting in a mean eastward advection speed for the WAG of 4 cm/s. By November 1<sup>st</sup>, anticyclonic circulation was observed south of Ceuta; this circulation is confirmed with the float data; and by November 19<sup>th</sup>, a fully developed WAG was at its usual position. Three anticyclonic vortices occupying the Alborán Sea appear in the SST image of November 23<sup>rd</sup>, these vortices are: the EAG, the old WAG placed north of Cape Tres Forcas, and the new WAG east of the Gibraltar Strait.

S<	Ss1	Ss2	Ss3	Ss4
36.30	--	0.9	1.4	0.091
36.35	0.016	1.45	3.619	1.094
36.40	0.281	2.1	5.5	2.9
36.50	9.60	10.9	14.6	11.6
36.60	20.7	21.9	23.0	18.3

**Table B.III.** Percent of water parcels, in the top 200 dbar, with salinities smaller than S

### B.2.3 Presence of North Atlantic Central Waters

The distributions of waters with  $S < 36.35$  for the four surveys are shown in figure B.8, during the first one, there were not water parcels with  $S < 36.30$  (table B.III); just 0.016% water parcels with  $S < 36.35$  (figure B.8a) and 0.281% with  $S < 36.40$ . The eastward ADCP transport for those waters at the second leg with  $S < 36.40$  was 0.04 Sv (table B.II). The distribution of recently advected Atlantic waters,  $S < 35.35$ , during the second survey (figure B.8b and table B.III) shows a significant increase, compared with the first



survey, reaching 1.45%. Most of those waters were found in the northern part of the sampled area in the neighborhood of the strait and above the 90 dbar level. For waters with  $S < 36.35$  the eastward velocities are higher, a few cm/s lower than the maximum ones, with values up to 106 cm/s (table B.I). The recently advected NACW are mainly distributed within the AJ, at the northern boundary of the WAG, and its advection is eastward, following the AJ path, with little recirculation within the WAG.

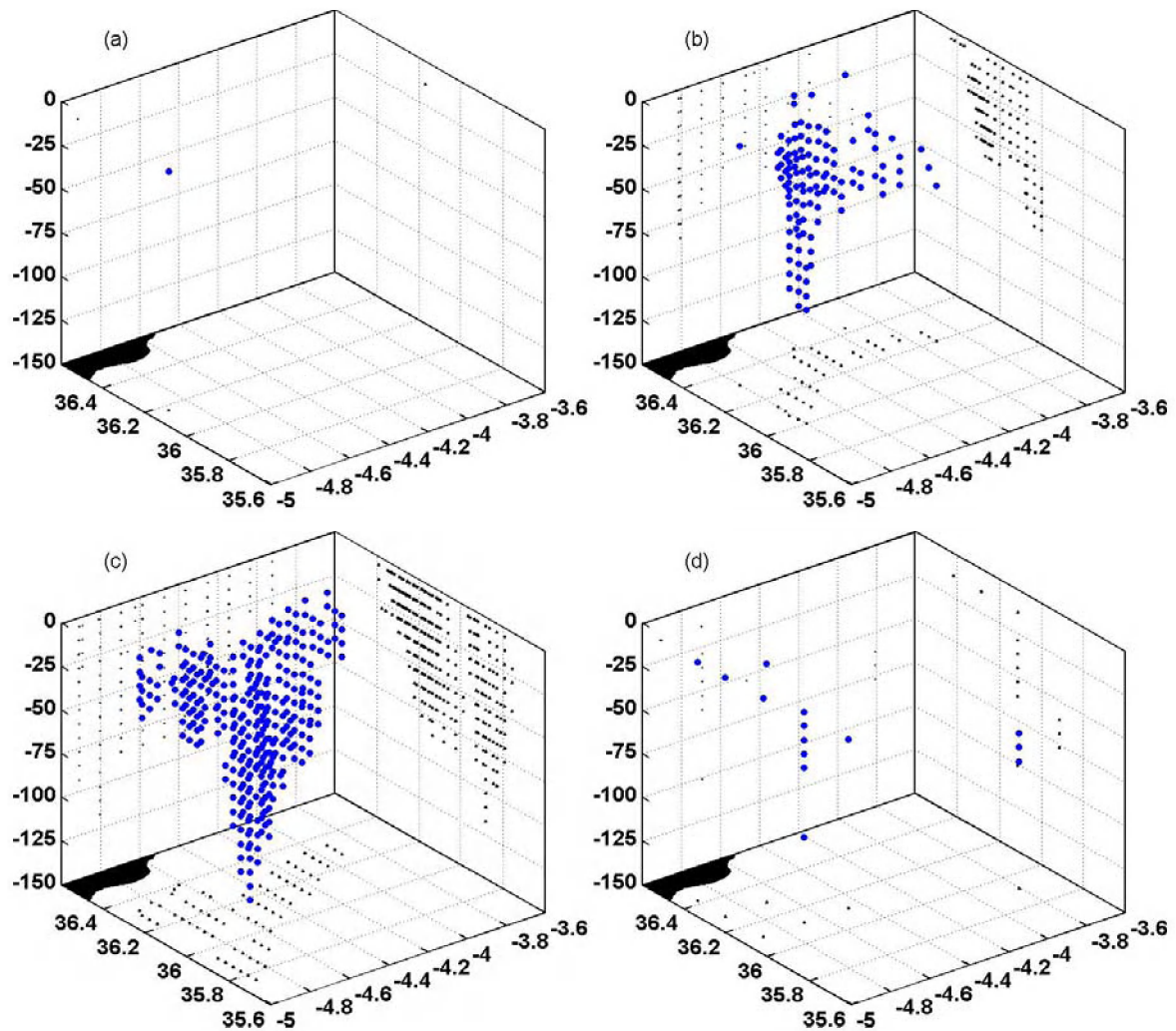


**Figure B.8.** Three-dimensional distribution of waters with  $S < 36.35$  for the (a) first, (b) second, (c) third and (d) fourth survey.

The observed changes in the amount of NACW coincides with the irruption of Atlantic waters, that pushed directly the WAG, observed in the SST image for the first day of the second survey (October 6<sup>th</sup> in figure B.2).

These observations, together with the studies carried out by *Cano* [1978], for whom large amount of NACW was representative of Atlantic waters recently advected, indicate an increase in the Atlantic flow. This interpretation is corroborated by the ADCP eastward transports of table B.II. The transport of the recent Atlantic waters ( $S < 36.40$ ) increased, from 0.04 Sv in the first survey, to 0.71 Sv in the second one, while the eastward transport of MAW ( $36.60 > S > 36.50$ ) was 0.25 Sv, similar to the 0.36 Sv found during the first survey.

Three days later, during the third survey (figure B.8c), the amount of water parcels with  $S < 36.35$  was 3.62%, indicating that the amount of recently advected Atlantic waters continued increasing. The recently entered NACW were also distributed along the AJ, meaning eastward advection with little recirculation. Advection is corroborated with the velocity data; the eastward ADCP velocities increased up to 128 cm/s, with its maximum value being in the purest NACW ( $S < 36.35$ ). The ADCP eastward transport also increased during the third survey (table B.II); for waters with  $S < 36.40$  it reached 0.92 Sv, while for the MAW ( $36.60 > S > 36.50$ ) the transport was 0.23 Sv, similar to the values found during the first and second survey. During the fourth survey (figure B.8d) the amount of recent NACW decreased in comparison with the second and third surveys; the quantity of waters with  $S < 36.35$  was 1.09% (table B.III). Unfortunately, there was not ADCP data for the fourth survey to be compared with previous surveys.

To summarize, the amount of fresher NACW increased between the first and the third surveys and decrease again between the third and the fourth surveys. On the other hand, the amount of waters with  $S < 36.6$  did not change appreciably during the four surveys. Accordingly, it can be concluded that the fresher waters found during the second and third surveys are consequence of a pulse of NACW, rather than due to recirculation of Atlantic waters within the WAG, in agreement with the transports measured by the ADCP. The pulse occurred between the end of the first survey and the end of the third one, lasting for approximately 5 days.



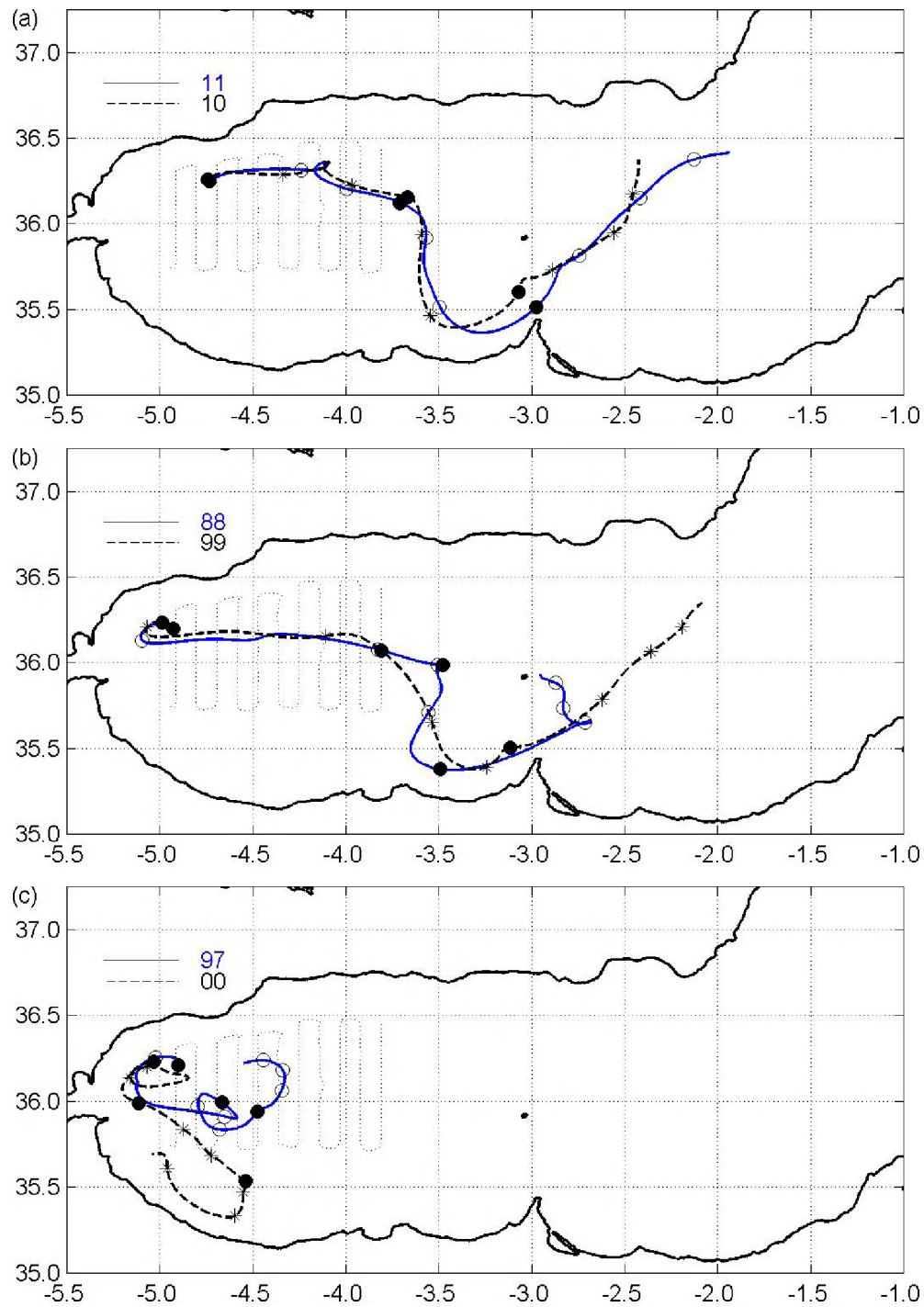


**Figure B.9.** Trajectories of the three pairs of floats. For reference, the first survey track is overlaid. The circles and asterisks denote the following dates: 8<sup>th</sup>, 11<sup>th</sup>, 20<sup>th</sup>, 26<sup>th</sup>, 29<sup>th</sup> October and 4<sup>th</sup>, 7<sup>th</sup>, 10<sup>th</sup> November, while the dark dots are for the 8<sup>th</sup>, 23<sup>rd</sup> October and the 1<sup>st</sup> November. The last data were received on November 14<sup>th</sup> 1996

### B.2.4 Float data

The time evolution of the western Alborán Sea after October 14<sup>th</sup> was followed with the help of the SST images and the float tracks data that extended up to November 10<sup>th</sup> that permitted to follow the migration event with subsurface data. Since the situation in the western Alborán Sea was not stationary, the trajectories of the floats are not streamlines and the float data have to be analyzed with care to avoid misunderstanding due to aliasing. After deployment, the deployed floats grouped in three pairs, each pair entering the sampled area after some time in a small cyclonic gyre near the Strait of Gibraltar and therefore providing a view of the western Alborán Sea circulation at three different times.

The first pair, (floats 10 and 11, figure B.9a) traveled quickly eastward within the Atlantic jet right after the deployment. The first days of the trajectories coincided with the first survey and the conditions represented in the SST image of October 1st (figure B.2). At 4.2°W, the pair was trapped in a small cyclonic eddy for four days; once the floats escaped from that eddy they traveled within the Atlantic jet. By October 26<sup>th</sup>, the pair began to turn southward, surrounding the WAG before entering the Alborán Passage. The first pair was on October 29<sup>th</sup> eastern that which would be expected if the WAG were at the position observed during the first days of October. This eastern position coincides with the drifted WAG that appears in the SST distribution for October 29<sup>th</sup>. The pair passed through the Alborán passage (35.7°N and 3.0°W in figure B.9a) on November 1st, and then rounded the EAG, towards the Almería-Orán frontal area [Tintoré *et al.*, 1988].

The second pair (floats 88 and 99, figure B.9b) was launched slightly north of the first one (figure A.1) and was trapped in the cyclonic eddy northwest of the WAG. After one loop in that cyclonic eddy, the pair continued eastward within the AJ, entering the sampled area on October 6<sup>th</sup>, the first day of the second survey. As observed in the SST images and the hydrographic data (figures B.6a.ss2 and B.7a.ss2) the gyre was displaced southward and thus the float trajectories were south of those from the first

pair. One of the floats from this second pair was also trapped in a cyclonic eddy at 36.0°N, 3.5°W (see figure B.9b). This eddy may be the same as the one that trapped the first pair, meaning an advection speed of 9 cm/s for that eddy. The second pair crossed the sampled area faster than the first pair, in agreement with the observed higher eastward velocities observed in the ADCP data. After October 26<sup>th</sup>, the pair followed a trajectory similar to the one described by the first pair, through the Alborán Passage and circling the EAG. The second pair confirmed the eastward drift of the WAG, since the trajectories on October 29<sup>th</sup> coincided with those that should be observed with the situation described by the SST image on that day.

The third pair (floats 97 and 00, figure B.9c) was launched north of the second one, and was trapped in the cyclonic eddy near the Strait, completing two loops. After the second loop, by October 18<sup>th</sup>, the pair went out of the cyclonic eddy. Between the October 23<sup>rd</sup> and the November 1<sup>st</sup>, float 00 traveled southeastward, corroborating the southward drift, 'coastal mode', of the Atlantic waters observed after October 15<sup>th</sup> in the SST images (figure B.2). After the November 1<sup>st</sup>, float 00 turned anticyclonically, following the cold Atlantic waters. These waters in the absence of the WAG advanced attached to the African coast, once they exit from the strait, to develop a new WAG, as suggested by *Viúdez et al* [1998] and *Vargas-Yáñez et al* [2002]. After October 23<sup>rd</sup>, float 97 went into the western Alborán Sea, describing a cyclonic journey (36.1°N, 4.6°W, figure B.9c). The subsurface circulation depicted by floats 97 and 00 is in agreement with the circulation inferred from the surface temperatures; the SST image for November 1<sup>st</sup> (figure B.2) shows the old WAG near Alborán Island and a bowl of cold waters at the usual position of the WAG; fifteen days later, the SST image shows the Atlantic waters turning anticyclonically once they exit from the strait of Gibraltar. The flow pattern, mushroom-like, described by floats 97 and 00 is due to the lack of a well-developed WAG, in such a situation, the AJ is not deflected to the northeast and the floats do not cross over the western Alborán basin as the previous pair did. This mushroom-like flow is usually found in fluids where there is an input of momentum and

therefore corresponds to a situation where the AJ, and its associated momentum, goes into the western Alborán Sea without being deflected northward by the WAG.

Several papers have addressed the question under which conditions the AJ will follow an anticyclonic trajectory and when it will follow the African coast as a coastal jet. Most of these works relate this issue to the upstream conditions in the Strait of Gibraltar. *Bormans and Garret* [1989], in their review of laboratory and numerical models, conclude that the critical parameter determining the detachment of the AJ from the African coast and the fast development of an anticyclonic gyre is the ratio between the inertial radius and the curvature radius in the Strait. *Gleizon et al.* [1996] agree on the importance of the upstream conditions. The gyre formation is linked to the volume flow, which could be related to the AJ momentum, and hence to the inertial radius. According to these authors, the circulation pattern (gyre or coastal jet) is determined by the ratio between internal radius and the width of the Strait.

### B.2.5 Sea level and pressure changes

The inflow through the strait is in quasi cross-strait geostrophic balance [*Kinder and Bryden*, 1987; *Lafuente et al.*, 1998], and measurements of cross-strait sea level slope can be used to estimate an averaged inflow speed  $U$ , using the following expression:  $-g\Delta D/fL$ . Where  $\Delta D$  is the sea level difference between the south (Ceuta) and the north (Algeciras) shores of the Gibraltar Strait;  $f$  is the Coriolis parameter at the latitude of the strait; and  $L$  is the distance between Ceuta and Algeciras. Errors in tide gauges leveling do not permit to obtain absolute velocities, for that reason only the relative sea level differences between the two shores of the Gibraltar Strait is shown (figure B.10a); higher sea level difference meaning higher inflow speed into the Mediterranean Sea. However, the information given by the sea level differences will yield to two important conclusions, each one described and demonstrated in the following paragraphs.

After the fourth survey, a relative minimum is observed on  $\Delta D$ , which corresponds to a minimum in the Atlantic inflow. At the same time, a drop in the atmospheric pressure at Ceuta ( $P_c$ ), of 15 mb in three days, is observed with the minimum on October 15<sup>th</sup>. As observed in the corresponding SST images (figure B.2) and the float data, is around this time when the WAG began its eastward migration.

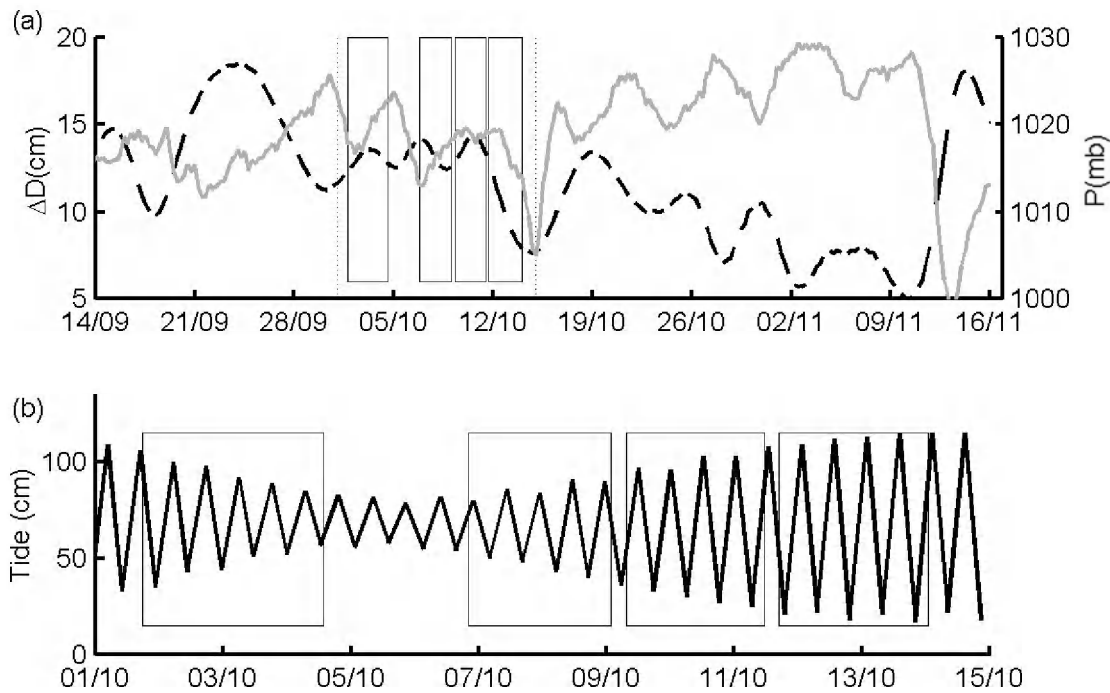


**Figure B.10.** (a) Time series of sea level atmospheric pressure at Ceuta (solid lines) and the difference between the sea level at Ceuta and the sea level at Algeciras (dashed line). (b) Tides at Algeciras. The boxes indicate the timing of each survey. Note the different time interval covered in (b). The two thin dashed lines in (a) denote the time interval covered in (b).

The decrease in the transport through the Strait indicated by  $\Delta D$  means a lower inertial radius for the inflow [Bormans and Garrett, 1989], producing, with an eastward displaced WAG, a southward deflection of the AJ into the coastal mode, in agreement with the SST images and the float observations. Due to the uncertainty in determining the exact day for the beginning of the coastal mode and the development of the new WAG we are aware of the speculative character of this interpretation. However, Vargas-Yáñez *et al.* [2002] have also pointed out the possibility that a drop in the inflow velocity leads to the coastal mode or a three gyre situation if the WAG is rapidly

recovered, as described here. The low sea level difference found on November 10<sup>th</sup> indicates that the decrease in the Atlantic flow continued, favoring the formation of the new gyre. Indeed, four days later the new gyre was clearly visible on the SST images. This is consistent with laboratory simulations where sub-critical inflows lead to the formation of large WAGs [Gleizon, 1994].

It is interesting to note that in the period represented in figure B.10a there is significant correlation between  $\Delta D$  and the pressure at Ceuta ( $P_c$ ), with the usual phase opposition and lag found in other studies [Crepon, 1965; Candela *et al.*, 1989; Vargas-Yáñez *et al.*, 2002], exception is the pressure drop centered on October 15<sup>th</sup>, where the correlation is opposite to the expected one. The correlation between  $P_c$  and  $\Delta D$  is -0.6, but reaches -0.7 if the data between October 12<sup>th</sup> and 17<sup>th</sup> is not included. This different behavior of  $\Delta D$  during the pressure drop October 15<sup>th</sup> may be due to the strong easterlies between October 13<sup>th</sup> and October 15<sup>th</sup> that could have produced a decrease in sea level, and hence in the inflow speed into the Mediterranean Sea, in spite that the pressure drop would have caused the opposite effect. Conversely, the lack of a meaningful increase in the sea level differences during the first 12 days of October does not invalidate the hypothesis of an increase of the Atlantic inflow between the beginning of the first survey and the end of the third one, since the ADCP velocities have confirmed the change in the velocity and transport of the incoming Atlantic waters. The hydrographic data have shown that this increase in the Atlantic inflow is related with the arrival of new NACW and therefore the measurements of cross-strait sea level slope are not a good proxy for the averaged inflowing speed  $U$  given that there are significant changes in the thickness of the inflow layer.

The analysis of the data has related the WAG migration to changes in the Atlantic inflow, but the causes for this change in the Atlantic inflow are not clear. The works of Gascard and Richez [1985] and La Violette and Lacombe [1988] suggested that the injection of Atlantic Water, either SAW or NACW, into the Alborán Sea is highly influenced by tides. These authors observed that only during neap tides pure NACW

enters the Alborán Sea. Between the end of the first survey and the beginning of the second, a neap tide occurred, as reflected by the sea level at Algeciras (see figure B.10b), the minimum amplitude was registered on October 5<sup>th</sup> at 20:32:00 GMT, just before the recently advected NACW was observed in the second and third survey. The atmospheric pressure at Ceuta during those days did not show any significant change, consequently, it seems reasonable to assume that the neap tide contributed, or even produced the Atlantic pulse.

### B.3 DISCUSSION

Given these results, it seems that two necessary conditions have to be fulfilled for WAG migrations to occur. Firstly, the velocity and the transport through the Strait of Gibraltar should increase. The hydrographic data confirms the advection of new NACW, the increase in velocity and transport were observed with the help of the ADCP. The Coriolis force obligates the Atlantic waters moving at higher speed to separate from the Spanish coast before the waters reach the easternmost side of the strait [*Bormans and Garrett*, 1989] and the flow enters the Alborán Sea in an almost eastward direction [*Lafuente et al.*, 1998]. Under such circumstances, the Atlantic waters does not flow around the WAG, but the AJ impacts directly into the WAG, thereby shifting it eastward, as observed in the hydrographic data of the last survey and the float data. The position and size of the WAG also contributed, since the WAG was at its northern possible position, the 200 m isobath. Afterwards, a decrease in the Atlantic flow helped with the migration of the WAG and the formation of a new gyre. The decrease of the flow through the Strait and the absence of the high pressure associated with the WAG produce a southward drift of Atlantic waters, as confirmed by the float data. The further decrease of the Atlantic inflow lead to the formation of a new WAG, in agreement with the laboratory results of *Gleizon* [1994].

We suggest that two necessary conditions should be fulfilled for an eastward migration event. Otherwise, the stable character of the WAG will not permit the migration. The



first condition is related with the tidal forcing. The hypothesis of a tidal induced pulse between the second and the third survey is supported by our data. The second condition is a decrease in the Atlantic inflow, induced by meteorological conditions. Different mechanisms have been proposed to explain WAG disappearances, among others, hydrodynamic instability [Speich *et al.*, 1996] and mixing, which increase the size of the WAG [Viúdez *et al.*, 1998]. However, those mechanisms would show periodic WAG disappearances, a behavior, which to our knowledge is not observed. The random character of the coincidence in the two conditions described above explains the lack of periodicity observed in the WAG migrations, although with preference to occur in periods with frequent drops in atmospheric pressure, in agreement with Vargas-Yáñez *et al* [2002].

## B.4 CONCLUSIONS

The intense mesoscale activity found in the western Alborán Sea is the ideal framework for the establishment of estimates of vertical velocities, as will be shown in the following chapter. The study of a comprehensive dataset, in time and in space, has allowed describing, for the first time, the time evolution of the Western Alborán Sea during a WAG migration event. In the first survey, the hydrographic structure is the one most typically found in the western Alborán Sea: the WAG, an anticyclonic vortex formed by MAW waters, occupying the southern part of the western Alborán basin and surrounded in its northern rim by the Atlantic jet. This typical situation was modified by an eastward migration. Two requirements, associated with two different mechanisms are crucial to trigger the eastward migration of the WAG. The first one is the increase in the Atlantic inflow that pushed the WAG eastward. The surface circulation, inferred from SST, describes the WAG migration, the CTD data confirm that the migration occurred in the whole water column and that the waters advected during the pulse were mainly NACW. The mass transport obtained with the ADCP data established that the increment in the flow of pure NACW was associated with an increase in the



transport and magnitude of the Atlantic inflow through the strait. The fact that a neap tide occurred at the same time as the pulse of NACW reflects the importance of tidal forcing in driving the increase in the flow of NACW. The second necessary requirement is the intense decrease in the Atlantic inflow after the pulse, which permitted the migration of the WAG, the southward drift of the Atlantic jet and the developing of a new WAG. The further evolution of the western Alborán Sea circulation was well described by the floats and the SST images; this evolution is in agreement with other studies [*Bormans and Garrett*, 1989; *Gleizon*, 1994].

As far as we know, it is the first time that the large-scale variability of the Alborán Sea has been clearly related to changes in the Atlantic inflow through the Strait of Gibraltar. Moreover, a clear relationship between this change and a WAG migration has been described [*Vélez-Belchí et al.*, 2005].

EN CADA AMANECER  
HAY UN VIVO POEMA DE ESPERANZA,  
Y, AL ACOSTARNOS,  
PENSEMOS QUE AMANECERÁ

*Noel Clarasó*

---

## **C.-ANALYSIS METHODS**

---

## C.0 ABSTRACT

The observed hydrographic fields are a non-regular discrete sampling of the ocean, and hence to describe the dynamical variables it is necessary to interpolate the data onto the nodes of a regular grid. Besides that, observations sample the continuous of spatial scales found in the ocean, and therefore, the measurements are contaminated by the aliasing of unresolved scales. To both, maximizes the signal-to-noise ratio and interpolates the observed data onto a regular grid, an optimal “mapping” scheme based on *Bretherton et al.* [1976] has been used; methods based on this formulation are usually called objective analysis (OA) in the oceanographic community. In the present chapter, the characteristics of the objective analyses technique used are described; and a sensitivity study of the derived variables, mainly vertical velocity, to changes in the parameters of the OA is included in order to quantify the impact of the observational and sampling error. In spite of the fact that the results indicate that estimations of vertical velocity are contaminated by the discrete sampling and the noise of observations, the sign, order of magnitude, and spatial scales of the diagnosed vertical velocity field are still valid, as will be corroborated in the next chapters.

## C.1 INTRODUCTION

To understand the three-dimensional circulation of an oceanic front is necessary to compute dynamical variables as geostrophic velocity, geostrophic relative vorticity, and vertical velocity. This implies high-order spatial derivatives of the observed density and geopotential fields. Although the observations described in section A.1 are at a nearly regular grid, it is necessary to map them onto a regular grid to compute the derived variables. However, it is not appropriate to consider this step just as a simple interpolation, since any interpolation from a discrete set of observations will also be subject to the uncertainty linked to the observational and sampling errors. The *observational error* is associated with the aliasing errors due to unresolved scales and with the, usually small, measurements errors on observations. On the other hand, the *sampling error* is related with the poor sampling of those spatial scales resolved by the observations. This error depends only on the distributions of the measurements, and it is the error left in the case of perfect observations. Both errors came out as consequence of the continuous spectrum of spatial scales that comprehend the ocean spatial variability, together with the fact that any sampling of the ocean represents a bandwidth of spatial frequencies, but not all the frequencies sampled will be resolved by the discrete set of measurements.

In consequence, it is convenient to use an interpolation technique, that based on statistics of the sampled data, maximize the signal-to-noise content of the analyzed data and therefore avoid the amplification of small-scale noise in the differentiation process. An example of such statistical technique is the set of schemes based on *Gandin* [1963] and *Bretherton et al.* [1976], usually called objective analysis (OA) in the oceanographic community. The scheme used here belongs to this set of schemes and follows the principles of Optimal Statistical Interpolation (hereafter OI).

Although OI maximize the signal-to-noise content of the analysis, to correctly quantify biogeochemical fluxes at mesoscale, as pointed out by *Martin and Richards* [2001], it is

necessary to quantify the impact of the observational and sampling error and therefore the accuracy of the mapped fields and the associated uncertainty in the derived dynamical variables as the vertical velocity.

With the exception of the work by *Gomis and Pedder* [2005], it has not been attempt to quantify this accuracy in oceanographic studies. Those authors carried out a theoretical and numerical study of the accuracy of the dynamical fields inferred from the first survey of the dataset used throughout this thesis. They found that for the observed variable, the dynamic height, the typical fractional error (this is, ratio of the total rms error to the standard deviation of the anomaly field) within a region away from the boundaries was 2.5%, reaching 6% near data voids. The fractional error decreased to 0.5% and 2% if the OI analysis was convoluted with a filter to cut-off those wavelengths not properly resolved. Large errors ( $> 2.5\%$ ) were found near the boundaries of the sampled area and around data voids, since the interpolation accuracy is reduced due to the asymmetry of the observations distribution, usually called the boundary effect. The width of this region of high error increases if the OI analysis is convoluted with a filter. For geostrophic velocity and vorticity, variables linearly related with dynamic height, the error distribution was similar to those obtained for dynamic height. In the inner domain, the fractional error for geostrophic velocity range from between 6% and 10%, while for geostrophic vorticity it ranged between 9% and 12%. This error was reduced to 2.5% and 4% with the convolution of OI with a filter, although after the filter, the errors near the domain boundaries reached 20% and penetrated further into the domain. For vertical velocity, the fractional error was 6%-10% in a small inner domain, exceeding 20% half a way between the centre of the domain and the lateral boundaries. After the filtering, the inner domain was reduced, penetrating the large error area near the lateral boundaries. Nevertheless, the study carried out by *Gomis and Pedder* [2005] should be considered as realistic lower bound for observational and sampling error, given that they assumed a precise knowledge of the statistical

parameters necessary to use OI, like the for the correlation model and the large scale mean field.

Given the importance of the objective analysis in obtaining accuracy-derived variables, as vertical velocity, and the lack of studies where the uncertainty in the diagnosed vertical velocity is addressed, in this chapter the objective analysis scheme used will be briefly described, including a justification of the statistical parameters considered as the optimal ones for OI. The error associated with the analysis, and therefore with the observational and sampling error will be presented. This error will be studied by means of analyses carried out with slightly different parameters, establishing the sensitivity, and hence the accuracy, of the derived variables. Special attention is given to the sensitivity associated with the guess of the mean field, since this sensitivity has not been studied before and have a large impact on the calculated  $w$ . Despite the study carried out in this chapter is qualitative, the results are rather interesting and will be necessary for the conclusions of the following chapters. In section C.2, the theoretical approach under optimal statistical interpolation will be exposed, together with the statistical requirements. The parameters used in OI for the present dataset will be also described and justified in that section. The sensitivity of the derived fields to small changes in the parameters of the OI is covered in section C.3. Finally, the partial conclusions of this chapter are presented in section C.4.

## **C.2 OPTIMAL STATISTICAL INTERPOLATION FORMULATION**

The goal of any data analysis is to predict properties of a variable using the information available from a finite number of discrete observations. Optimal Statistical interpolation considers the spatial coherence of the observations, which are considered as a random function of the position.

A set of  $n$  observations can be partitioned as follows:

$$\theta_i = \bar{\theta}_i + \tilde{\theta}'_i + \varepsilon_i = \bar{\theta}_i + \theta'_i, \text{ where}$$

$\bar{\theta}_i$  is the large scale mean, or background field;

$\tilde{\theta}'_i$  is the *true* increment or residual value of the variable  $\theta$ , this is the difference between the *true* value ( $\tilde{\theta}_i$ ) and the mean field:  $\tilde{\theta}'_i = \tilde{\theta}_i - \bar{\theta}_i$ ;

$\varepsilon_i$  is the observing error, that includes both the aliasing of the unresolved scales and the instrumental error; and

$\theta'_i = \tilde{\theta}'_i + \varepsilon_i = \theta_i - \bar{\theta}_i$  is the observed anomaly.

The large scale mean field is typically estimated by fitting a low order polynomial surface to the observations. The optimal mean field should be that one that produces an anomaly field that behaves like a stationary, zero-mean random function of the location. However, oceanographic dataset do not have enough data for statistical significant estimates of the large scale mean, and thereby the degree of the polynomial surface should be a compromise between incorporating as much large-scale signal as possible but keeping the polynomial degree low to avoid overshooting in the polynomial fit. The degree of the polynomial should be increased until the size of the observed anomalies is similar to the stations' grid. In physical terms, the mean field is removed from the analysis to avoid the masking of the small-scale residual field, mainly mesoscale activity, by the more energetic large-scale field. In the case of the western Alborán Sea, the mean field represents the structure of the western Alborán gyre.

In the set of analysis methods know as *distance weighting*, the predicted increments at the nodes of a regular grid are estimated as a linear function of the observed anomalies.

$$\hat{\theta}'_g = \sum_{i=1}^n w_{ig} \theta'_i = \underline{w}_g^T \cdot \underline{\theta}' = \begin{pmatrix} w_{1g} & \cdots & w_{ng} \end{pmatrix} \cdot \begin{pmatrix} \theta'_1 \\ \vdots \\ \theta'_n \end{pmatrix}$$

In order to find the appropriate value of the weighting coefficients, several methods could be used. If the spatial coherence of the observed field is considered, the most suitable method is the one denominated optimal statistical Interpolation (OI). In this method, the coefficients  $\{w_{ig}\}$  are found minimizing, in a statistical sense, the deviations between the prediction and the true field at the nodes of the grid, this is, requiring that the variance of the analyses error is a minimum with respect the choice of weights.

The variance of the analysis error is given by:

$$\langle e_g^2 \rangle = \langle (\hat{\theta}'_g - \tilde{\theta}'_g)^2 \rangle = \langle \tilde{\theta}'^2_g \rangle - 2 \underline{w}_g^T \cdot \langle \underline{\theta}' \tilde{\theta}'_g \rangle + \underline{w}_g^T \cdot \langle \underline{\theta}' \underline{\theta}'^T \rangle \cdot \underline{w}_g$$

On the right-hand side,  $\langle \tilde{\theta}'^2_g \rangle = \tilde{\sigma}_g^2$  denotes the variance of the true increment field,

$\underline{\tilde{g}}_g = \langle \underline{\theta}' \tilde{\theta}'_g \rangle = (\tilde{g}_{1g} \quad \cdots \quad \tilde{g}_{ig} \quad \cdots \quad \tilde{g}_{ng})$  the vectors of covariances in the second term of the right hand side of the previous equation; while the nxn matrix in the last term is the observation covariance matrix, which in the case where the observing error  $\varepsilon$  is the same for all the observations can be represented as:

$$\underline{\underline{\Upsilon}}_o = \underline{\underline{\tilde{\Upsilon}}} + \mathbf{I} \eta^2 = \begin{pmatrix} \tilde{\sigma}^2 + \eta^2 & \tilde{g}_{12} & \cdots & \tilde{g}_{1n} \\ \tilde{g}_{21} & \tilde{\sigma}^2 + \eta^2 & \cdots & \tilde{g}_{2n} \\ \vdots & \vdots & \ddots & \vdots \\ \tilde{g}_{n1} & \cdots & \cdots & \tilde{\sigma}^2 + \eta^2 \end{pmatrix}$$

Differentiating with respect to  $\underline{w}_g$  and equaling to zero, to minimize the variance of the analysis error, the following set of normal equations is obtained:



$$\underline{\underline{Y}}_{\circ} \cdot \underline{w}_g = \underline{\underline{\tilde{g}}}_g$$

If each side is divided by a suitable value of  $\tilde{\sigma}^2$ , the solution for the prediction of the anomalies at the nodes of the grid is:

$$\underline{\hat{\theta}}'_g = \underline{\rho}_g^T \underline{\underline{\Omega}}_{\circ}^{-1} \underline{\theta}', \text{ where}$$

$\underline{\rho}_g$  is the vector of autocorrelations between the increments at  $\mathbf{r}_g$  and  $\mathbf{r}_i$ .

$\underline{\underline{\Omega}}_{\circ}$  is the matrix of anomaly autocorrelations between all the observations points; with the diagonal elements equal to  $(1+\gamma)$ , where  $\gamma = \langle \varepsilon^2 \rangle / \langle \theta'^2 \rangle$  is the noise-to-signal variance ratio of the observed anomalies, and with the off-diagonal elements equal to the autocorrelations between the increments at  $\mathbf{r}_i$  and  $\mathbf{r}_j$ .

Since the correlations between the nodes of the new grid and the observations are unknown, a model for the correlation function  $\rho$  has to be assumed. This model is used to generate the off-diagonal elements of  $\underline{\underline{\Omega}}_{\circ}$  and  $\underline{\rho}_g$ . Hence, the predicted anomalies at the nodes of the grid could be written as follows:

$$\underline{\hat{\theta}}'_g = \begin{pmatrix} \rho_{1g} & \cdots & \rho_{ig} & \cdots & \rho_{ng} \end{pmatrix}_{(1 \times n)} \cdot \begin{pmatrix} (1+\gamma) & \cdots & \rho_{1i} & \cdots & \rho_{1n} \\ \vdots & \ddots & \vdots & \ddots & \vdots \\ \rho_{i1} & \cdots & (1+\gamma) & \cdots & \rho_{in} \\ \vdots & \ddots & \vdots & \ddots & \vdots \\ \rho_{n1} & \cdots & \rho_{ni} & \cdots & (1+\gamma) \end{pmatrix}_{(n \times n)}^{-1} \cdot \begin{pmatrix} \theta'_1 \\ \vdots \\ \theta'_i \\ \vdots \\ \theta'_n \end{pmatrix}_{(n \times 1)}$$

It is interesting to note that these optimal predicted anomalies  $\{\hat{\theta}'_g\}$  obtained in the OI schemes is the best linear unbiased estimator of  $\tilde{\theta}'_i$ , in the sense that the variance of the analysis error is a minimum with respect to the choice of weights. However, this

does not necessary implies the best possible analysis, in the sense that the validity of the prediction relays on the validity of the assumptions done.

Using the same mathematical developing, the analysis error for the observed variable that can be obtained as a by-product of the OI method [Bretherton et al., 1976] should be understood as a lower bound of the analysis error, an extension of this analysis error to the variables not linearly related with the observed variables is found in the work by *Gomis and Pedder* [2005].

### C.2.1 Scale selection

It has been said that one of the major objectives of any analysis is to minimize the effects of the aliasing of unresolved scales. In spite that OI was designed to minimize the variance of the analysis errors, the correlations model used could increase the aliasing error if its Fourier transform have components in the poorly resolved wavelengths, given that in such a case the analysis would attribute variance to those scales. This occurs for most of the correlation models used, given that the smallest scale represented in the model is larger than the smallest wavelength that can be properly resolved by the spatial distribution of the observations. This latter scale should be taken as  $\lambda_{\min} > 2 \cdot dx$ , where  $dx$  is the minimum distance between observations.

Moreover, this effect increase with smaller scales and therefore contribute in significantly to the analysis error in vertical velocity, geostrophic velocity, vorticity, and any variable obtained after differentiating the observed field. An approach to overcome this problem is to increase the degree of smoothing with a higher noise-to-signal variance ratio ( $\gamma$ ), however, this method has two majors inconvenient. Firstly, the objective character of the analysis is lost, since the changes in  $\gamma$  has to be done visually, increasing it until the analysis shows an *adequate* degree of smoothing. Secondly, it is not coherence with the assumptions of OI, where the *observational noise* is handled as an uncorrelated white noise, while the problem is related with the higher variance in the poorly resolved scales.

A more objective method to reduce this effect is archived by applying a low-pass filter to the mapped variable, with a cut-off length scale such that the well-resolved scales are retained, at least  $\lambda_{cut-off} > 2 \cdot dx$ . Notwithstanding, this reduction of the sampling error is at the expense of loosing spatial resolution, especially at the boundaries [Gomis and Pedder, 2005]. Numerically, the filtering is applied during the analysis, using a modified correlation model, derived from a 2-D convolution of a filter with the model for the sampled anomaly correlation.

Finally, it has to be said, that the OI used throughout this study is based on the work by Pedder [1993], implemented with an iterative method that yield the same results as the classical OI with the filter described above, but is faster, in computational terms.

### **C.2.2 Parameters used in optimal interpolation throughout this study**

In the previous paragraphs, the theoretical basis of OI has been described, pointing out all the necessary parameters required to use optimal statistical interpolation. Here, the values of the parameter used in OI with the data set described in section A.1.2 are described.

The first necessary assumption to apply OI is the decomposition of the observations into an anomaly and a large scale mean field that should behave like a stationary, zero-mean function of the location. Given that usually oceanographic data sets do not have enough observations to obtain a mean field with the appropriate statistical requirements, a model for the mean field has to be assumed. In the case of the western Alborán Sea, the strong curvature of the density front obtained from the raw density data indicates that the spatially variable mean should be represented by a polynomial and calculated by fitting the field to a polynomial function as follows:

$$\bar{\theta}_i = (a_n x_i^n + \dots + a_0) \cdot (a_n y_i^n + \dots + a_0) \quad n = 1, \dots, 4$$

In figure C.1, where the mean, anomaly and raw density fields for the first survey are shown for different polynomial fits, is observed as the size of the anomalies decrease with the degree of the polynomial.

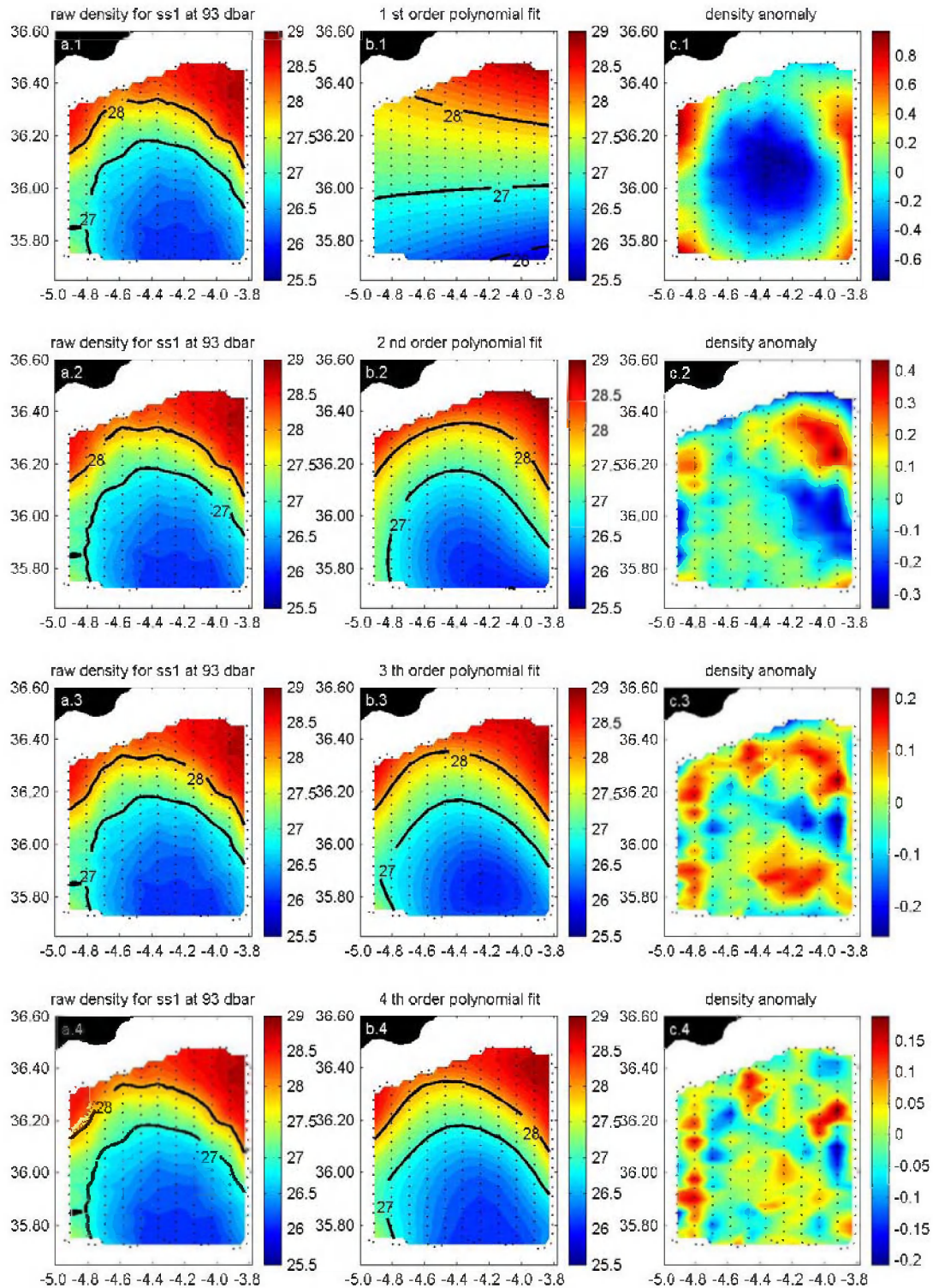


**Figure C.1.** Raw density data (a.n), mean field (b.n) and anomaly density field (c.n) for the first survey and polynomial of degrees  $n=1, 2, 3, 4$ .

With a polynomial fit of second degree, the mean field recovers most of the large-scale signal and the sizes of the anomalies are similar to the distance between observations along the east-west axis. A polynomial of third degree as mean field gives a size for the anomalies similar to the distance between along track stations, while for a polynomial fit of fourth degree, the size of almost all the anomalies is about the meridional distance between stations. Nevertheless, the spacing between adjacent meridional legs is about 10 km, and hence anomalies smaller than this should not be accepted, if the regular rule of thumb for using fitted polynomial surfaces as the large scale mean field is used. For the other surveys, similar results were obtained, and given that, throughout this study we will use a second order polynomial fit as the mean field.

Optimal statistical interpolation also requires the knowledge of the true correlations between the nodes of the new grid and the observations. Since the sampled data do not provide those correlations, they have to be estimated from a correlation model obtained after fitting a mathematical function to the correlations obtained between the observed anomalies. Since for an uncorrelated noise  $\tilde{\nu}_{ij} = \nu_{ij} \forall i \neq j$  and  $\sigma^2 = \langle \theta'^2 \rangle = \tilde{\sigma}^2 + \eta^2$ , the resulting sampling statistics provides an estimation of the true anomaly correlation times a constant, as indicated by:

$$\rho_k = \frac{1}{1+\gamma} \tilde{\rho}_k \quad (1)$$

To increase the number of observations that contribute to the mathematical fit, the model is assumed to be homogenous and isotropic, and thereby the correlations can be computed averaging the product of anomalies  $\theta'_i \theta'_j$  over all stations separated by a distance between  $R_k - \delta$  and  $R_k + \delta$ . It is interesting to point out that the isotropic assumption is valid in frontal zones given that the large scale mean field recovers most of the anisotropy imposed by the front.

In that way, the model chosen for the correlation is an isotropic Gaussian function of the distance between the observations:

$$\tilde{\rho}(R) = e^{-R^2/2L^2}, \text{ where } L \text{ is the characteristic scale.}$$

Although there is not guarantee that a chosen correlation model is realistic, the poor statistical significance of the fit does not justify a more sophisticated correlations model. Moreover, uncertainty in the estimated model's parameters is larger than the error associated with the particular choice of a correlation model. Using a 1<sup>st</sup> and 2<sup>nd</sup> order polynomial as mean field and fitting the observed anomalies to the correlation model, averaged over the water column, the two parameters  $L$  and  $\gamma$  were obtained for each survey (figure C.2 and table C.I). With a second order polynomial as mean field, and excluding the anomalous value obtained for the third survey, the mean value of the signal-to-noise ratio is  $\gamma = 0.015$ . Negative values for  $\gamma$  were also obtained (table C.I), obviously, there is no sense for such values, just meaning unrealistic estimations, consequence of the small actual value of  $\gamma$ . A detailed study, at different depth levels and for the different cruises, of the estimations of  $\gamma$  showed small positive and negative values within the order of magnitude of the average value obtained in table C.I. The low values obtained are characteristics of strong frontal regions, where the signal, mainly mesoscale activity for the anomaly field, is more energetic than the sampling noise due to the aliasing of the unresolved scales. With the same dataset *Gomis et al.* [2001] assumed a compromise value of  $\gamma = 0.02$ .

Polynomial degree	Ss1	Ss2	Ss3
1	-0.063	-0.050	0.071
2	0.040	-0.005	0.43

**Table C.I.** Noise-to-signal ratio  $\gamma$  obtained from the least-square fit to the correlation model of figure C.2



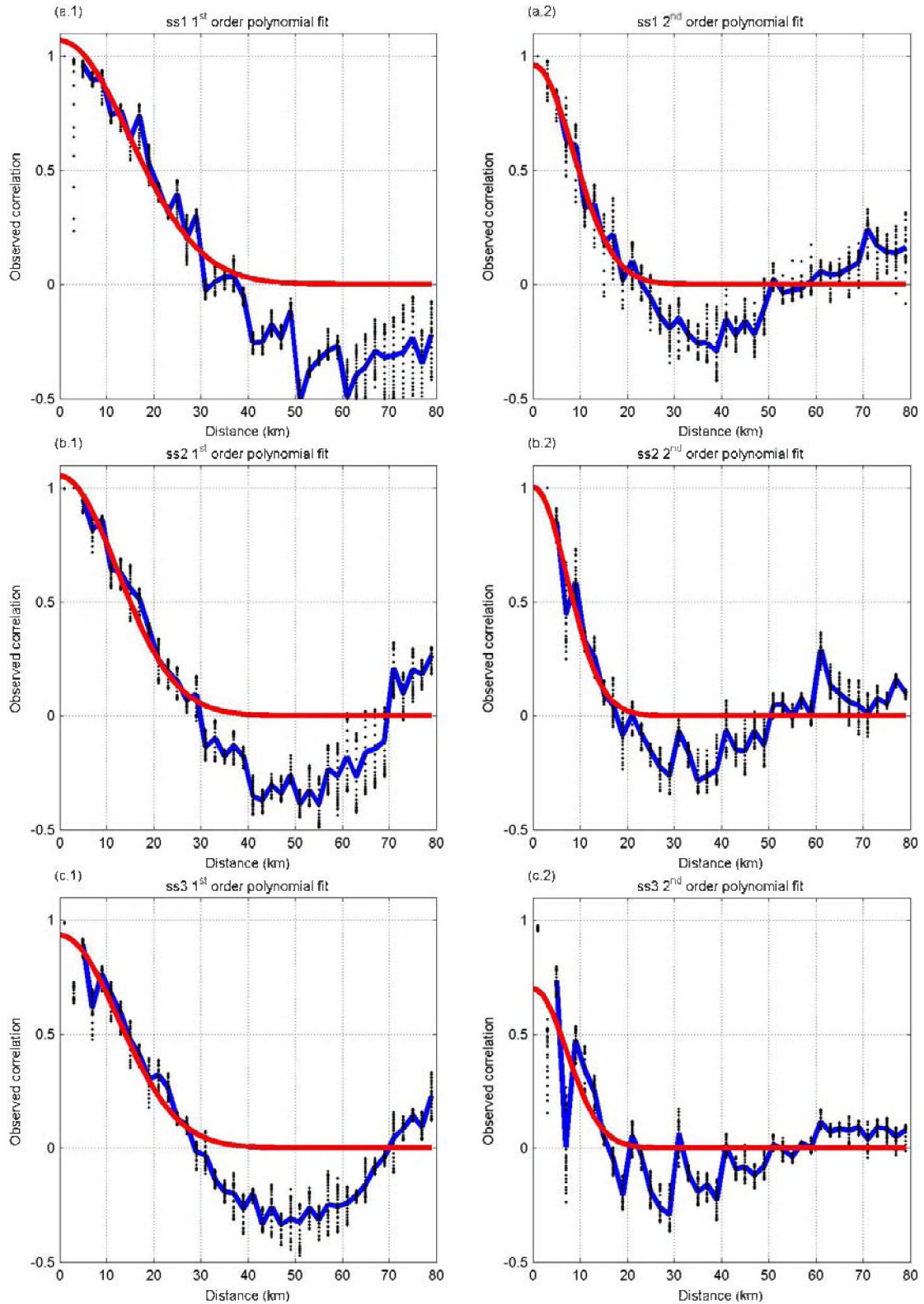


**Figure C.2.** Least-squares fit of the correlation model for dynamic height in surveys (a.n) ss1, (b.n) ss2 and (c.n) ss3, where n=1, 2 is the degree of the polynomial used as mean field. The red line is the fitted true correlation, the black dots are the observed correlations, and the blue line is the correlations averaged throughout the water column.



The correlation length scale  $L$  estimated by the least-square fit to the correlation model assumed, gave a broad variety of scales (figure C.2), ranging from 12 km for the third survey and a polynomial of 4<sup>th</sup> degree as mean field to 22 km for the first survey and a polynomial of 1<sup>st</sup> degree as mean field.

The exploration carried out and the statistics computed from the dataset have permitted to establish the *optimal* values of the noise-to-signal ratio and the correlation length scale as  $\gamma = 0.01$  and  $L = 20$  km.

Regarding the length scale of the filter used for scale selection, the value  $\lambda_{cut-off} = 20$  km has been assumed because the distance between adjacent meridional tracks is about 10 km. Some authors would have suggested  $\lambda_{cut-off} = 4 \cdot dx = 40$  km, but a smaller value has been assumed, to avoid even larger areas of high uncertainty near the boundaries of the sampled region.

### C.3 SENSITIVITY STUDY

It has been demonstrated that for an accurate ascertainment of derived variables, a carefully objective analysis should be done. Despite of that, the estimations of the different parameters needed for OI are not robust, in the sense that a range around the *optimal* value of a given parameter is within the uncertainty of the processes used to establish the parameters needed for optimal statistical interpolation. This occurs even in cases where a large amount of data is available. Given that, is useful and interesting to analyze the sensitivity of a derived variable as vertical velocity to changes in the parameters of need by OI. This exploration will be carried out by comparing different estimations of  $w$  with the optimal diagnosed vertical velocity field obtained with the parameters:  $L = 20$  km,  $\gamma = 0.01$ ,  $\lambda_{cut-off} = 20$  km and a 2<sup>nd</sup> order polynomial as mean field. Vertical velocity has been calculated with the Q-vector form of the omega equation (see D.3.1), although vertical velocities diagnosed using the DFI technique (see D.3.2) have yielded very similar results.

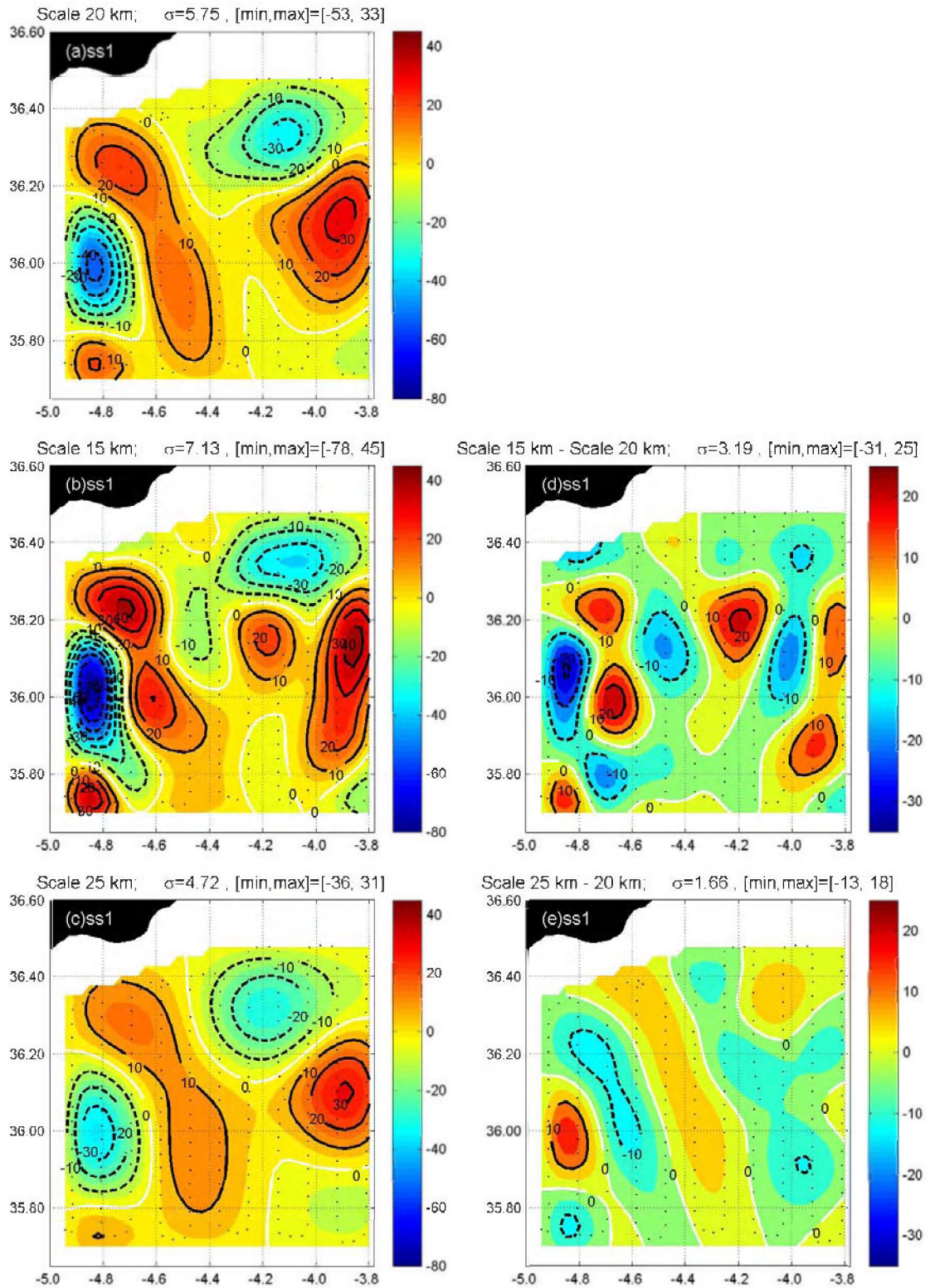


**Figure C.3.** Vertical velocity diagnosed at 90 dbar from analysis of dynamic height for ss1 and different values of the correlation scale: (a)  $L=20$  km, (b)  $L=15$  km and (c)  $L=25$ ; (d) represents (b)-(a) and (e) represents (c)-(a). The other analysis parameters were kept as the optimal ones. For each map, the standard deviation and the maximum and minimum value of the represented field have been included.

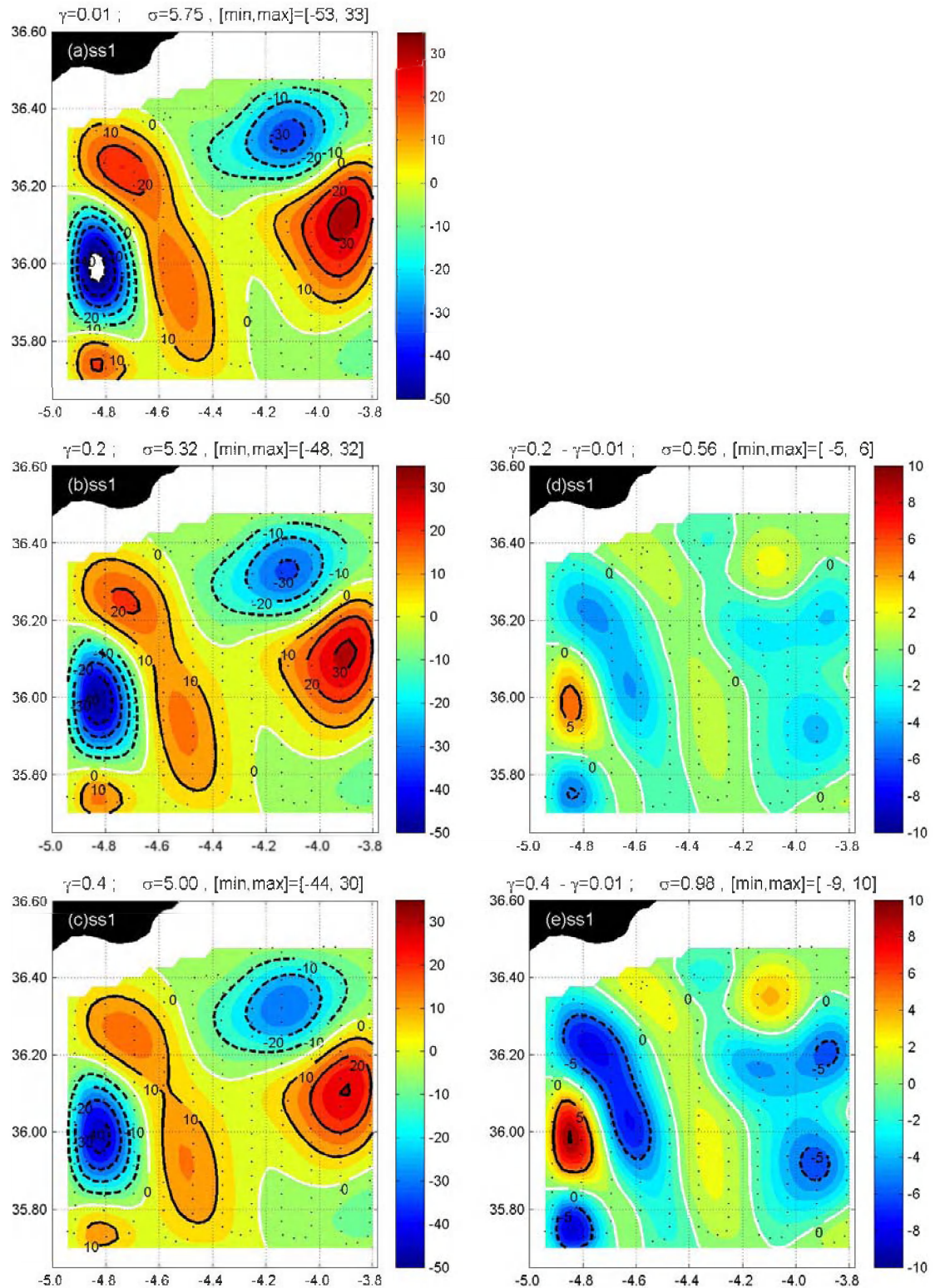


**Figure C.4.** Vertical velocity diagnosed at 90 dbar from analysis of dynamic height for ss1 and different values of the noise-to-signal ratio: (a)  $\gamma=0.01$ , (b)  $\gamma=0.2$  and (c)  $\gamma=0.4$ ; (d) represents (b)-(a) and (e) represents (c)-(a). The other analysis parameters are the optimal ones. For each distribution, the standard deviation and the maximum and minimum value of the represented field have been included.



As show by figure C.2 and table C.I there is a range of values around the chosen optimal characteristic scale and noise-to-signal ratio within the uncertainty of the fitting to the correlation model described in C.2. To test the importance of changes in the characteristic scale, figure C.3 shows  $w$  obtained from analysis of dynamic height with the *optimal* parameters except the characteristic scale that has been set to  $L=20$  km,  $L=15$  km and  $L=25$  km. It is observed as the overall shape of the distribution of the vertical velocity field is similar for the three different analyses. The analysis with smaller correlation scale shows a more patchy distribution, as indicated by the new upwelling spots determined at  $36.2^\circ\text{N}$ ,  $4.2^\circ\text{W}$  and  $36.2^\circ\text{N}$ ,  $4.4^\circ\text{W}$  (figures C.3a and C.3b) with a size about the distance between the meridional legs. A smoother  $w$  distribution is obtained with the analysis carried out with larger characteristic correlation scale (figure C.3c), maintaining the main upwelling/downwelling cells at the same position that in the diagnosis carried out with the optimal parameters. Though the general distribution of the vertical velocity is comparable, the magnitude of the estimated vertical velocity at each grid point is significantly different among the three different analyses. The standard deviation of  $w$  at 90 dbar increased in a 24% for  $L=15\text{km}$ , and decrease in a 18% for  $L=25\text{km}$ . A corresponding decrease and increase of the minimum and maximum values of the field is also observed with fluctuations up to 47% in the minimum value and 27% in the maximum. The standard deviation of the difference field (figures C.3d and C.3e) represents about 55% of the *optimal* field for  $L=15$  km, and 28% for  $L=25$  km.

The overall shape of the  $w$  distribution remains very similar if the noise-to-signal ratio is modified (figure C.4). The standard deviation of the field at 90 dbar shows as the calculated  $w$  becomes smoother as the noise-to-signal ratio is increased. Nevertheless, the sensitivity of  $w$  is small, a change of the noise-to-signal ratio to  $\gamma=0.2$  only produces a decrease in the standard deviation of 7.5%, while the difference field only represents a 10% of the *optimal* vertical velocities.

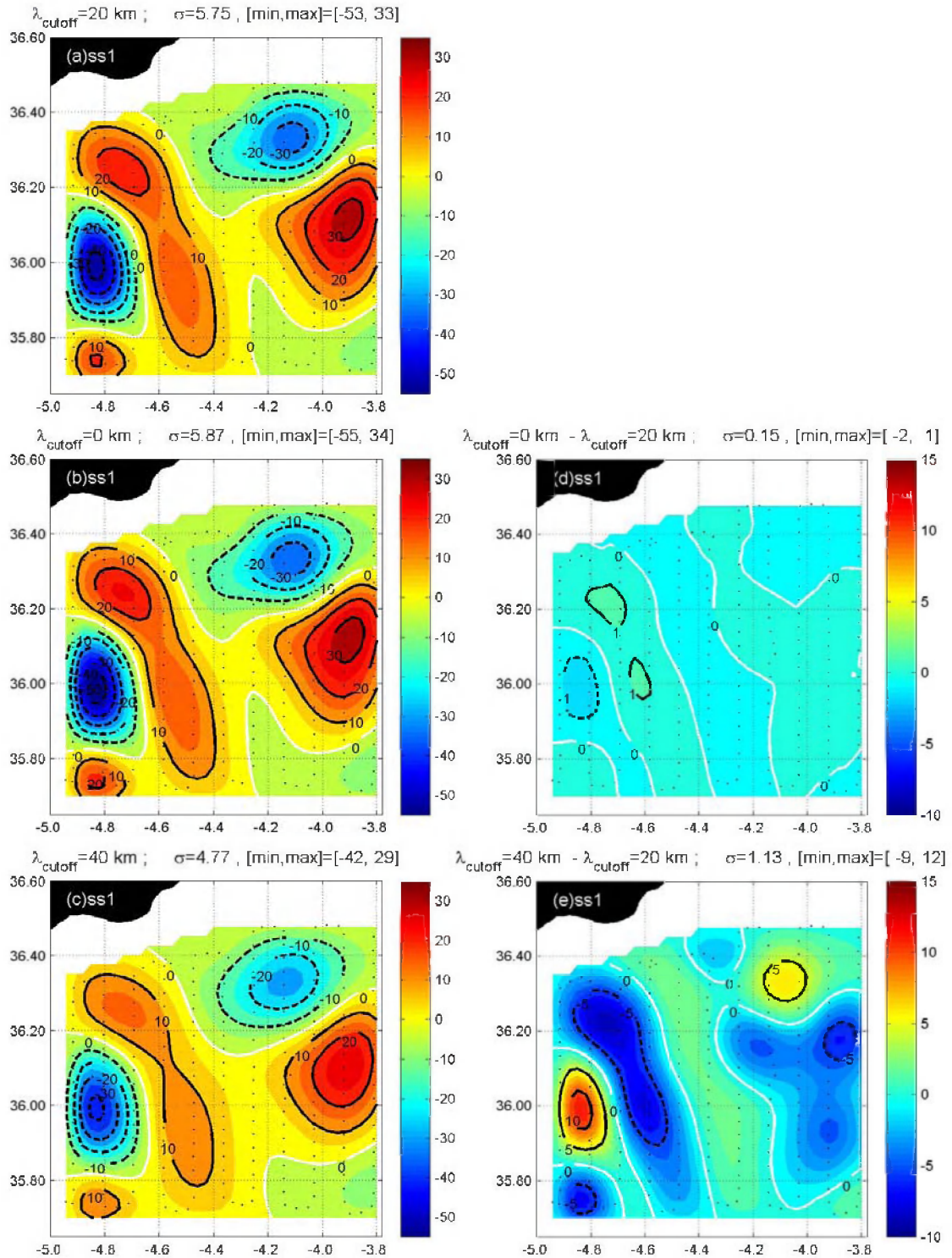


**Figure C.5.** Vertical velocity diagnosed from analysis of dynamic height for ss1 and different values of the cut-off scale: (a)  $\lambda_{\text{cut-off}} = 20 \text{ km}$ , (b)  $\lambda_{\text{cut-off}} = 0 \text{ km}$  and (c)  $\lambda_{\text{cut-off}} = 40 \text{ km}$ ; (d) represents (b)-(a) and (e) represents (c)-(a). The other analysis parameters are the optimal ones. For each map, the standard deviation and the maximum and minimum value of the represented field have been included.

For larger changes in the noise-to-signal ratio,  $\gamma=0.4$  (figure C.4c), the decrease in the magnitude of the  $w$  field remains small, with a decrease of 13% in  $\sigma$ , whilst the standard deviation of the difference field just represents the 17% of the *optimal* estimated vertical velocity.

The sensitivity of the vertical velocity field to changes in the cut-off length-scale  $\lambda_{cut-off}$  is small, keeping the overall shape of the distribution, although increasing/reducing slightly the magnitude of the vertical velocity. The differences with respect the *optimal* field are less than 2 m/day if no filter is applied (figure C.5b,d), while differences around 10 m/day and a 17% smaller standard deviation were found when the filter applied had a larger scale,  $\lambda_{cut-off}=40$  km.

Let's now inspect the uncertainty due to the chosen mean field. This step is critical, given that the first necessary assumption for using optimal statistical interpolation is the decomposition of the observed field into a mean field and an anomaly field. The mean field should guarantee that the anomalies behave like a stationary, zero-mean random function of the location, however there is not an objective way to select the degree of the fitted polynomial used as mean field and therefore values around the *optimal* one are possible. Contrarily to that found for the noise-to-signal ratio, the correlation scale and the cut-off scale, changes in the mean field not only affect the magnitude but also the overall distribution of the vertical velocity, as can be observed in figure C.6, where vertical velocity fields calculated from analyses of dynamic height from the first survey and obtained with different polynomial degrees as mean field are exposed. There is still a subtle similarity between the four different estimations, give that some of the main upwelling/downwelling cells remain similar although with differences in its shape and position. The most notable changes occur between the diagnoses obtained using a first and a second order polynomial degree as mean field (figures C.6a, C.6b and C.6e).



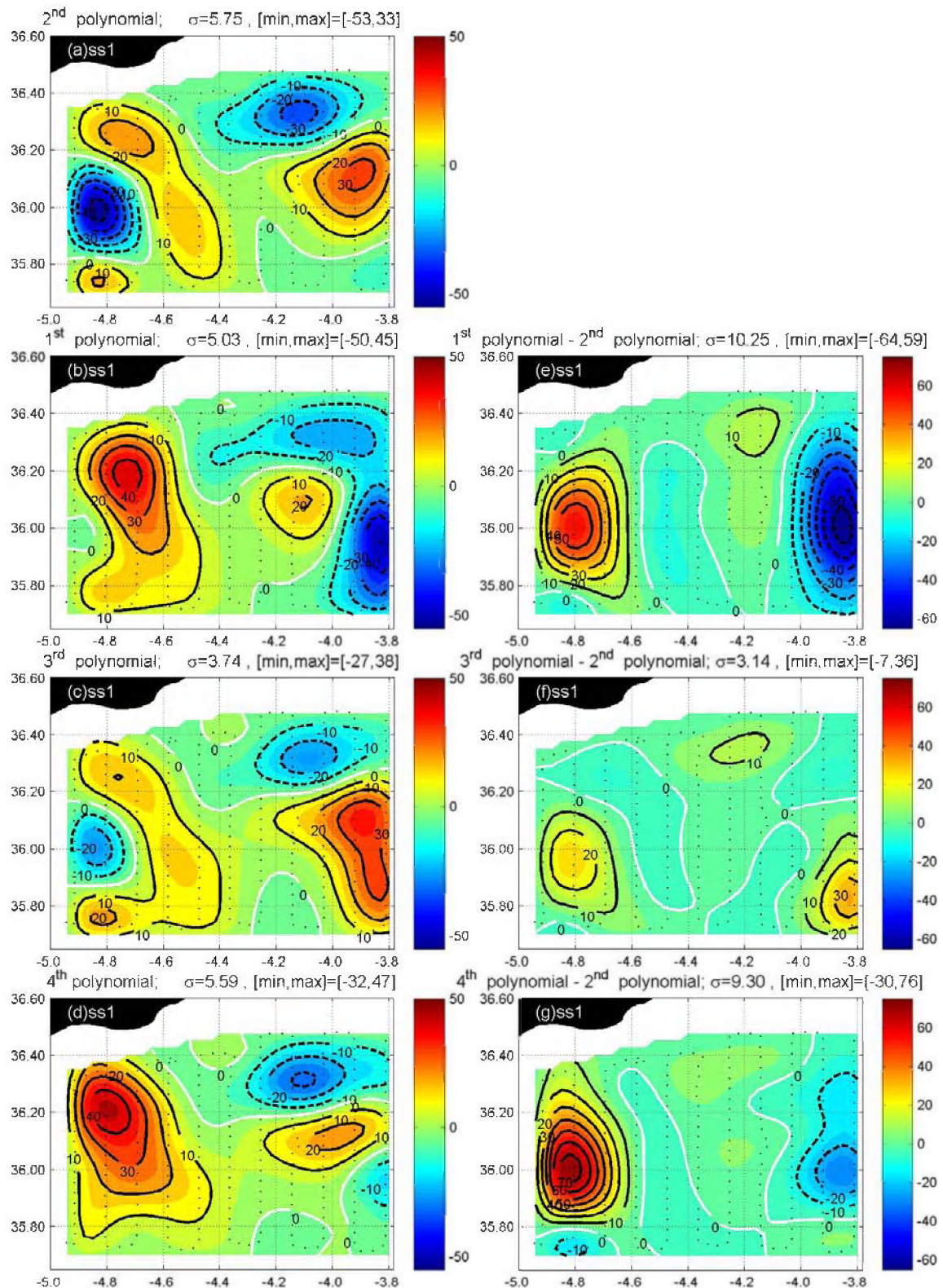


**Figure C.6.** Vertical velocity diagnosed from analysis of dynamic height for ss1 and different polynomial degree as mean field: (a)  $n=2$ , (b)  $n=1$ , (c)  $n=3$  and (d)  $n=4$ ; (e) represents (b)-(a) and (f) represents (c)-(a) and (g) represents (d)-(a). The other analysis parameters are the optimal ones. For each map, the standard deviation and the maximum and minimum value of the represented field have been included.

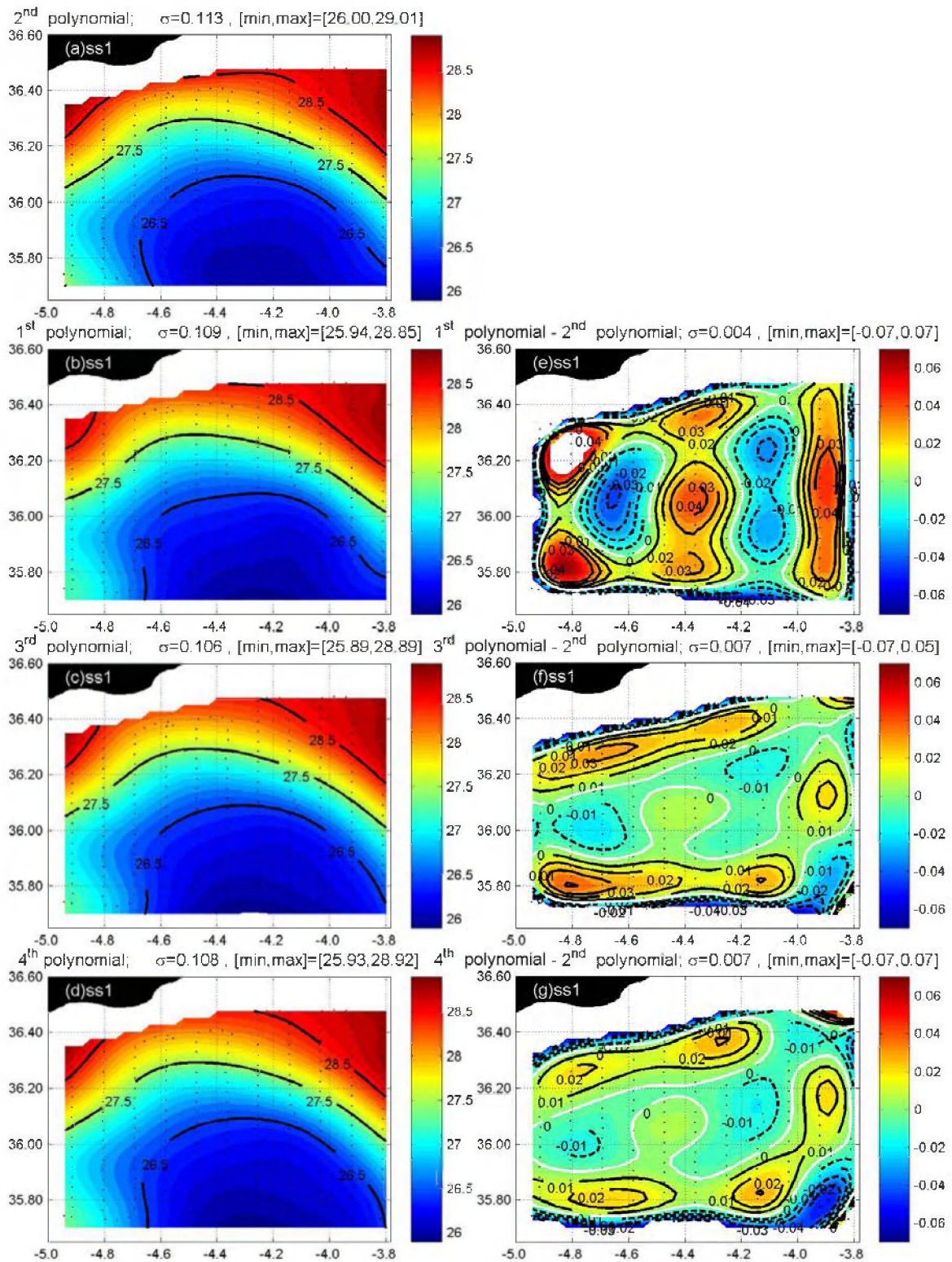


**Figure C.7.** Analysis of density for ss1 and different polynomial degree as mean field: (a)  $n=2$ , (b)  $n=1$ , (c)  $n=3$  and (d)  $n=4$ , (d) represents (b)-(a) and (e) represents (c)-(a). The other analysis parameters are the optimal ones. For each map, the standard deviation and the maximum and minimum value of the represented field have been included.



The difference field between both estimations represents almost 180% of the standard deviation of the *optimal* vertical velocity field, with a significant change in the position of the main upwelling cell, the disappearance of the downwelling centered at 36°N, 4.8°W and a variation in the range of the vertical velocity field. Between the vertical velocity fields derived with the polynomial of second and third degree as mean field the number of upwelling/downwelling patches kept similar (figure C.6a, C6.c and C6.f). However, the sensitivity is still high as manifested by the fact that the difference field still represents more than the 55% of the *optimal* fields, there is a reduction of 35% in the standard deviation and the maximum and minimum of the field have suffered a significant decrease. The differences of the *optimal* fields with respect the computations done assuming a polynomial of fourth degree as mean field are high, with significant changes in the shape and number of upwelling/downwelling cells, as observed in the difference field that represents more than 160% of the standard deviation of the *optimal* diagnosed vertical velocity (figure C.6g).

As a counterpart to the significant sensitivity of the vertical velocity field to changes in the polynomial used as mean field, figure C.7 shows that the differences in density for analyses using different degrees of polynomial are small. Within the interior domain, the differences are around  $\pm 0.04 \text{ kg/m}^3$ , and the difference field represents less than 6% of the *optimal* field. The sensitive of the density field to changes in the noise-to-signal-ratio, the correlation and the cut-off scale are weaker than those due to changes in the mean field and therefore are not shown.

Given the strong impact of the changes in some of the objective analysis parameters to the derivation of vertical velocities, a similar study has been done for the other two SeaSoar surveys. The comparison after changes in the noise-to-signal-ratio, the correlation, and cut-off scale are analogous to those found for the first survey. However, changes in the polynomial used as mean field have yield slightly different results, since weaker sensitivity than that described for the first survey has been found. The differences between the  $w$  field obtained with a polynomial of first and second

degree are about 95% of the *optimal* field for the second survey and 112% for the third survey. While the differences for the comparison of the diagnosis with polynomials of third and second degrees represents 23% of the *optimal* field for the second survey and 47% for the third survey.

For the first survey the change in the polynomial used as mean field modifies not only the magnitude but also the number and shape of the upwelling/downwelling patches; while for the third survey, the number of the upwelling/downwelling patches keeps nearly constant, with minor changes in its shape and position, as can be observed in figure C.8.

The overall major difference between the three small-scale surveys is the dynamical situation found in the western Alborán Sea. During the first survey, the WAG was within the sampled domain, and therefore the areas of maximum advection of vorticity, and thus maximum forcing for vertical velocities (see D.3-Vertical velocity), were at the boundaries of the sampled domain. While in the third survey, and as consequence of the displacement of the WAG, the areas of higher advection of vorticity were at the centre of the sampled region. If the mean field is not optimal, and given that each choice of a mean field will displace a different amount of forcing of the vertical velocity field onto the anomaly field, the asymmetry imposed by the geographical distribution of observations at the boundaries has stronger impact on the first survey than on the third. These results suggest that the sensitivity to the polynomial used as mean field is strongly enhanced by the boundary effect. The boundary effect in the context of objective analysis should be understood as the increased sampling error due to the asymmetry imposed by the distribution of the measurement in the sides of the sampled domain.

In order to show the impact of the boundary effect on the estimated  $w$ , a reduced analysis has been done. In that reduced analysis, a smaller domain has been used, where the eastern and western most sections were eliminated from the observations.

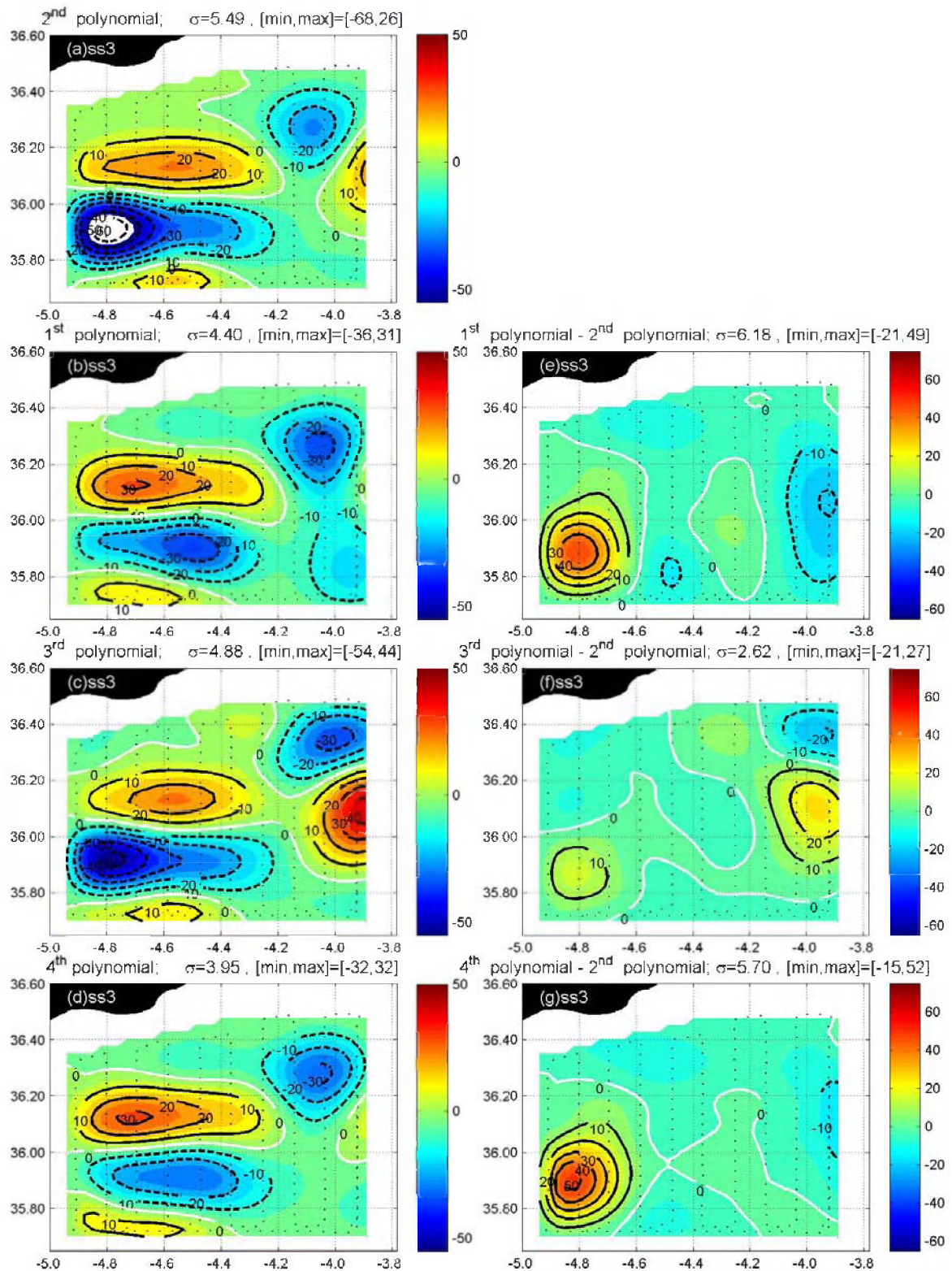


**Figure C.8.** Vertical velocity diagnosed from analysis of dynamic height for ss3 and different polynomial degree as mean field: (a)  $n = 2$ , (b)  $n = 1$ , (c)  $n = 3$  and (d)  $n = 4$ ; (e) represents (b)-(a) and (f) represents (c)-(a) and (g) represents (d)-(a). The other analysis parameters are the optimal ones. For each map, the standard deviation and the maximum and minimum value of the represented field have been included.



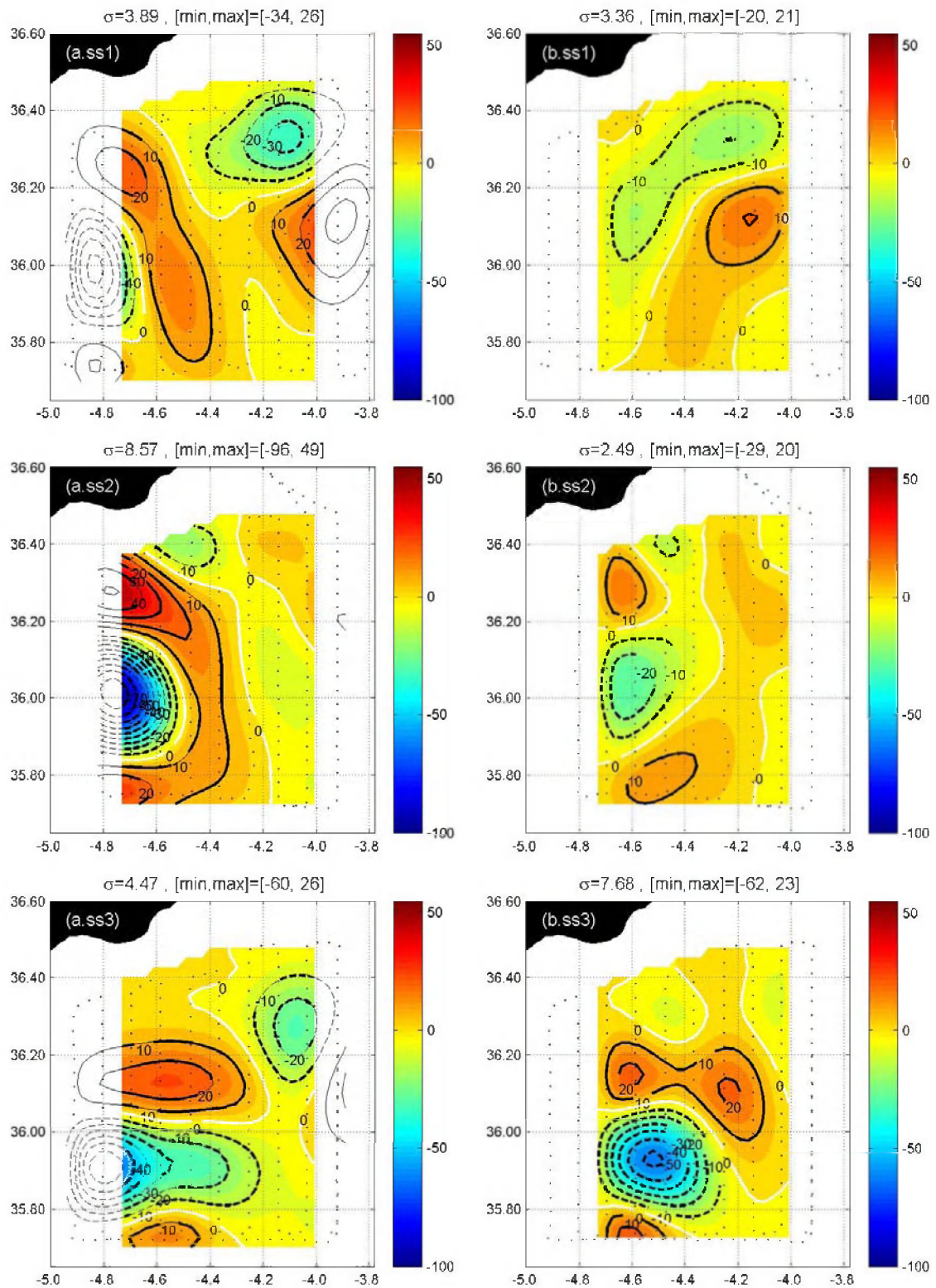


**Figure C.9.** Vertical velocities (m/day) diagnosed from the (a.survey) complete dataset and (b.survey) a reduced dataset within the contoured region. Survey=ss1, ss2 and ss3. The standard deviation and the maximum and minimum value of the represented field have been included in each figure.



Within the small domain, the full analysis should be less affected by the boundary effect than the analysis carried out just in the reduced domain, and therefore a comparison of the reduced and the extended analysis within the small domain should give a qualitative idea of the impact of the boundary effect; figure C.9 shows the analyses and its reduced version for the three surveys carried out with the SeaSoar. As suggested before, for the first survey the impact of the boundary effect is stronger than in the other two surveys as noted by the fact that the estimated vertical velocity in the extended and small domain has large differences, without coincidences neither in the number of upwelling/downwelling patches nor in the position of them, and with an intense decrease in the maximum and minimum values of the vertical velocity field. For the second survey, within the small domain the number and size of the patches remain similar, though with a reduction in the magnitude of the vertical velocities. For the third survey, the test on the boundary effect has yielded the expected results: the boundary effect on the third survey has the weakest impact on the computed vertical velocities since in the small domain the structure and range of the  $w$  field is similar to that obtained with the complete dataset but still with significant differences (figure C.9).

## C.4 CONCLUSIONS

In order to maximize the signal-to-noise content of the analyzed data and avoid the amplification of small-scale noise in the differentiation process necessary for computing variables as vertical velocity, an interpolation technique, based on statistics of the sampled data have been used. The scheme used here belongs to this set of schemes and follows the principles of Optimal Statistical Interpolation (hereafter OI). Despite that the dataset do not permit robust estimations of the parameters, compromises values have been chosen for the required objective analysis parameters: a 2<sup>nd</sup> order polynomial fit as the large scale mean field, a noise-to-signal ratio of  $\gamma=0.01$ , a length scale  $L= 20$  km for the Gaussian correlation model and  $\lambda_{cut-off}=20$  km for the convoluted filter. These parameters have been used for the four surveys, except the

cut-off length scale that for the last survey was set to  $\lambda_{cut-off}=40$  km, since the distance between adjacent meridional tracks was twice than that for the SeaSoar surveys.

The uncertainty associated with both, the aliasing of unresolved scales and the discrete character of the sampling, has been studied throughout the sensitivity of the vertical velocity to changes in the parameters used in the optimal statistical interpolation. In spite that the density and geopotential fields seems to be well retrieved from the observations, the derivatives of the geopotential field are seriously contaminated by the aliasing errors due to the unresolved scales, because in the differentiation, the high wave components of the anomaly field are amplified. Small changes in the length scale of the spatial correlation model and the observational error do not have large impact on the vertical velocity as shown by the comparative study carried out, where quite similar distributions were found, with just minor differences in the magnitude. Similarly, an analysis without applying the convoluted low-pass filter, or applying it with larger cut-off scale, does not represent major changes neither in the magnitude of the vertical velocities nor in the shape and distribution of the upwelling and downwelling areas. However, the size of the *trustable* inner domain decrease with the increase of the cut off length scale and therefore realistic values should be used.

The inaccuracy in determining the mean field has stronger impact on the vertical velocity, yielding artificial, although spatially coherent features in the vorticity and vertical velocity fields. A non-optimal choice of the mean field produces an anomaly field that is not really a stationary, zero-mean random function of the location, and thereby the large scale field mask part of the signal from the anomaly field. The uncertainty due to the choice of the main field was strongly enhanced by the boundary effect and the impact of boundary effect in the objective analysis changes considerably depending on the dynamical conditions found. The influenced of the boundary effect on the density and vertical velocity fields was tested for each survey carrying out analyses where the number of available observations was modified. The uncertainty associated

with the boundary effect is higher in critical cases, as during the first survey, where the maximum advection of vorticity was at the boundaries.

The uncertainty due to observational and sampling error is independent of the theoretical approach used to calculate the vertical velocities, as indicated by the fact that the vertical velocities diagnosed from the omega equation and those obtained from the assimilation into the PE model, have the same sensitivity to changes in the parameters used in the optimal statistical interpolation analyses.

The results presented here are based on a qualitative study, being difficult to estimate quantitatively the restrictions that the sampling and observational errors impose on the vertical velocity fields and vertical fluxes. However, these results imply some concern for studies required to understand the upper ocean mesoscale processes and its impact on marine ecosystems; among others, those where balance assumptions are tested, or where the geostrophic fields are compared with kinematics estimations of horizontal velocities from observed ADCP velocities; or even where the vertical motion is used to estimate net vertical biogeochemical fluxes.

Fortunately, the fact that slightly similar shapes were found throughout the sensitivity studies to the OI parameters give confidence to establish that the diagnosis, at least, permit to ascertain the order of magnitude, sign and size of the upwelling and downwelling patches. These results are in agreement with the comparison with the lagrangian estimations of  $w$  presented in chapter E.

---

**D.-THREE-DIMENSIONAL  
CIRCULATION ASSOCIATED WITH  
AN INTENSE OCEANIC FRONT:  
THE WESTERN ALBORÁN SEA**

---

## D.0 ABSTRACT

Vertical velocities cannot be measured, at least in an eulerian framework; therefore diagnosing methods should be used. We present and describe vertical velocities computed using two different techniques, the **Q**-vector form of the quasi-geostrophic omega equation and a digital filtering initialization of a primitive equation model. These techniques have been applied to four consecutive high-resolution surveys of the western Alborán gyre carried out during fall 1996. In the Western Alborán Sea two very different waters masses are found, the convergence between them gives rise to intense density fronts and energetic mesoscale features. Associated with those hydrographic conditions there was a strong density front in the upper 200 dbar, with gradients up to  $2\sigma_t$  in 20 km and an associated velocity jet with velocities reaching 120 cm/s. In this energetic upper ocean, the associated vertical velocities were as high as -100 m/day and 70 m/day. The results show that the main contribution to the mesoscale vertical motion is the geostrophic advection of geostrophic vorticity, while the comparison between both techniques has provided an estimation of the diagnosis error due to the theoretical approach. The differences are well within the uncertainty due to sampling and observational error. In spite of the high vertical velocities found, simulated trajectories have shown small net vertical motion in the area, less than 5 m/day in the interior of the WAG, and nearly 20 m/day outside the WAG. These small net descending and ascending velocities are coherent with the quasi-geostrophic theory, which assumes vertical displacements much smaller than horizontal displacements. The potential vorticity conservation is shown through the correspondence of geostrophic vorticity and vertical velocity along the simulated trajectories.

## D.1 INTRODUCTION

The intention of this chapter is to obtain and describe the three-dimensional circulation, including the vertical velocities, associated with a strong density front, in particular, the one placed on the western Alborán gyre. For such purpose two different techniques are used, the Q-vector form of the QG omega equation and an assimilation into a PE ocean model. This chapter is thereby essential to undergo the comparison with in-situ data that will be addressed in the following chapter. Due the complexity and impact of the objective analysis on the estimations of the vertical velocity, chapter *C.-Analysis methods* was entirely devoted to this topic, including the processes followed to obtain the parameters for the objective analysis used here, as well as a sensitivity study of the influence of changes in those parameters onto the derived fields. The remainder of this chapter is organized as follows: Section D.2 describes briefly the front and the geostrophic circulation in the frontal area. The vorticity fields are described in section D.3. The two different diagnosed techniques are explained in section D.4, where the vertical velocity fields are also described and discussed. In section D.5, the trajectories computed with the three-dimensional velocity field are described. Finally, section D.6 discusses the results and presents the conclusions.

## D.2 TWO DIMENSIONAL CIRCULATION AND VORTICITY

The overall circulation in the Alborán Sea for the first survey is depicted in figure A.1. Three remarkable features are observed: two anticyclonic vortexes and an intense eastward jet. The western bowl of warm surface waters ( $T > 21^\circ\text{C}$ ) constitutes the western Alborán gyre. The warm waters of Atlantic origin ( $T > 21^\circ\text{C}$ ,  $S < 36.6$ ) that are found in the inner part of the gyre are due to the longer residence time and isolation of recirculating waters. Eastern of the Alborán ridge there is another bowl of warm waters that constitutes the semi-permanent anticyclonic vortex denominated eastern Alborán gyre (EAG), and surrounding the northern side of the WAG is observed the Atlantic jet (AJ), characterized by colder surface Atlantic waters ( $T < 19.5^\circ\text{C}$ ). The AJ is



consequence of the density differences between the recent advected Atlantic waters and the surface Mediterranean waters.

The geostrophic and ADCP velocities show the anticyclonic circulation of the WAG (figures B.6 and B.7), with maximum ADCP velocities up to 140 cm/s at the surface (12 dbar) and up to 90 cm/s at 90 dbar. Separating the northern colder and saltier MW from the southern fresher and warmer MAW there is a strong front. Part of this density front is associated with the more superficial AJ and part with the northern boundary of the WAG, since the AJ and the WAG both coexist at 90 dbar. The horizontal distributions of density at 90 dbar (figure B.5) corroborate the existence of an intense front separating the dense waters in the north from the bowl of light waters in the south. At this depth, the horizontal gradient of the front is  $1.8 \text{ kgm}^{-3}$  in 20 km, this is, about  $2 \text{ kgm}^{-3}$  in one Rossby radius, a gradient comparable to the strongest gradients found in the world's oceans.

During the two weeks after the first survey, there was a change in the dynamic situation, mainly due to an increase in NACW (see B.-Hydrographic conditions of an intense oceanic front: the Western Alborán Sea), however, the large-scale circulation remained similar. The time evolution is summarized as follow: pushed by the AJ, the WAG was drifted to the east, at the same time that it reduced its size and was centered southern. Figure B.5 shows the meandering of the front between the MAW and the MW, for the second and third survey, the ADCP (figure B.7a) and geostrophic velocities at  $36^{\circ}\text{N}$  had higher eastward component. The meandering, that began on the 6<sup>th</sup> October, continued during the third survey, as show the horizontal distributions of density and geostrophic velocity for that survey. The hydrographic data for the last survey (figure B.5.ctd) shows like the WAG was pushed eastward by the AJ at the same time that it was constrained to the southeast. It is important to note that the time evolution of the WAG during the four surveys was not due to the internal slow quasi-geostrophic dynamics of the WAG, since an important change in the inflow of Atlantic waters and a spring tide forced the time evolution.

The geostrophic relative vorticity field associated with the circulation found in the western Alborán Sea was computed from the geopotential field, using the equation obtained after taking cross derivatives in the horizontal geostrophic equations:

$$\zeta_g = \frac{\partial v_g}{\partial x} - \frac{\partial u_g}{\partial y} = \frac{1}{f} \left( \frac{\partial^2 \Phi}{\partial x^2} + \frac{\partial^2 \Phi}{\partial y^2} \right) = \frac{1}{f} \nabla_h^2 \Phi \quad (2)$$

The horizontal distributions of geostrophic vorticity, scaled by the local planetary vorticity  $f$  are shown in figure D.1. At 90 dbar, a depth representative of the surface circulation in the Alborán Sea, the geostrophic vorticity ranged between  $-0.7f$  and  $0.50f$ . During the four surveys, the bowl of negative vorticity that corresponds to the western Alborán gyre was observed, but stronger anticyclonic vorticity was found in the inner part of the gyre given that curvature vorticity and shear vorticity both contribute with negative sign to the local geostrophic vorticity. Significant changes in the distribution of the areas with anticyclonic vorticity were found as consequence of the changes in the shape of the WAG that occurred during its evolution, as described in chapter B.

Surrounding the anticyclonic vorticity bowl there were patches of cyclonic vorticity; those at the north side of the WAG corresponded to the positive shear vorticity associated with the AJ and with the cyclonic meandering. Places where both components of the vorticity contribute with the same sign gave maximum cyclonic vorticity, as can be observed in the northeast corner of the first survey (figure D.1b.ss1). At 15 dbar, the time evolution of the cyclonic vorticity follows the time evolution of the AJ; this is, during the first survey (figure D.1a.ss1) the maximum in cyclonic vorticity was found at the northeast corner; during the second and third surveys (figure D.1a.ss2) the maximum of cyclonic vorticity is associated with the increase in the strength of the AJ and therefore with its shear, being this maximum placed in the neighborhood of the strait of Gibraltar, where the AJ was stronger. The southern displacement of the AJ is also revealed in the vorticity fields. The patches of cyclonic vorticity southern than the AJ, correspond to the meandering of the borders of

the WAG, due to the temporal variability induced in the western Alborán sea by the changes in the inflow through the strait of Gibraltar.

The size of the anticyclonic vorticity bowl became smaller with depth since the negative vorticity is mainly related with the WAG, its magnitude decreased from up to  $-0.8f$  at 15 dbar to  $-0.1f$  at 200dbar. The cyclonic patches showed strong coherence down to the 200 dbar, with  $0.7f$  at 15 dbar down to  $0.1f$  at 200 dbar. In the northern hemisphere the flow is inertially stable if the absolute vorticity of the flow is positive, otherwise, the occurrence of inertial instability would trigger inertially unstable motions, mixing the fluid and reducing the shear until the absolute vorticity is positive again.

Given that the vertical motion in the Alborán Sea is mainly due to differential geostrophic vorticity advection (figure D.4), the horizontal distributions of geostrophic velocities and vorticity indicate where the maximum vertical velocities will be, this will be described widely in the next section. The main length scale of variability for the density field, and the geopotencial field, is associated with the WAG and to the meanders of the AJ, the later being around 30/40 km. The geostrophic vorticity fields are also dominated by the same scales, as observed in the horizontal distributions of relative vorticity.

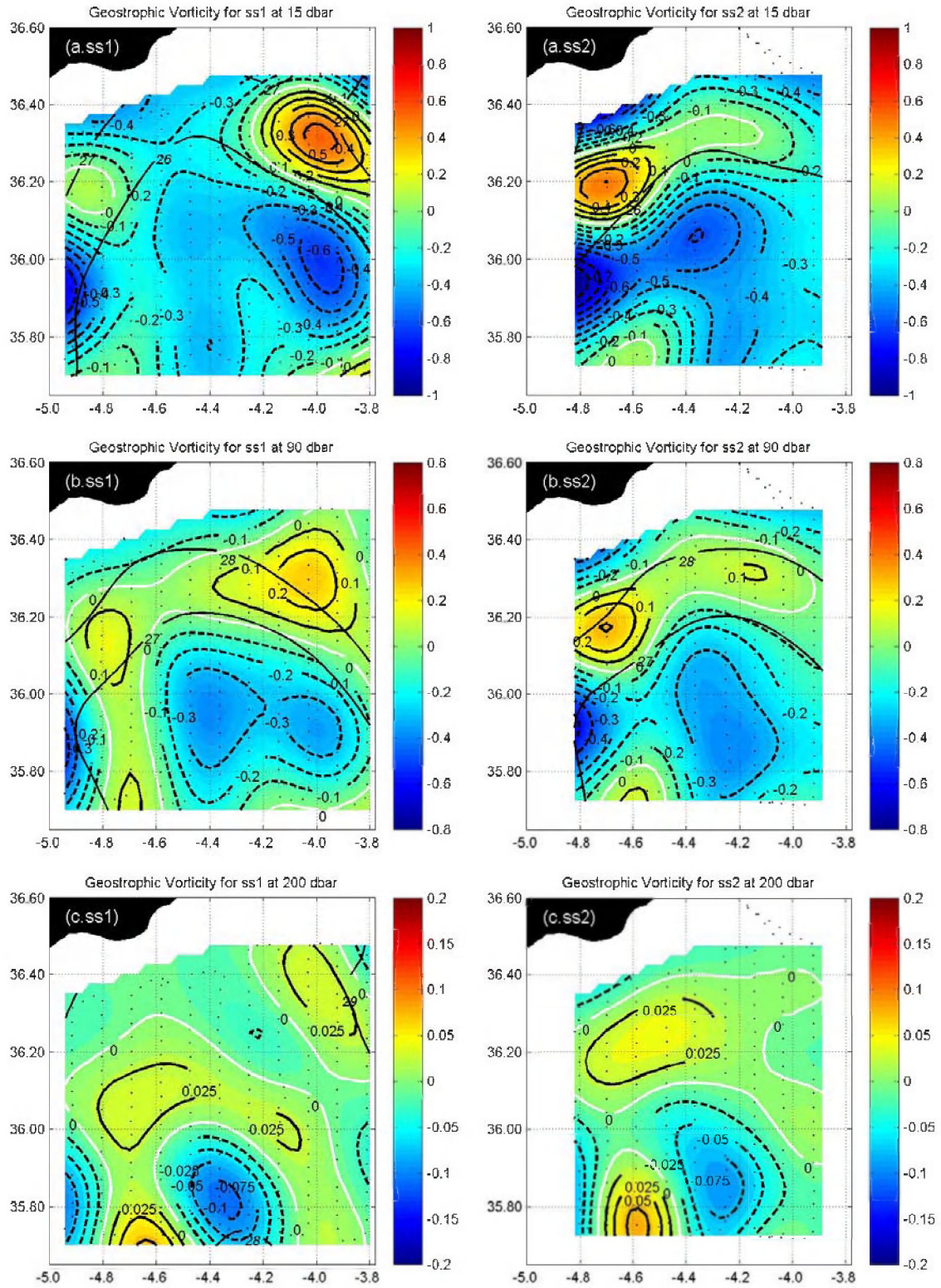


**Figure D.1:** Horizontal distributions of geostrophic vorticity, scaled by the local coriolis parameter,  $(\zeta/f_0)$  at (a) 15 dbar (b) 90 dbar and (c) 200 dbar for the (ss1) first, (ss2) second, (ss3) third and (ctd) fourth surveys.



D.-THREE-DIMENSIONAL CIRCULATION ASSOCIATED WITH AN INTENSE OCEANIC FRONT: THE WESTERN ALBORÁN SEA

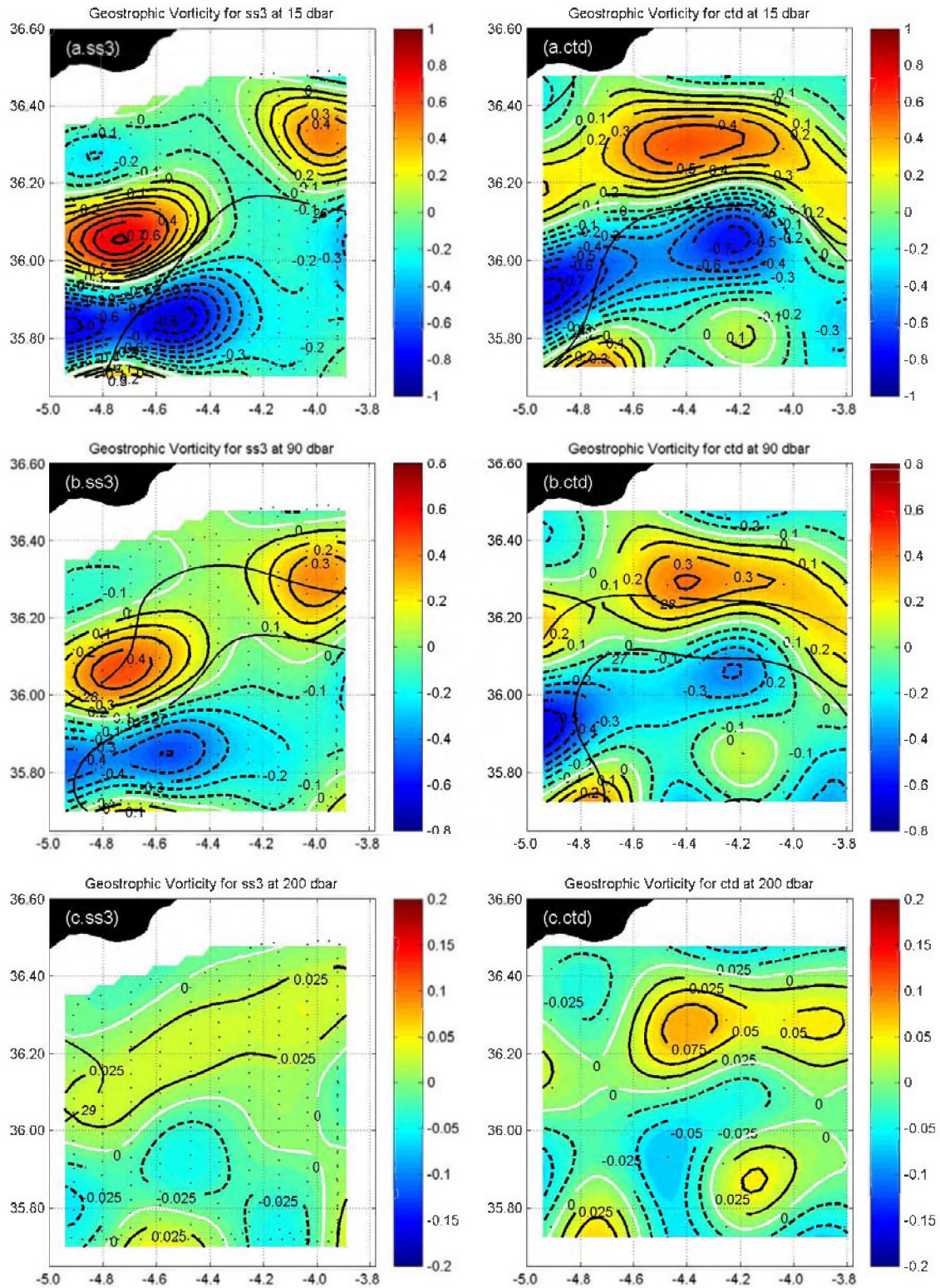
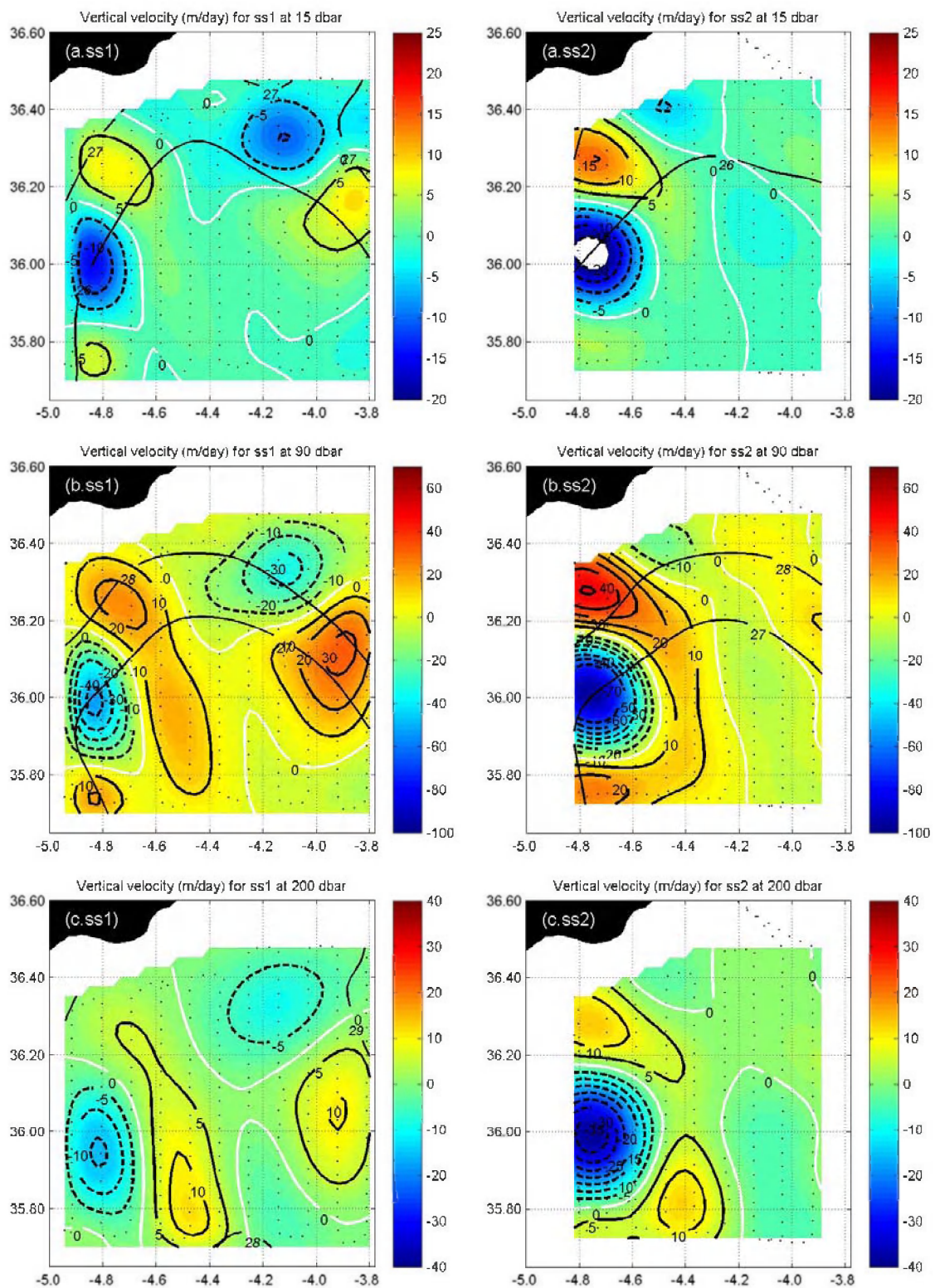


Figure D.1: (continued).



**Figure D.2:** Horizontal distributions of vertical velocity (m/day), at (a) 15 dbar (b) 90 dbar and (c) 200 dbar for the (ss1) first, (ss2) second, (ss3) third survey and (ctd) fourth surveys.



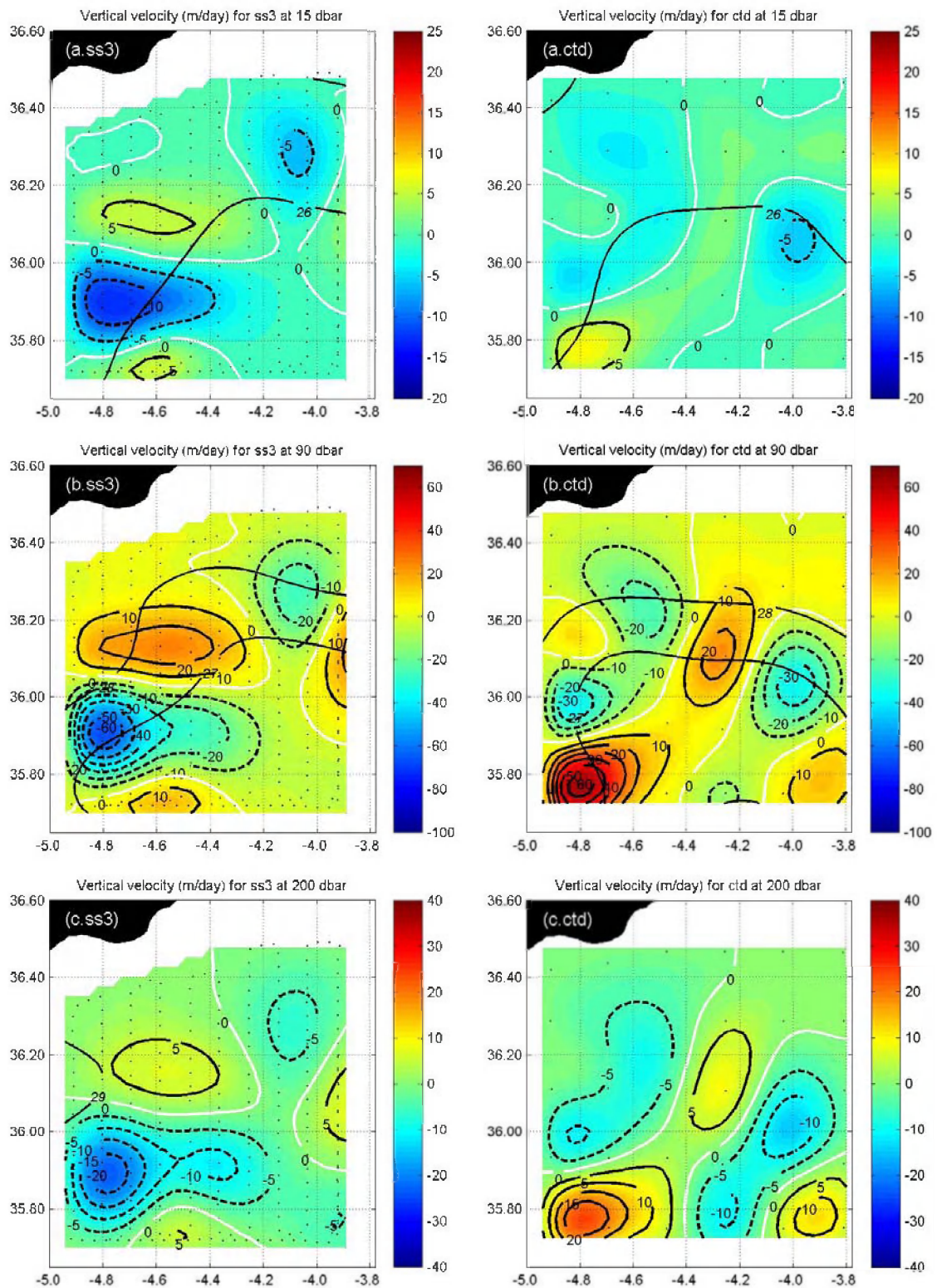


Figure D.2: (Continued)

## D.3 VERTICAL VELOCITY

### D.3.1 Omega equation

The slow time evolution (time scale  $\gg 1/f$ ) of mesoscale features is driven by the geostrophic advection of density and momentum. This advection modifies the initial fields and hence the geostrophic and hydrostatic balance could be broken. Since the ocean at scales larger than the Rossby radius is almost in geostrophic and hydrostatic balance, the density field must be modified through the vertical velocity field to keep both balances valid. The key point to understand the way the ocean adjusts to changes, when these changes are slow, are the departures from geostrophic, even though these are small, leading to what is known as the quasi-geostrophic theory. Under this framework, the vertical velocity field is the requirement to ensure that the changes in the density field during the time evolution of mesoscale features will keep the thermal balance valid. The slow evolution of a mesoscale feature can be described, from the point of view of the quasi-geostrophic theory, as a process, that although tending towards geostrophic and hydrostatic balance, is continuously altered. This complex tendency to a balance can be written in a mathematical sense [*Hoskins et al.*, 1978; *Hoskins et al.*, 1985b; *Holton*, 1992]. The horizontal momentum equations and the vertical momentum equation together with the hydrostatic relation may be written as follows:

$$\frac{D_g u_g}{Dt} - f v_a = 0, \quad (3.1 \text{ 1a})$$

$$\frac{D_g v_g}{Dt} + f u_a = 0, \quad (3.1 \text{ 1b})$$

$$\frac{\partial p}{\partial z} = -\rho g, \quad (3.1 \text{ 1c})$$

where  $\frac{D_g}{Dt} = \frac{\partial}{\partial t} + u_g \frac{\partial}{\partial x} + v_g \frac{\partial}{\partial y}$ , is the geostrophic advection operator.

The horizontal velocity can be divided in two contributions: the geostrophic and the ageostrophic ( $u_a, v_a$ ) components. The ratio between both contributions is assumed to be small,  $|\vec{V}_a|/|\vec{V}_g| \cong \varepsilon$ , since in quasi-geostrophic theory the Rossby number  $\varepsilon = \frac{U}{fl} \ll 1$ .

If just the geostrophic advection is considered in the thermodynamic equation, this can be approximated as follows:

$$\frac{D_g \rho}{Dt} + w \frac{\partial \rho}{\partial z} = 0 \Rightarrow \frac{1}{\rho_0} \frac{D_g}{Dt} \frac{\partial \rho}{\partial z} + N^2 w = 0, \quad (3.1 2)$$

where  $N = \sqrt{-\frac{g}{\rho_0} \frac{\partial \rho}{\partial z}}$  is the Brunt-Väisälä frequency.

The quasi-geostrophic vorticity equation is obtained combining the horizontal momentum equations,  $\frac{\partial}{\partial x}[Y \text{ Momentum Eqn.}] - \frac{\partial}{\partial y}[X \text{ Momentum Eqn.}]$ , and using the

fact that the geostrophic wind is no-divergent:

$$\frac{\partial \zeta_g}{\partial t} = -\vec{V}_g \cdot \nabla \zeta_g + f \frac{\partial w}{\partial z}, \quad (3.1 3)$$

where  $\zeta_g = \frac{\partial v_g}{\partial x} - \frac{\partial u_g}{\partial y} = \frac{1}{f \rho_0} \nabla^2 p = \frac{1}{f} \nabla^2 \phi$  is the geostrophic vorticity. The vorticity

equation relates the local changes in geostrophic vorticity to both, the advection of geostrophic vorticity by the geostrophic velocities and the gain/lost of vorticity due to the stretching/shrinking term.

Defining the pressure tendency by  $\chi = \partial p / \partial t$ , the vorticity and thermodynamic equations can be re-written as:

$$\nabla^2 \chi = -\vec{V}_g \cdot \nabla (\nabla^2 p) + f^2 \rho_0 \frac{\partial w}{\partial z} \quad (3.1 4)$$

$$\frac{\partial \chi}{\partial z} = -\vec{V}_g \cdot \nabla \left( \frac{\partial p}{\partial z} \right) + \rho_0 N^2 w \quad (3.1 5)$$

To obtain a diagnose equation for the vertical velocity that uses the information contained in the thermodynamic and vorticity equations, the time derivatives between both equations should be cancelled. The pressure tendency could be eliminated from the previous equations by taking the horizontal Laplacian of (3.1.5) and the vertical derivate of (3.1.4) respect to  $z$ :

$$\frac{\partial}{\partial z} \nabla^2 \chi = - \frac{\partial}{\partial z} \vec{V}_g \cdot \nabla (\nabla^2 p) + f^2 \rho_0 \frac{\partial^2 w}{\partial z^2}$$

$$\nabla^2 \frac{\partial \chi}{\partial z} = - \nabla^2 \left[ \vec{V}_g \cdot \nabla \left( \frac{\partial p}{\partial z} \right) \right] + \rho_0 N^2 \nabla^2 w.$$

The term containing  $\chi = \partial p / \partial t$  could be cancelled between both equations by reversing the order of the operators in the left hand side of the previous equations. Therefore, the vertical velocity necessary to keep valid the balance between the geostrophic advection of vorticity and density can be written as:

$$N^2 \nabla^2 w + f^2 \frac{\partial^2 w}{\partial z^2} = - \frac{1}{\rho_0} \nabla^2 \left[ \vec{V}_g \cdot \nabla \left( \frac{\partial p}{\partial z} \right) \right] + \rho_0 \frac{\partial}{\partial z} \left[ \vec{V}_g \cdot \nabla (\nabla^2 p) \right] \quad (3.1.6)$$

The two terms on the right hand side of equation (3.1.6) are associated with the two components of the vertical velocity: the along isopycnal advection and the local isopycnal displacement. Local isopycnal displacement is related to the in-situ change of the isopycnals' depths, while along isopycnal advection is induced by the small horizontal departures from the geostrophic velocity (ageostrophic horizontal velocity) that push water parcels out of its isopycnal. Water parcels in their aim to keep its density constant, experiment vertical excursions, either upward or downward. In addition, the first term can be identified as corresponding to the vertical velocity associated with the advection of density, while the second one corresponds to the advection of vorticity.

The right-hand side of equation 3.1.6 can be defined as the components of the  $\vec{Q}$  vector [Hoskins et al., 1978]:

$$\vec{Q} = 2 \frac{g}{\rho_0} \left( \frac{\partial \vec{u}_g}{\partial x} \cdot \nabla \rho, \frac{\partial \vec{u}_g}{\partial y} \cdot \nabla \rho \right),$$

yielding the final  $\vec{Q}$ -vector form of the omega equation:

$$N^2 \nabla^2 w + f^2 \frac{\partial^2 w}{\partial z^2} = \nabla \cdot \vec{Q}$$

The important usefulness of the omega equation is that given suitable boundary conditions the vertical velocity field can be we can obtained from knowledge of the geopotential field, since the  $\vec{Q}$ -vector equation is a Poisson equation in three dimensions, where the forcing and coefficients are just determinate by the density and geostrophic velocity fields. After breaking the omega equation as a set of simultaneous finite difference equations, these equations are solved with a suitable boundary conditions [Leach, 1987; Tintoré et al., 1991; Pollard and Regier, 1992; Allen and Smeed, 1996b].

The omega equation has been solved using a relaxation scheme, given that this method has been demonstrated to be successful in solving poison three-dimensional equations. Although two different bottom boundary conditions can be used to solve the omega equation, here Neumann bottom boundary conditions have been used because at 300 dbar the velocities in the Alborán Sea are dominated by its geostrophic part, and therefore the flow is divergence-free:

$$\left. \frac{\partial w}{\partial z} \right|_{z=300} = 0$$

Comparison between vertical velocities computed with this bottom boundary condition and those estimated with Dirichlet boundary conditions ( $w|_{z=300} = 0$ ) does not show



significant differences in the horizontal distribution of the vertical velocity fields but show differences in the magnitude of the vertical velocity of  $\pm 5$  m/day, intensifying both the upwelling and the downwelling patches. Minor differences, less than  $\pm 2$  m/day, between the vertical velocities calculated using Neumann and those using Dirichlet as lateral boundary conditions were observed. These differences were restricted to a strip 5 km wide around the boundary. In the present study Dirichlet lateral boundary conditions have been used:

$$\left. \frac{\partial w}{\partial x} \right|_{x=x_{west}} = \left. \frac{\partial w}{\partial x} \right|_{x=x_{east}} = 0,$$

$$\left. \frac{\partial w}{\partial y} \right|_{y=y_{north}} = \left. \frac{\partial w}{\partial y} \right|_{y=y_{south}} = 0$$

### D.3.1.1 First survey

In figure D.2, the vertical velocity fields obtained using the omega equation are presented. It is observed in the first survey that the vertical motion is dominated by alternating patterns of upwelling and downwelling along the path of the Atlantic jet and the boundary of the WAG. There is a strong downwelling pattern at the western side of the domain, with velocities up to  $-50$  m/day at 90 dbar, the depth where the maximum vertical velocities are found. This downwelling is associated with the meander found at  $36.0^\circ\text{N}$ ,  $-4.95^\circ\text{W}$  in the density field (figure B.5 b). Eastern and downstream of this downwelling pattern, and related with the trough that extends diagonally between  $36.20^\circ\text{N}$ ,  $4.90^\circ\text{W}$  and  $35.90^\circ\text{N}$ ,  $4.6^\circ\text{W}$  (figure B.5b), there is an upwelling patch that extends north-south throughout the sampling area with vertical velocities up to 30 m/day. Downstream along the AJ, there is one more downwelling/upwelling cell, associated with the meander at the northwest side of the WAG and with the advection of geostrophic vorticity by the Atlantic jet.

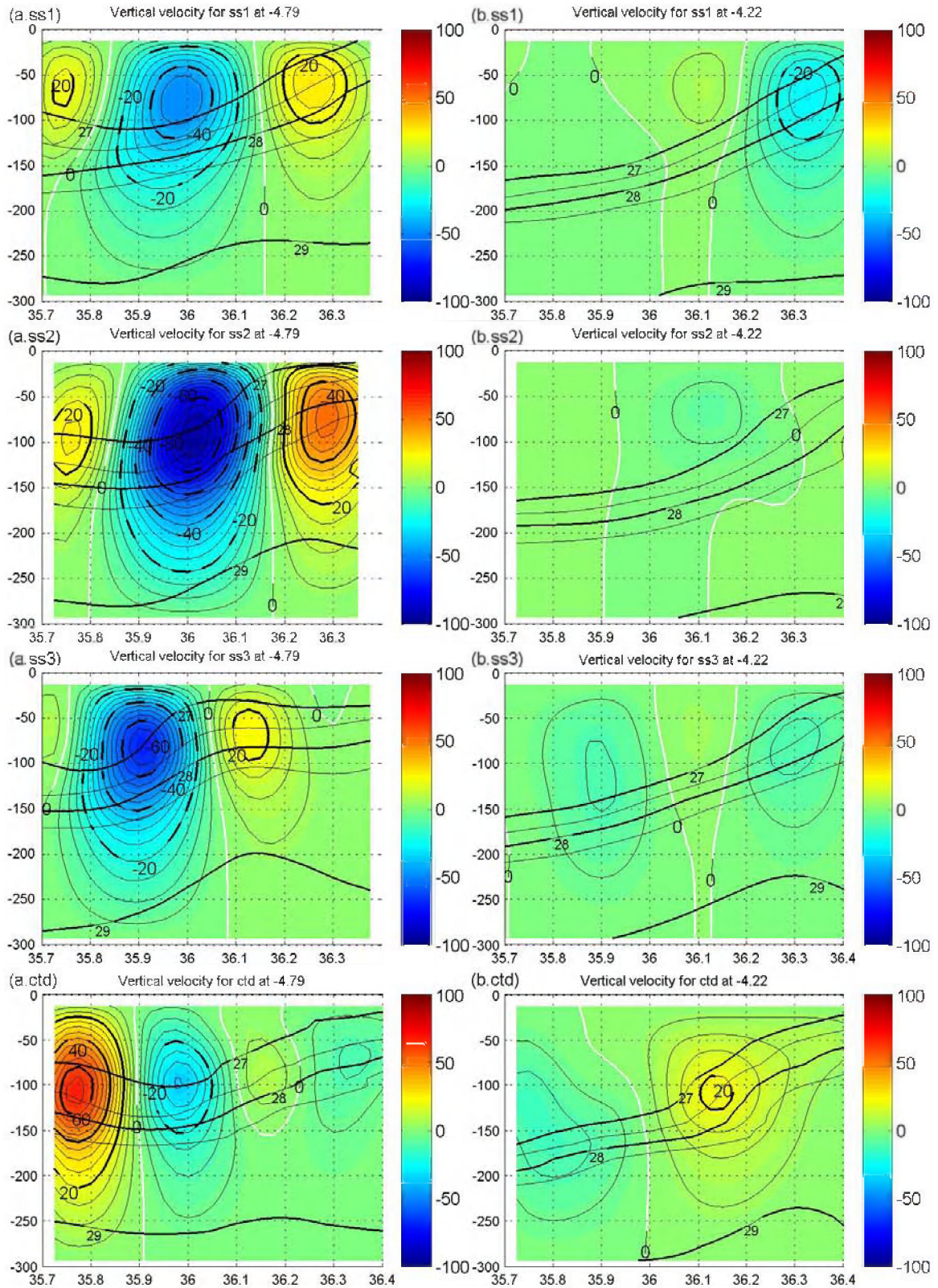


**Figure D.3:** South-north sections of  $w$  (m/day) along (a)  $4.79^\circ\text{W}$  and  $4.22^\circ\text{W}$  (b) for the (ss1) first, (ss2) second, (ss3) third and (ctd) fourth survey. The 26, 27 and 28  $\text{kg/m}^3$  isopycnals are overlaid for reference.

The horizontal length scales of the vertical velocity fields are similar to those for the geostrophic relative vorticity, and they are around 30 km, the length scale associated with the meandering of the WAG's rim. The weak vertical velocities found within the WAG are consistent with an eddy that is not growing. At 200 dbar, the vertical velocity field shows similar structure than that found at 90 dbar, although with weaker velocities, between  $-20$  m/day and  $10$  m/day. The cause of this weakening corresponds to the lower density gradients found at this depth. The vertical distribution of  $w$  at the western side,  $4.8^\circ\text{W}$  (figure D.3), shows as the alternative patch of positive and negative  $w$  extends coherently down to 300 dbar, with the maximum occurring between 80 dbar and 110 dbar, the level where the density field presents the stronger gradients, and therefore where the forcing in the omega equation is maximum. Inside the interior of the gyre, the vertical velocities are within the  $\pm 5$  m/day interval, a range that can be considered within the noise level, indicating an anticyclonic gyre in its mature state, as evidenced in the vertical section that crosses the inner part of the WAG, at  $4.22^\circ\text{W}$  (figure D.3b.ss1).

The vertical velocity fields do not completely follow the advection of vorticity, since contributions from the horizontal laplacian of the density advection are also necessities in a non-stationary dynamics as the one found in the western Alborán Sea. Although the term in the forcing of the omega equation is really the differential advection of vorticity, it has been used just the advection of vorticity since it is more intuitive and help to understand the physical mechanism causing vertical motion in the western Alborán sea.

The density advection in the area is small and hence there is high correlation between the vertical motion, described in the previous paragraph, and the vorticity advection field,  $V_g \cdot \nabla(\zeta_g + f)$  (figure D.4). The main contributions to the vorticity advection were associated with changes in curvature, and for that reason the stronger upwelling and downwelling signals were found along the AJ and in the rim of the WAG. Given that the

relative importance of the vorticity advection with respect the horizontal advection of density decrease with depth in the ocean, the correlation between the vorticity advection and the vertical velocity goes from 0.74 at 20 dbar to 0.38 at 280 dbar (figure D.5).

### **D.3.1.2 Time evolution of the vertical velocity field**

The successive surveys manifested a time evolution of the  $w$  field in concurrence with the displacement of the WAG and the meandering of the AJ. During the second survey, the alternating upwelling and downwelling structure remained (figure D.2 b). The downwelling patch at the eastern side of the domain ( $4.7^\circ\text{W}$ ,  $36^\circ\text{N}$ ) became larger, at the same time that intensified, reaching vertical velocities up to  $-97$  m/day at 90 dbar. The upwelling patch that during the first survey was eastern than this downwelling area modified its structure, wrapping completely the downwelling area at the same time that increased its maximum values up to 50 m/day. These changes were related with the meandering of the northern boundary of the western Alborán Gyre, and the associated changes in the structure of the vorticity advection. At 90 dbar, the vorticity distribution of the first survey was characterized by a bowl of negative vorticity (the WAG) surrounded by a band of positive vorticity, while during the second survey, and as consequence of the meandering of the AJ, the surrounding belt of positive vorticity was interrupted at  $35.9^\circ\text{N}$ ,  $4.7^\circ\text{W}$  by a patch of negative vorticity,  $-0.6f$ , that connected with the bowl of negative vorticity. This change in vorticity, coupled with the meandering of the WAG and the AJ, which produced changes in the geostrophic currents enhanced the negative advection of vorticity and therefore the downwelling. During the second survey, the gradients of vorticity at the eastern part of the domain became weaker since the WAG acquired a more circular shape and the advection of vorticity decreased. Consequently, at the eastern side of the sampled domain there were significant differences with respect to the first survey, the downwelling/upwelling cell disappeared; being the eastern part of the domain occupied with weak vertical



velocities, lower than  $\pm 5$  m/day. During the second survey, the vertical velocity field at others depth than 90 dbar was coherence to the behavior described for the 90 dbar level. In western side (figure D.3a.ss2), the intensification of the downwelling corresponded to an increase in the steepness of the density field, as denoted by the 26  $\text{kg/m}^3$  and 28  $\text{kg/m}^3$  isopycnals. The vertical section at the 4.22°W (figure D.3b.ss2) showed as the vertical velocities within the eastern part of the sampled area remained in the range  $\pm 5$  m/day associated with the inner part of the WAG.

The significant increase in the curvature of the AJ and in the rim of the WAG during the third survey resulted in a vorticity distribution similar to the one found during the second survey but displaced southeastward.

The advection of vorticity did not increased, and accordingly the downwelling pattern at the eastern boundary reduced its magnitude to  $-68$  m/day, stretching eastward and breaking the evolving upwelling patch into a northern and southern parts, with maximum vertical velocities of 25 m/day (figure D.2 b.ss3). Due to the eastward displacement of the WAG, the circular part of the WAG was at the southeaster side of the sampled domain, and this area was therefore characterized by weak vertical velocities,  $\pm 5$  m/day. The trough found in the density field at the rim of the WAG (36.2°N, 4.1°W) produced vorticity advection and thus significant vertical velocities, developing an upwelling/downwelling cell with values up to  $\pm 25$  m/day. The vertical velocity field exhibited similar behavior throughout the whole water column. At 4.8°W, the upwelling/downwelling cell was divided by the doming of the isopycnals associated with the meander of the AJ, while the section at 4.2°W showed the weak vertical velocities found within the core of the WAG (figures D.3a.ss3 and D.3b.ss3).

The vertical motion field computed for the fourth survey revealed significant changes if compared with previous surveys. There are two reasons for that: firstly, the pushing of the AJ modified considerably the position and shape of the WAG; and secondly, the sampling done during the fourth survey was done with CTDs 20 km spaced, a much lower spatial resolution than that obtained in previous surveys.



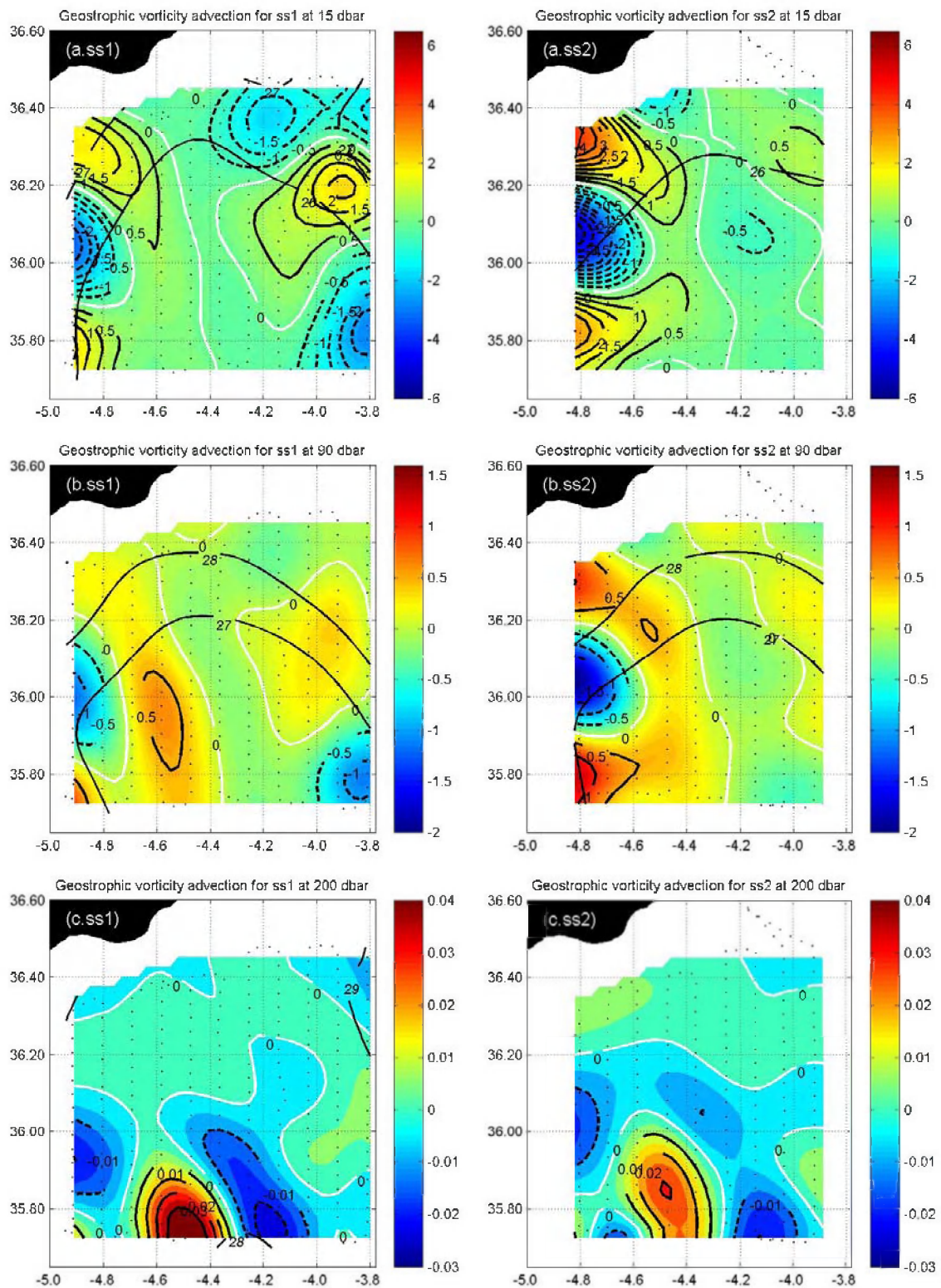


**Figure D.4:** Horizontal distributions of vorticity advection ( $\times 10^{-9}$ ) at (a) 15 dbar (b) 90 dbar and (c) 200 dbar for the (ss1) first, (ss2) second, (ss3) third survey and (ctd) fourth survey.

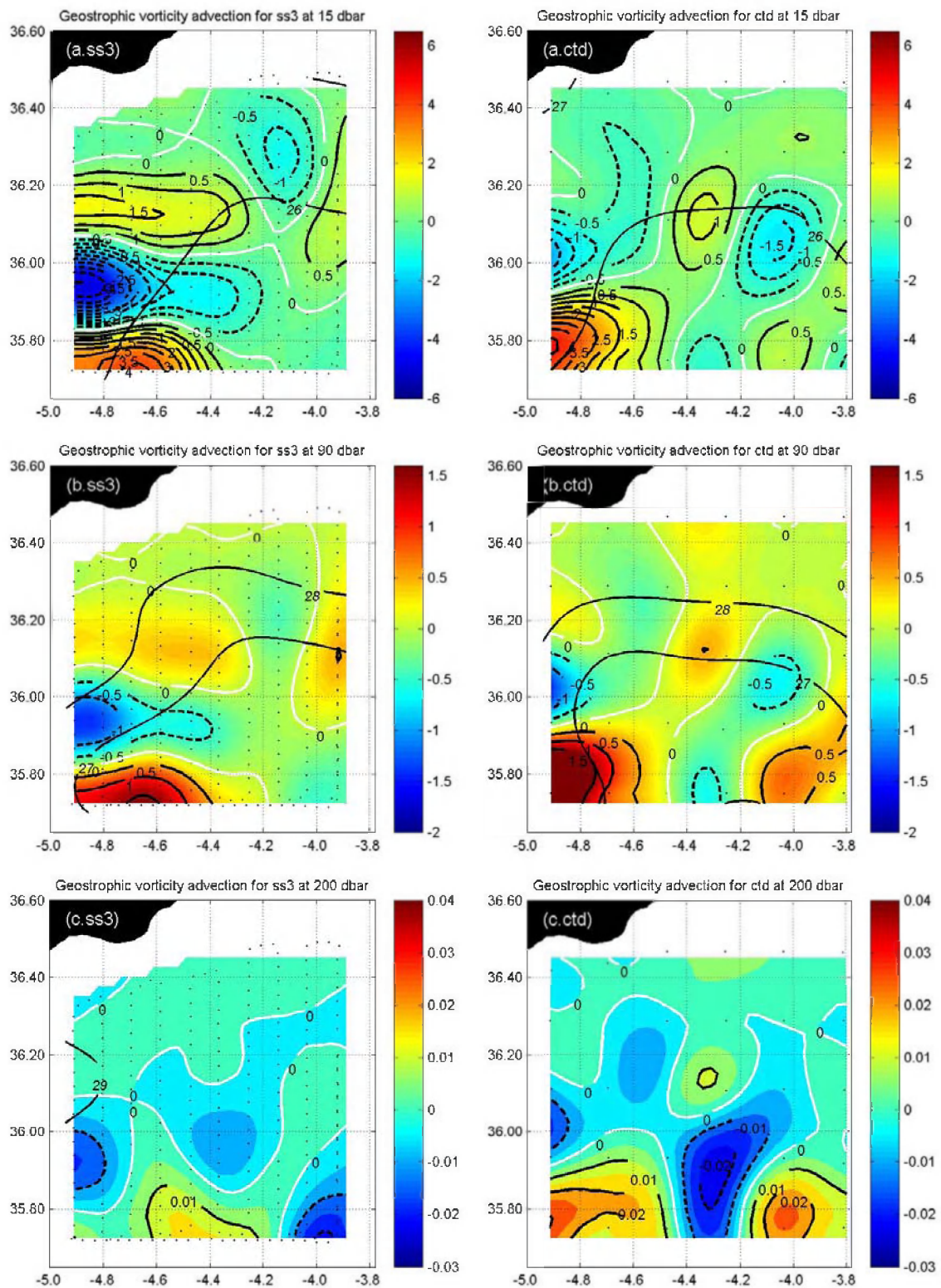
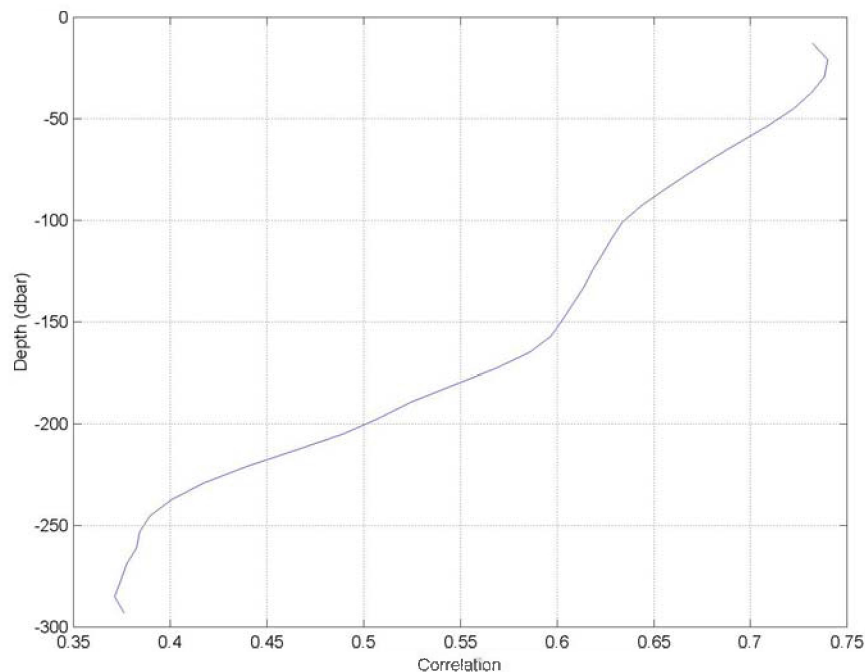


Figure D.4: (Continued).



Thus, gradients are smoother and the magnitudes of the geostrophic vorticity and vertical motion are weaker than in previous survey. Besides that, the vertical velocity field is displaced towards the southeast, since the WAG was moved towards the southeastern part of the sampled domain.

Following the rim of the WAG there were two cells of downwelling/upwelling, the first one was the result of the strong cyclonic/anticyclonic meander at  $36^{\circ}\text{N}$ ,  $4.8^{\circ}\text{W}$  and its associated geostrophic vorticity advection. The second cell, much weaker than the first one was consequence of the meanders in the rim of the WAG, although the geostrophic vorticity advection was weak and consequently the vertical velocities are small. As in the previous surveys, within the interior of the WAG the vertical velocities are weak, given that the vorticity and the vorticity advection were also low. The vertical section at  $4.8^{\circ}\text{W}$  crossed the two upwelling/downwelling cells, confirming the alternative positive and negative vertical velocities and the change in the steepness of the isopycnals.



**Figure D.5.** Vertical profile of correlation between the vertical velocity and the vorticity advection during the first survey.

At 4.22°W, the southern area had weak vertical velocities, since this area was occupied during the fourth survey by the inner part of the WAG (figures D.3a.ctd and D.3b.ctd).

It is interesting to note that during the first and second surveys, the maximum vorticity advection occurred at the western side of the domain, whereas during the third and fourth surveys those areas were in the interior of the domain. This fact has significant impact on the sensitivity of the  $w$  field to the non-resolved scales, and therefore in the accuracy of the computed field, of the diagnosed vertical velocities as has been described in chapter B.

### **D.3.2 Digital filtering initialization**

Alternative methods to the Q-vector omega equation for estimating vertical velocities exists. One of them consist in the combination of a primitive equation model with a with a low-pass filter. This technique, called digital filtering initialization was firstly developed for initialization numerical weather prediction models from observations [Lynch and Huang, 1992], and was firstly applied to the ocean by [Viúdez *et al.*, 1996a], who initialized an ocean PE equation model with the observed density field and integrated it shortly back and forward. The resulting vertical velocity and density field were obtained by applying a low pass filter to the resulting time series. The concept behind DFI is the possibility of removing the high frequency signal from the “slow manifold” of the primitive equation model [Lorenz, 1992] by applying a low pass filter. Since the DFI technique is based on an ocean PE model, the resulting fields will include dynamics of higher order than that included in the quasi-geostrophic approximation.

#### **D.3.2.1 Boundary conditions**

To integrate the PE ocean model, open boundary conditions are needed to simulate the open-ocean and dissipate the waves created during the adjustment processes dissipate. The open boundaries are especially important in the present case due to the small sampled domain. The strong dynamics that characterize the western Alborán Sea, with typical velocities at the surface of 100 cm/s and nearly 50 cm/s at

intermediate levels, 100 dbar, produce that waters particles could be advected from one side to the other of the domain in 1-2 days. Under such circumstances, optimal open boundary conditions are necessary to minimize reflection of waves and therefore to avoid artificial fields. The open boundary conditions used are based on the *Ross and Orlansky* [1982] and *Chumbinho* [1994] formulations, with slightly small changes, and can be summarized with the following steps:

- Firstly, at each point it should be decided if there is either inflow or outflow. For such a purpose, the velocity vector normal to the boundary plus a constant that guarantees propagation of waves out of the domain is used, this is  $\delta = C_a + \vec{V}_n$ ,

where  $\vec{V}_n$  is the velocity component normal to the boundary at the boundary:

$$\vec{V}_n = -1/4 \cdot [u_{2,j}^n + u_{2,j-1}^n + u_{1,j}^n + u_{1,j-1}^n],$$

the superscript n indicates the timestep.

- For the inflow points, the vorticity, divergence and density are set to the observed boundary values, while for the outflow points the vorticity, divergence and density are advected from the interior domain using an advection velocity normal to the boundary.
- Given the values of the divergence and vorticity at the boundaries, the normal and tangential components of the baroclinic velocity are computed using the definition of vertical vorticity and divergence.
- Outflow density is also advected along the boundary, using a tangential phase velocity computed as the spatial four-way average of the nearest two rows to the boundary, but excluding the points at the boundary.

The boundary conditions for vorticity and divergence in the outflow case were modified from the original, since those equations were designed to deal with gravity waves, without taking into account the inertial waves. After *Chumbinho* [1994], the following scheme for divergence and vorticity at the boundaries was set:



$$\begin{aligned}\frac{\partial D}{\partial t} + \delta \frac{\partial D}{\partial n} &= f\zeta - \gamma D \\ \frac{\partial \zeta}{\partial t} + \delta \frac{\partial \zeta}{\partial n} &= -fD - \gamma \zeta\end{aligned}$$

where  $f$  is the coriolis parameter and  $n$  is taken normal to the boundary.

$D$  is the divergence and  $\zeta$  is the vertical component of relative vorticity:

$$\begin{aligned}D &= \frac{\partial u}{\partial x} + \frac{\partial v}{\partial y} \\ \zeta &= \frac{\partial v}{\partial x} - \frac{\partial u}{\partial y}\end{aligned}$$

The damping coefficient was specified to be proportional to the effective gravity wave speed normalized by the grid size; the intention of this parameterization was to damp anomalies in a time scale of days.

$$\gamma = \frac{\delta}{\Delta x}$$

In finite differences form, the final vorticity and divergence equations are, respectively:

$$\begin{aligned}\zeta_B^{n+1} &= \zeta_B^n - \delta \frac{\Delta t}{\Delta x} [\zeta_{B+1}^n - \zeta_B^n] - f\Delta t D_B^{n+1} - \gamma \Delta t \zeta_B^n \\ D_B^{n+1} &= D_B^n - \delta \frac{\Delta t}{\Delta x} [D_{B+1}^n - D_B^n] + f\Delta t \zeta_B^{n+1} - \gamma \Delta t D_B^n\end{aligned}$$

where the subscripts  $B$  and  $B+1$  indicate the boundary point and the adjacent interior point. The previous equations are solved simultaneously at each time step along the four boundaries, except in the corners, where the vorticity and divergence are set equal to the average of the two adjacent points that have been already computed by advection normal to the boundaries. Initially, for inflow at the lateral boundaries, the vorticity was specified from its initial geostrophic value and the divergence was set to zero.

In order to test the sensitive of the vertical velocity field to changes in the different parameters of the open boundary conditions, a set of model simulations were done, in these simulations the total integration time was set to 12 hours, and the conclusions

are summarized as follows. Without the advection of density in the open boundary there were significant changes in the  $w$  field, with changes in the magnitude of  $w$  up to 10 m/day in 1/8 of the sampled area, especially at the northern, eastern and western boundaries, where the tangential velocity component was more intense. On the other hand, changes in the friction and coriolis terms of the open boundaries did not affect significantly the vertical velocities; with modifications in its magnitude smaller than 5 m/day, but only affecting 1/16 of the domain nearest to the boundaries. Additional tests of the model were done in order to find the set of parameters that was more stable and therefore give longer integration times; resulting that those simulations with the approaches that most affect the  $w$  field were the more stables. In summary, the best approach to the open boundary conditions for the case area is the one that computes the phase velocity based in the evolution of the density field, and includes advection of density along the boundary, coriolis and damping term.

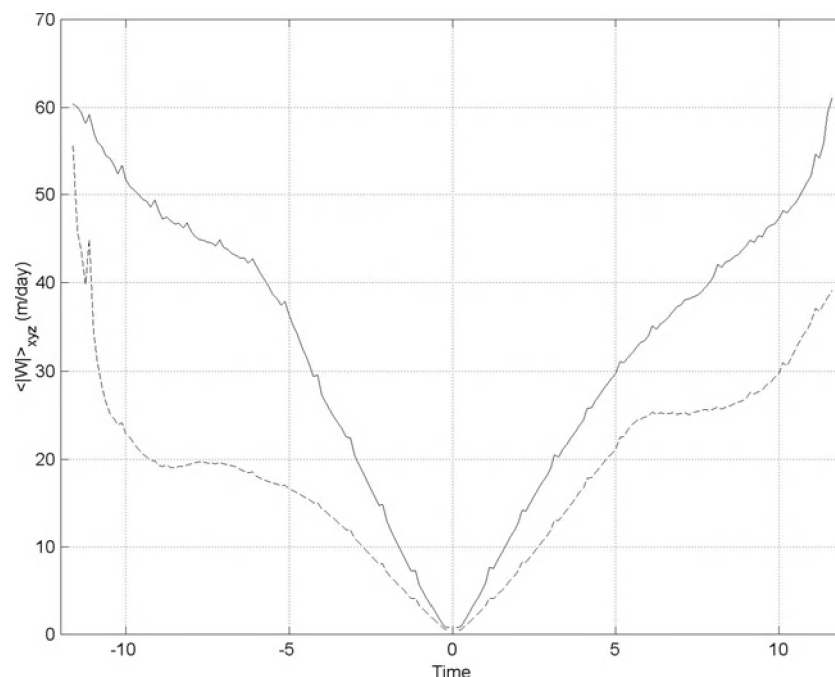


**Figure D.6.** Absolute vertical velocity (m/day), averaged over the domain, as function of the integration time (h), for the first (solid line) and the third (dashed line) surveys

### D.3.2.2 Spin up

The PE model was initialized with the density fields obtained after the objective analysis described in chapter C.-*Analysis methods*, while the initial currents were the geostrophic velocities associated with the density field, and using the level of no-motion described in chapter B. The geostrophic velocities were been used since the ADCP velocities contain noise at scales smaller than the Rossby radius and were significantly aliased by inertial motions and internal baroclinic tides.

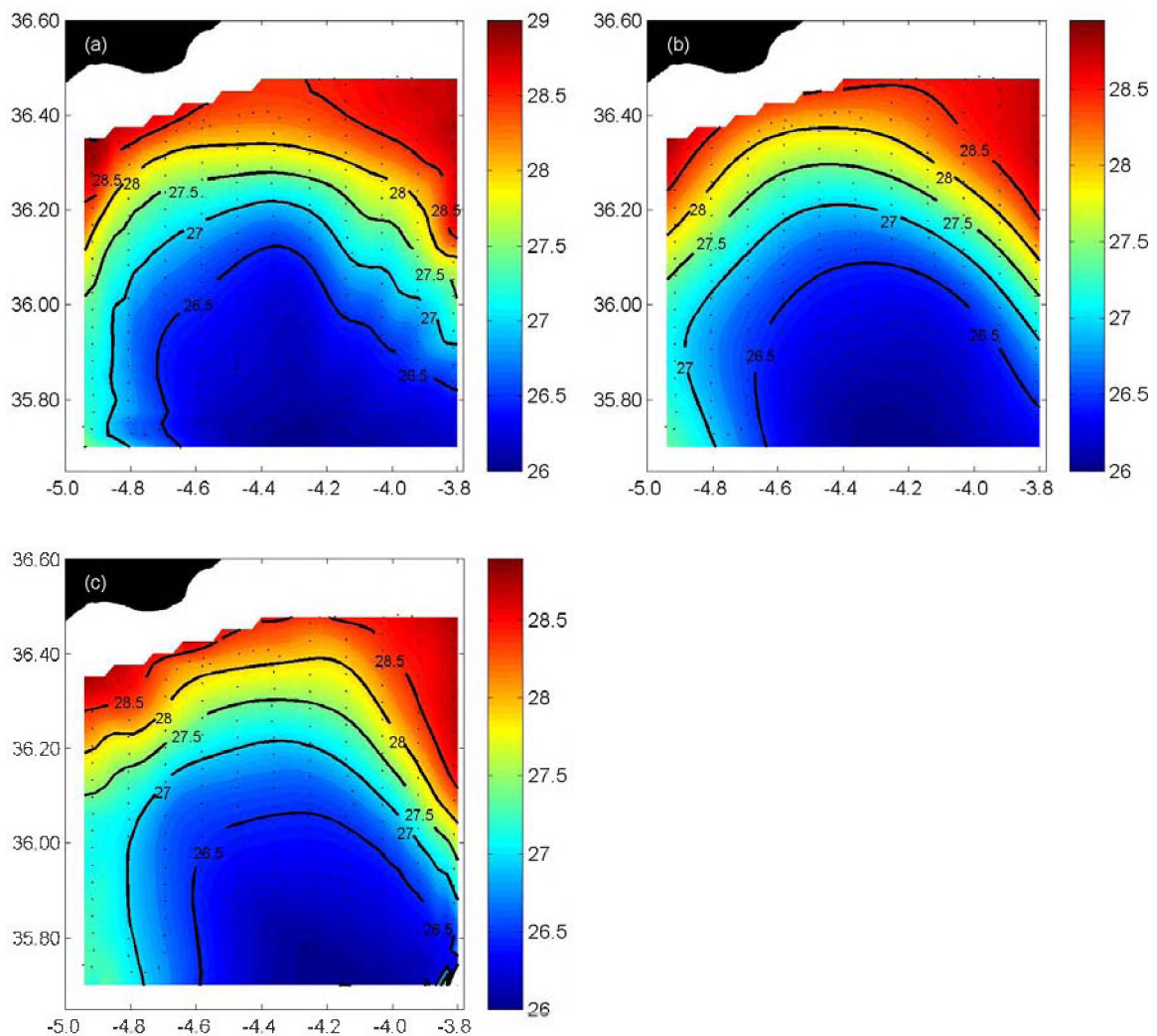


**Figure D.7.** Density fields ( $\text{kg/m}^3$ ) at 100 dbar from the primitive equation model at (a)  $t=-12\text{h}$ , (b)  $t=0\text{h}$  and (c)  $t=+12\text{h}$ . The small dots indicate the survey track.

The total forward and backward integration time was set to 24h with just one filtering cycle. The use of a time span of 24h permitted to average over the inertial period of the

Alborán Sea, nearly 20h. Different integration times and cycles were tested and compared, yield differences smaller than those due to changes in the open boundary approach.

The average absolute vertical velocity at each time step for the whole volume illustrates the spin-up process of the PE model (figure D.6). The vertical velocity increased during the first 6 hours of integration, pointing out the adjustment after the initial geostrophic balance. Since any advection produced by the geostrophic flow will try to destroy the initial thermal wind balance, an ageostrophic motion was developed to keep the evolution in thermal wind balance. The adjustment is achieved through waves radiated outside the domain, as shown in fig D.7. Associated with these small scale features there were strong vertical velocities that were removed as high frequency signal by the low-pass filter applied to the time series.

### **D.3.2.3 Results**

The PE/DFI technique was used successfully with the four surveys; however only the results obtained for the first and third surveys will be described given that these two surveys are a good representation of the different dynamical situations found. During the first survey, the maximum advection of vorticity was localized near the eastern and western boundaries, while during the third survey this maximum was well within the sampled domain. Through the assimilation processes, the density field suffered small changes, although the rms difference between the initial and filtered density field was  $0.12 \text{ kg/m}^3$  for the first survey and  $0.13 \text{ kg/m}^3$  for the third survey. The  $w_{\text{dfi}}$  domain is smaller than the  $w_{\text{qg}}$  domain, since the grid point near the boundaries has been taken out from the  $w_{\text{dfi}}$  as consequence distortion produced by imperfect open boundary conditions of the model.

The vertical velocity field (figure D.8) computed with PE/DFI have similar pattern than that calculated via the omega equation. The rms difference between the QG and DFI  $w$  fields was  $7.18 \text{ m/day}$  for the first survey and  $6.90 \text{ m/day}$  for the third survey. The

apparent little difference between both  $w$  fields is quantitatively corroborated: the sign of  $w_{DFI}$  match the sign of  $w_{QG}$  at 84% of the grid points for the first survey and 87% for the third one. The results are in agreement with those obtained previously by [Viúdez *et al.*, 1996a] and [Chumbinho, 1994] in the California current.

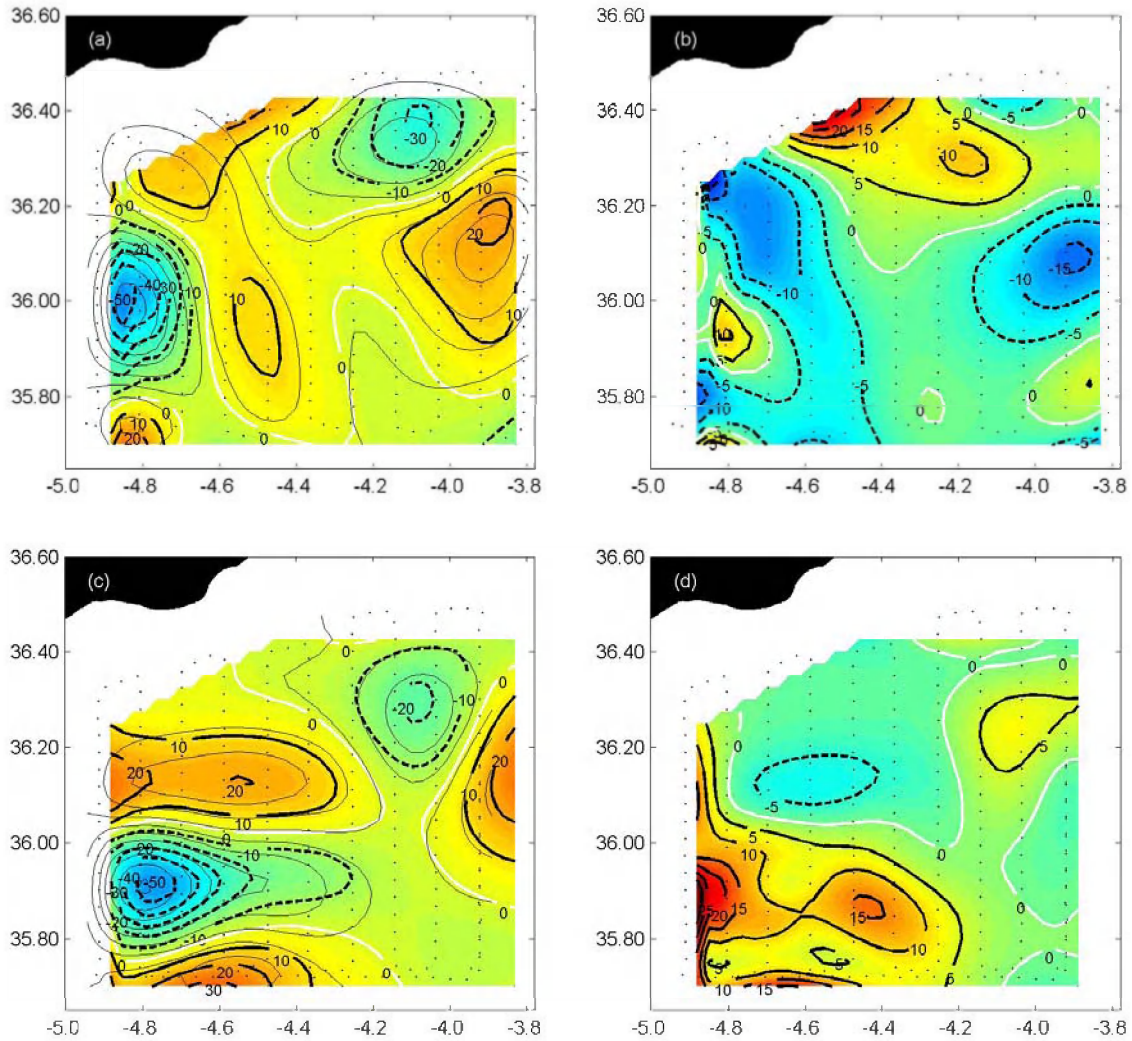


**Figure D.8.** Vertical velocity field at 90 dbar computed using the PE/DFI technique for the (a) first survey and the (c) second survey. Contour interval is 5 m/day with thick contours each 10 m/day. The thin line is the vertical velocity field computed using the QG-omega equation. The difference between the  $w_{DFI} - w_{QG}$  at 90 dbar for the (b) first survey and the (d) second survey are included.

These authors found that the quasi-geostrophic vertical velocities were 30% larger than those calculated using the omega equation. As expected the  $w_{QG}$  field was higher than the  $w_{DFI}$  because of lack of ageostrophic advection in the QG approach. The DFI



technique does not have this overestimation since DFI take into account the advection associated with the ageostrophic horizontal velocities. For those grid points where  $|w_{QG}| > |w_{DFI}|$ ,  $w_{DFI}$  is 64% of the  $w_{QG}$  for the first survey and 60% for the third survey in average. The QG overestimation is similar for upwelling and downwelling, representing a 67% and 63% during the first survey and 61% and 63% for the third survey. Similar differences were obtained for the other surveys, indicating that the variation in the dynamical situation do not affect the estimations obtained by the DFI/PE method. The differences with respect the QG estimations are similar if different objective analyses parameters are used, thus demonstrating that the theoretical approach have lower impact on the uncertainty of the vertical motion than the uncertainty due to the sampling and observational errors.

#### D.4 THREE-DIMENSIONAL CIRCULATION

The vertical motion for the four surveys show strong velocities associated with meanders in the rim of the WAG and in the AJ; however, the high horizontal velocities in the area indicate that a water parcel would not feel for a long time the strong vertical velocities. In order to understand the behavior of a water parcel traveling through the domain, simulations of trajectories have been computed using the geostrophic velocities and  $w$ , interpolated to the position of the water parcel, and integrating forward in time, with a time step of 0.1 hours. This is coherence with the quasi-geostrophic approximation, where the vertical displacements are assumed to be much smaller than the horizontal ones. Since the system is not stationary, these simulations will correspond neither to the true trajectories nor to the streamlines of the flow. The vertical velocity field used is the determined with the omega equation because this  $w$  field does not have spurious values at the boundaries.

In the first set of simulations, the initial position was at the rim of the WAG, at 90m dbar in the westernmost leg (4.9°W, 35.90°N). In the simulations for the first and the third survey, the horizontal path of the trajectories is very similar to the streamlines, as

expected under the QG approximation (figures D.9a, b). Alternative out of phase maximums and minimums of  $\zeta_g/f$  and  $w$  is an indication of the conservation of potential vorticity. After a maximum (minimum) of  $\zeta_g/f$ , the water parcel is advected into a region of rapid vorticity changes, to conserve potential vorticity the water parcel have to shrink (stretch) and consequently involving upwelling (downwelling) (figure D.9b). For the simulation done with the dynamical conditions found during the first survey, the water parcel was firstly deployed in a downwelling area, initially deepening 25 m in less than one day (figure D.9c). Right after, the water parcel entered in the interior region, dominated by weak positive vertical velocities, to finalize its trajectory throughout the upwelling structure at the eastern side of the domain, resulting in a net displacement over the three and half days of trajectory smaller than one meter. The water parcel simulated in the third survey also spent three days to cross the sampled domain, revealing potential vorticity conservation by the alternative maximum/minimum of  $\zeta_g/f$ , followed by maximum/minimum of  $w$  (figure D.9e). After deployment, this water parcel traveled through the strong downwelling at the western side of the domain, deepening 15 m in half a day; during the following 1.5 days, it crossed the upwelling patch, associated with the meander in the rim of the WAG, at the northwest side of the area; to end its trajectory crossing the downwelling/upwelling cell at the northeast. The net vertical displacement is small, less than 3 m. Four more trajectories with different initial depth and position have been simulated for the first and third survey (figure D.10). During the first survey, the trajectories of water parcels deployed at the same geographical location, but at different depth, had very similar trajectories, with only differences in the time spent in the area (figure D.10a). Since the AJ is surface intensified, the deeper water parcel moves more slowly through the region than the shallower ones, taking almost 24 days to cross the sampled domain. The net vertical displacement is smaller than 2 m, except for those water parcels deployed at the outermost limit of the WAG and outside the WAG, which had a net vertical displacement of about 4 m (figure D.10c).

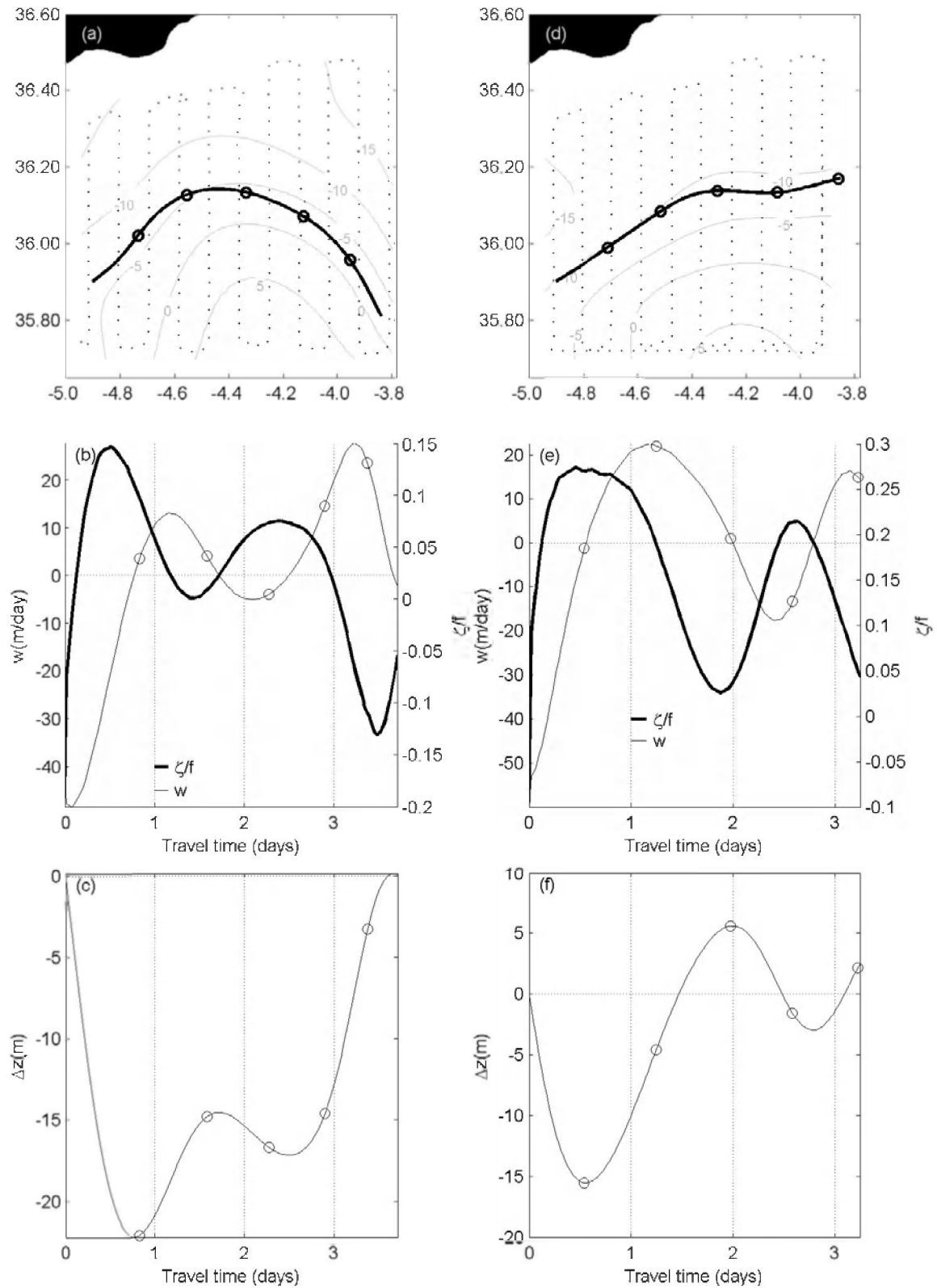


**Figure D.9.** Simulated trajectories for a water parcels initially at 90 dbar for surveys (a) ss1 and (d) ss3. For reference, the dynamic height at 90 dbar is overlaid. Time series of  $w$  and  $\zeta_g/f$  along the trajectory for surveys (b) ss1 and (e) ss3. Net vertical displacement for the water parcels for surveys (c) ss1 and (f) ss3. The dots are drawn every 20 km.

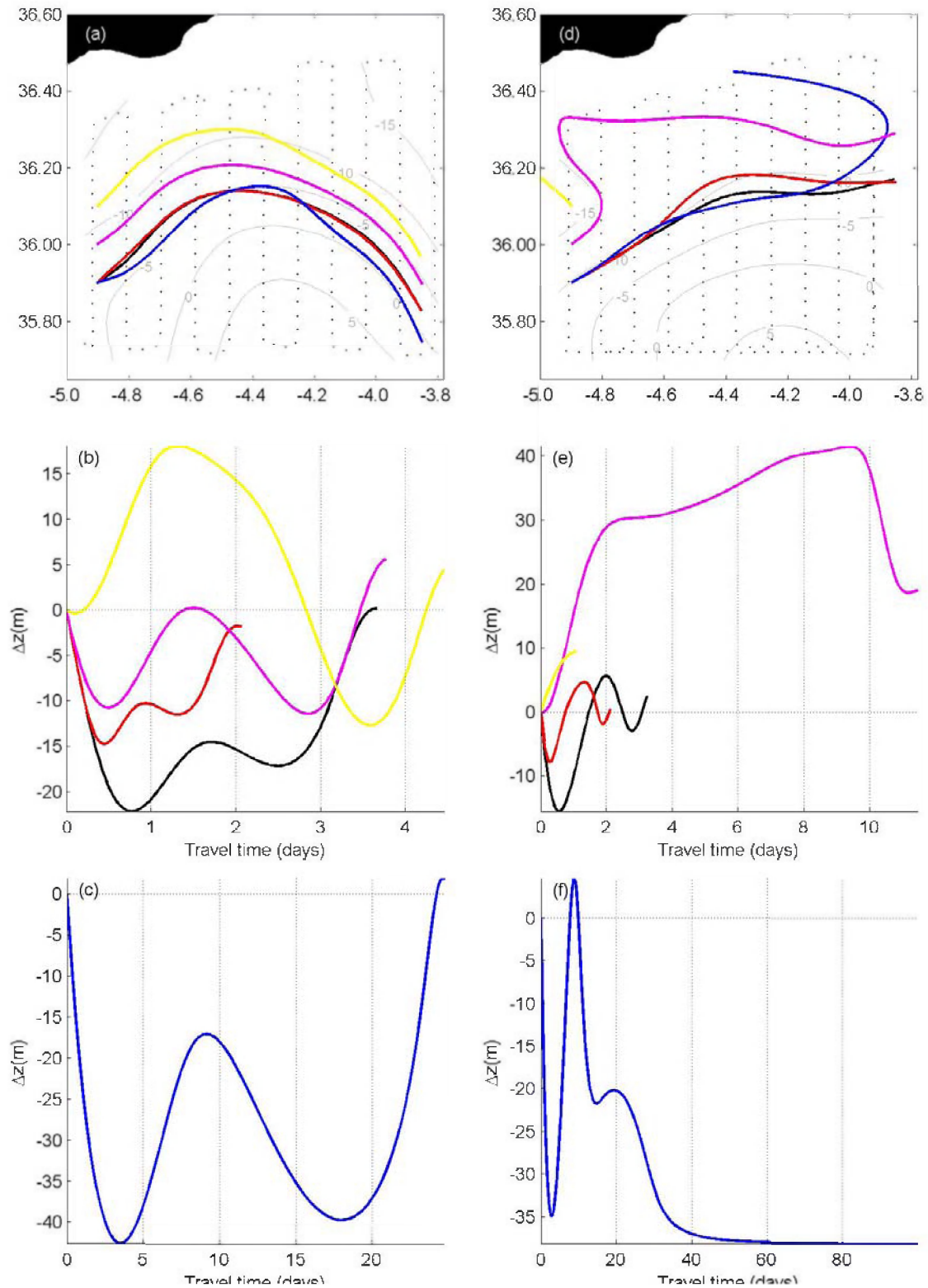


**Figure D.10.** Simulated trajectories for water parcels initially at 50 dbar (red), 150 dbar (blue) and 100 dbar (black, yellow, and magenta) for surveys (a) ss1 and (d) ss3. Net vertical displacement for water parcels initially at 100 dbar for surveys (b) ss1 and (e) ss3. Net vertical displacement for water parcels initially at 150 dbar for surveys (b) ss1 and (e) ss3.

During the third survey, the WAG was more southward than in the previous surveys and therefore the water parcel deployed northern than  $36^{\circ}\text{N}$  got in the slow Mediterranean waters north of the WAG (figure D.10b), spending more than 10 days in the domain. During most of the time the water parcel was at the upwelling area of the northwest side and hence experimented high, up to 20 m, net vertical displacement (figure D.10f). The water parcel released at the northernmost part was not in the AJ and was trapped in the cyclonic circulation at the northwest, being expelled from the domain in less than two days. As result of the southward displacement of the WAG and the southeast tilting of the centre of the high pressure associated with the WAG, the water parcel released at 150 dbar was trapped in the slow Mediterranean waters north of the WAG's core, spending there more than 60 days and resulting in a net vertical displacement of about -38 m, since it spent a long period in the downwelling patch of the northeast. The net vertical displacements for the other trajectories were small, similar to those found for the first survey and around 2 m.

The trajectories already described show that the predominant horizontal length-scale found in the area corresponds to the meanders of the western Alborán gyre and the Atlantic Jet, between 30 km and 40 km, of the order of the Rossby radius of deformation. The results obtained from the simulations carried out with the first and the third surveys reinforce the ideas exposed before, this is, since the WAG is at its mature state, nether net downwelling nor net upwelling has been observed, only those trajectories outside the WAG showed appreciable net vertical motion, given that the dynamics was not the same as the one associated with the WAG.

## **D.5 DISCUSSION AND CONCLUSIONS**

The unprecedented resolution and synopticity of the surveys carried during October 1996 in the northwestern Alborán Sea has provided a unique opportunity to test the validity of the quasi-geostrophic omega equation, as a method to diagnose vertical velocities. The density field showed a density front associated with both, the northern



part of the WAG and the AJ, with gradients up to  $2 \text{ kg/m}^3$  in one Rossby radius. The AJ reached maximum speeds above  $110 \text{ cm/s}$ . The area was characterized by a region of negative vorticity associated with the WAG, with values up to  $-0.6f$  at  $90 \text{ dbar}$ . The rest of the sampled domain had patches of positive and negative vorticity associated with the meandering and shear at the WAG's rim and at the AJ; the positive vorticity reached values up to  $0.5f$  at  $90 \text{ dbar}$ . This frontal situation had associated a strong non-geostrophic circulation, the resulting  $w$  field was consequence of an ocean tending to be in near geostrophic and hydrostatic balance, and therefore the slope of the isopycnal slope by itself cannot suggest the  $w$  distribution.

The vertical motion in this complicated balance has been obtained using two different techniques: the inversion of the quasi-geostrophic Q-vector form of the omega equation; and the assimilation of the density field into a PE ocean model, where the fields resulting from the forward and backward integration have been filtered to extract the slow mode from the high frequency signal.

In the energetic western Alborán Sea, the omega equation yielded vertical velocities between  $-100 \text{ m/day}$  and  $+70 \text{ m/day}$ . The maximum values were at the rim of the WAG and at depth of  $90 \text{ dbar}$ , where the maximum vertical density gradients occurred; being the differential geostrophic advection of geostrophic vorticity the main contribution to  $w$ . The model assimilation technique gave vertical velocities slightly smaller, with  $\text{rms}(w_{\text{DFI}} - w_{\text{QG}}) = 7 \text{ m/day}$ , since the omega equation tends to overestimate the vertical velocity due to the lack of ageostrophic advection in the QG theory. If the parameters in the objective analysis of the density field are modified, the differences between the vertical velocities from the omega equation and those from the PE/DFI assimilation kept small, meaning that the impact of the theoretical approach is low, and much smaller than the sampling and observational errors. The horizontal lengths scales are dominated by the meandering of the WAG's rim and therefore are around the local internal Rossby radius of deformation,  $30\text{-}40 \text{ km}$ . The time evolution of the  $w$  field between the first and the four surveys is easily tracked if the pushing of the WAG by

the AJ, and the meandering of the WAG's rims are considered. However, it has not been any attempt to determine the quasi-geostrophic time evolution because, as described in chapter B, the time evolution during the first fortnight of October 1996 was dominated by the changes in the inflow through the strait of Gibraltar rather than by the slow QG evolution.

The analysis of the simulated water parcel's trajectories for the first and third surveys, representatives of the two different dynamical situations found, indicates that the net vertical displacement for those waters parcel released in the interior of the WAG was very small, less than 5 m/day. The WAG was in its mature stage and neither net downwelling nor net upwelling were observed, only those trajectories outside the WAG showed appreciable net descending or ascending, since the dynamics was not the same as associated with the WAG and the horizontal velocities were smaller [Vélez-Belchí *et al.*, 1999].

The small net vertical motions found are coherent with the quasi-geostrophic theory, which assumes that the vertical displacements are much smaller than the horizontal ones. Values of geostrophic vorticity along the simulated trajectories indicated that the vertical velocities were consequence of potential vorticity conservation.

In addition to the uncertainty due to the theoretical approach and observational errors, the diagnostics presented here are just a snapshot of the real ocean, and the time-varying structures can significantly modify the upwelling and downwelling areas, as will be described in the next chapter. For that reason, quantification of the transport of any quantity should be done with a precise knowledge of the four (space and time) dimensional velocity field.

---

## **E.-LAGRANGIAN VERTICAL VELOCITY DATA**

---

## E.0 ABSTRACT

The order of magnitude of the vertical motion found in energetic areas as the western Alborán is smaller than the accuracy of most of the techniques and instruments used to measure currents in eulerian frameworks. For instance, the ADCP accuracy is around 1 cm/s, while a typical value for vertical velocities is 15 m/day, approximately 0.018 cm/s. Thereby, and in spite of the importance of vertical velocities in marine ecosystem and ocean dynamics, indirect methods should be used to obtain vertical velocities from routine hydrographic surveys. Occasionally, lagrangian measurements of vertical velocity are available with floats that register vertical excursion of isopycnals and the vertical motion of water parcels across the isopycnals. In this chapter, vertical motion measured by six floats in the western Alborán Sea is presented and compared with vertical velocities estimated with the Q-vector form of the omega equation. The spatial and temporal scales that characterize the measured vertical velocity are similar to those that characterize the estimated fields, although the range of the measured vertical velocities is slightly smaller than those computed with the QG-omega equation, as should be, given the restrictions that the quasi-geostrophic theory impose on the ageostrophic advection. The results presented in this chapter, permit to establish that, the sign, order of magnitude and size of the patches of upwelling and downwelling determined with the Q-vector form of the omega equation, from routinely measured density fields, are trustable.

## E.1 INTRODUCTION

Given the already described importance of the vertical velocities and the impossibility to measure them, there is a need to validate the diagnosis techniques with in situ-data. The first attempt to compare computed vertical velocities with in-situ lagrangian estimates was carried out by *Lindstrom and Watts* [1994]. They compared three different independent vertical velocities estimates: time derivatives of pressure from RAFOS floats on isopycnal surfaces; the heat equation applied to the temperature and velocity data from moored currentmetres  $w_{CM}$ ; and the quasi-geostrophic vorticity equation applied to a geostrophic stream function determined from inverted echo sounders,  $w_{IES}$ . High agreement between  $w_{IES}$  and  $w_{cm}$  was found, as well as a significant linear correlation between selected samples of float vertical velocities (around twenty from a two-year period) and the two other estimations. The spatial and temporal scales of upwelling and downwelling motions for the three methods were similar.

However, in that study the dataset was collected within an intensive multi-institutional study with more than 24 inverted echo sounders and 12 moorings for two years that provided an exhaustive time and space coverage for the  $w_{cm}$  and  $w_{IES}$  estimates. Nevertheless, usually CTD/SeaSoar surveys do not have such intensive coverage and thus the results from *Lindstrom and Watts* [1994] should be revised for surveys like those studied here. More over, the study carried out by these authors did not analyses the validity of the omega equation since the dataset comprehend time evolving fields and the diagnosis was carried out with the quasi-geostrophic equation of heat and vorticity.



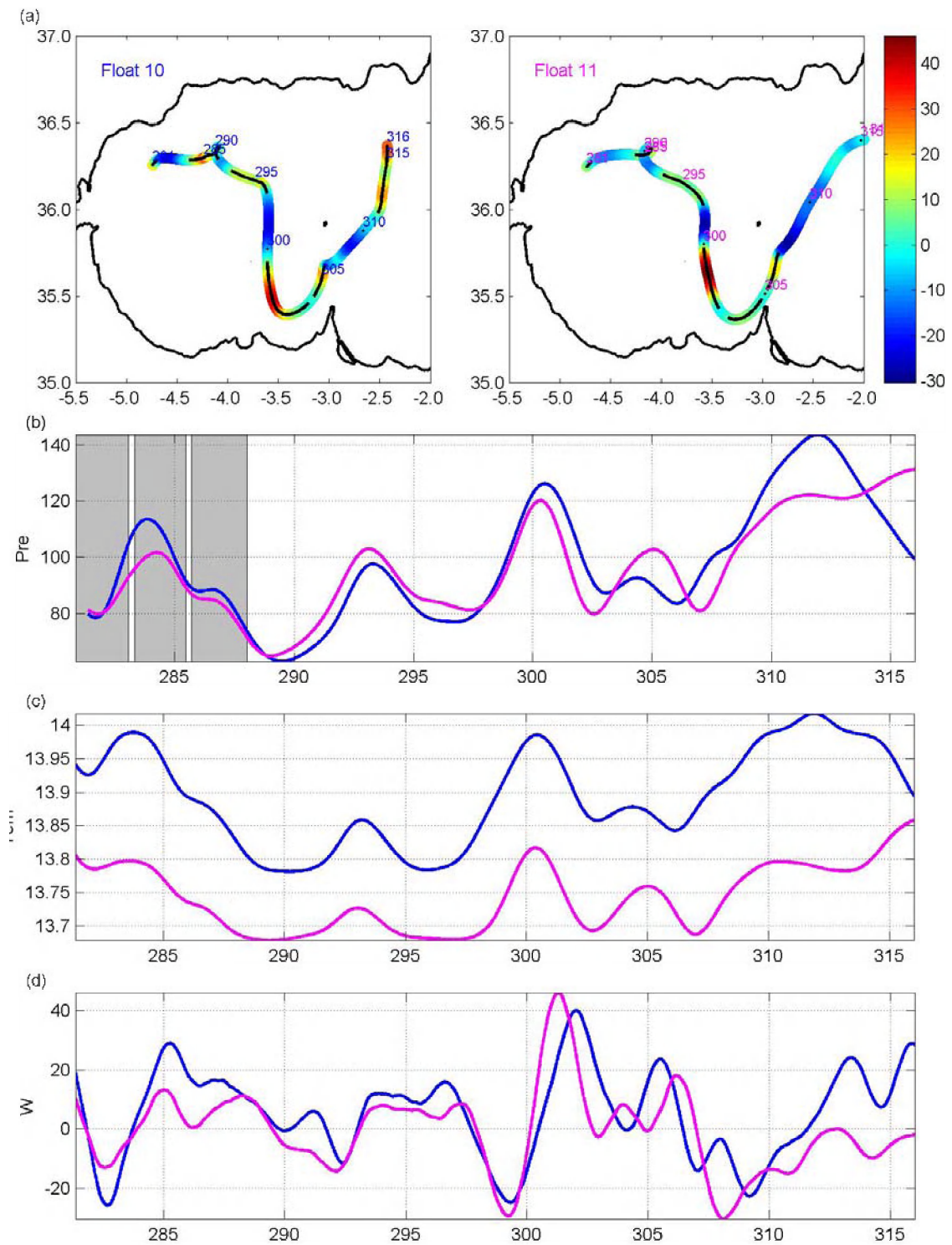


**Figure E.1.** (a) Trajectories of the cluster formed by floats 10 and 11, the labels in the trajectories are shown every five days, beginning on October 7<sup>th</sup> (yearday 282 in 1996). Float's pressure (dbar), (c) temperature (°C) and (d) measured vertical velocity (m/day) as function of yearday in 1996.

To validate the vertical velocity fields diagnosed with the QG and DFI/PE techniques in routine CTD/SeaSoar surveys, ten neutrally buoyant lagrangian floats were deployed (see section 0), to provide Lagrangian estimates of vertical velocity, temperature and pressure every 30 minutes. These floats registered vertical excursion of isopycnals and any vertical motion of water parcels across isopycnals.

The measured lagrangian vertical velocity  $w$  is constituted by two components. The entrainment component,  $w_E$ , is computed from the variations in the measured pressure since the buoyancy forces acting on the float displaced it vertically. In order to register the water passing through the float in situations where the compressibility of the float, half of that for the seawater, did not permit pure lagrangian behavior the floats had a vane that converted the associated drag forces onto rotations of the float. Variations in the number of turns,  $w_{ROT}$ , constitute the second component of the estimated lagrangian vertical velocity. It is the first time, as far as we know, that this kind of floats has been used in a stratified environment to estimate vertical velocities at mesoscale. In the following section, the data obtained with these floats is described and compared with the vertical velocities determined with the **Q**-vector form of the quasi-geostrophic omega equation.

## **E.2 RESULTS**

### **E.2.1 General description**

The floats were not deployed together, but right after the deployment they grouped in clusters of two floats. The two floats in each cluster had an almost identical behavior during the first 15 days (figures E.1 and E.2), except the cluster formed by floats 88 and 97 (figure E3). Following the deployment, all floats were trapped in a small cyclonic eddy eastward than the sampled domain, though each cluster left that eddy at a different time, giving snapshots views of the western Alborán sea during the second, third and fourth survey.

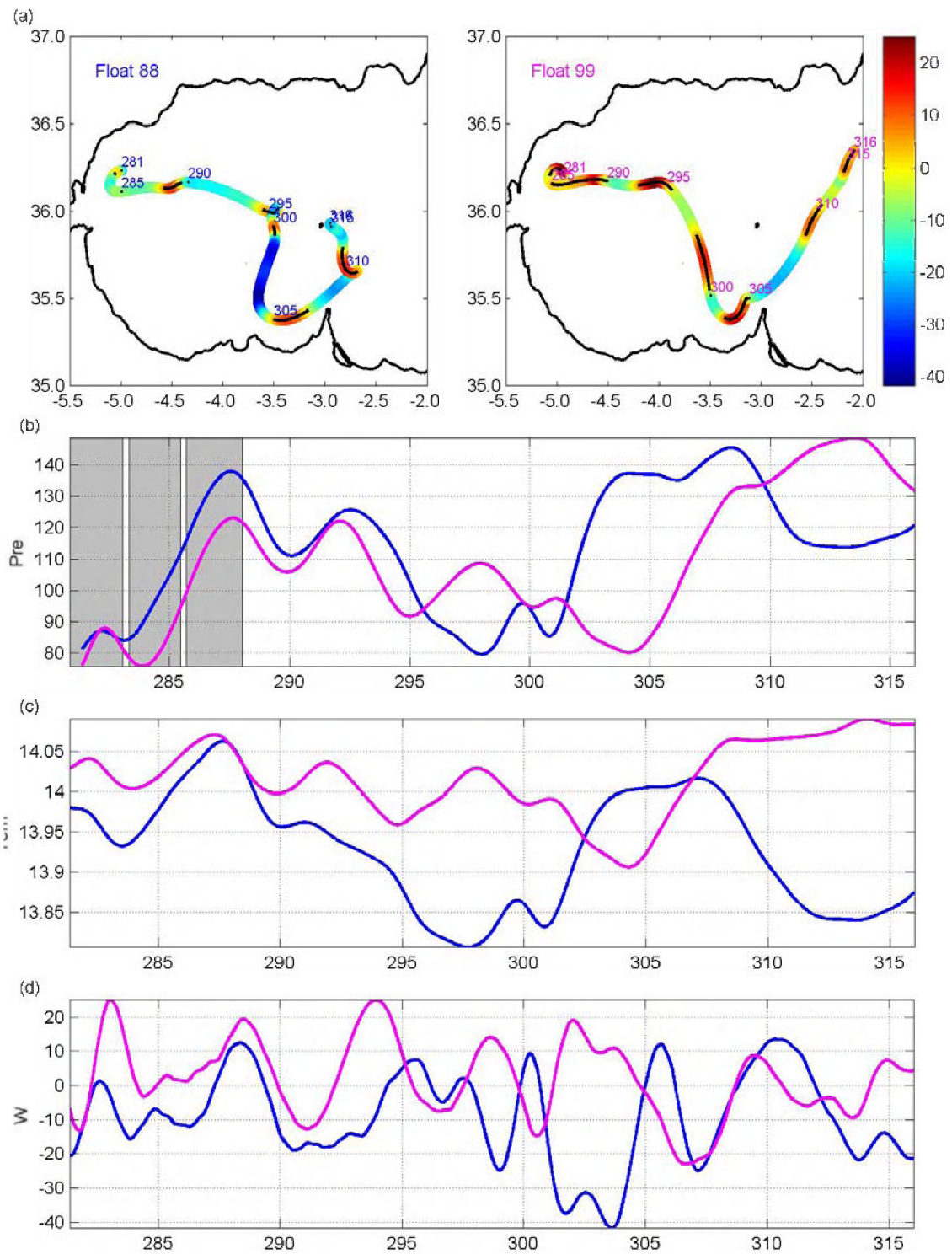


**Figure E.2.** Same as figure E.1 but for the cluster formed by floats 88 and 99.



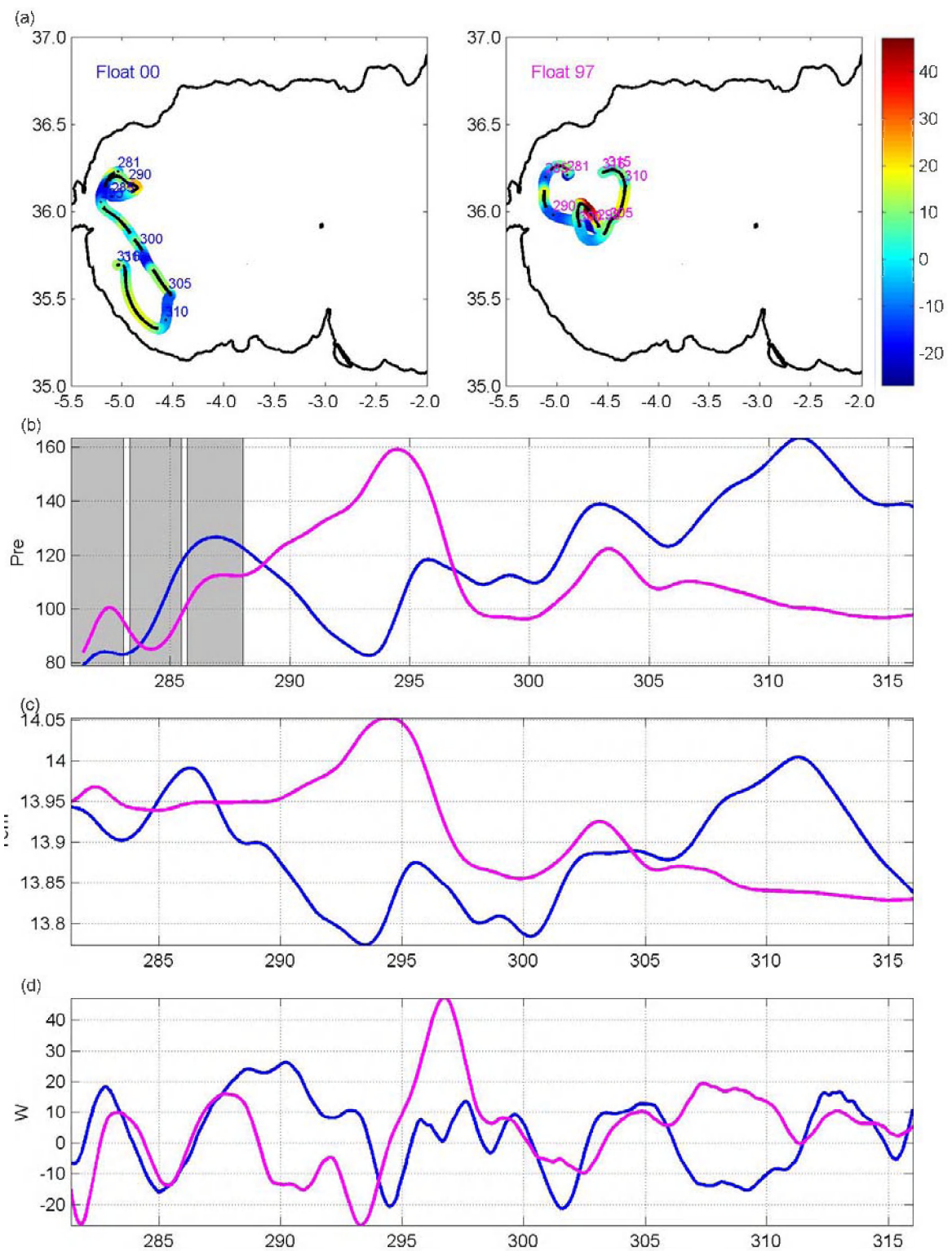


**Figure E.3.** Same as figure E.1 but for the cluster formed by floats 97 and 00.

The data recorded while the floats were at the cyclonic eddy cannot be used to compare with the diagnosed data, because the length scale of the eddy is poorly solved by the hydrographic sampling.

Float	Scale (km)	Min $w$ (m/day)	Max $w$ (m/day)	Std $w$ (m/day)	Pressure range (dbar)
10	25.83	-25.80 (-25.80)	39.98 (28.91)	14.66 (12.78)	80.72 (50.56)
11	25.59	-30.40 (-14.24)	46.08 (13.20)	13.64 (8.15)	66.53 (38.19)
88	24.91	-41.65 (-19.08)	13.50 (12.47)	13.27 (10.85)	65.81 (26.75)
99	30.06	-22.99 (-12.78)	25.10 (25.10)	11.21 (11.41)	72.69 (31.36)
00	19.62	-21.32 (-21.32)	26.37 (16.32)	12.16 (11.02)	84.37 (53.49)
97	21.21	-26.78 (-26.78)	47.16 (47.16)	13.94 (13.77)	74.97 (62.71)

**Table E.I.** Statistics of the vertical velocity measured by the floats, the value between parentheses was calculated with the data measured while the floats were in the area covered by the hydrographic data.

The first cluster to get into the sampled area was the one formed by floats 10 and 11, covering the second, third and fourth surveys (see figure E.1 and table E.I). This cluster crossed the sampled area in fourteen days, from yeardays 281 to 295, although five days were spent in the cyclonic eddy at 36.35°N, 4.1°W (figure E.1.a). For this cluster, the net vertical displacement during the period was small, with a range of vertical excursions in the study area up to 50 dbar for float 10 and 40 dbar for float 11. Such vertical displacements in a stratified area as the Alborán Sea would mean a change in temperature of more than 2°C, conversely, the recorded temperature signal (figure E.1.c) shows minor variations with a measured range of 0.25°C for float 10, indicating an almost complete lagrangian behavior. With that behavior, the  $w_{ROT}$  component of the vertical velocity was smaller than  $w_E$ , and the ratio  $w_{ROT}/w_E$  was in agreement with the theoretical considerations about the float behavior. The high correlation between the temperature and the pressure, with pressure increments corresponding to temperature



increments, indicated that departure from a pure lagrangian behavior was due to the impossibility of the floats to entirely follow the vertical water displacements.

Since the compressibility of the float is half of the seawater, during upward motions, the float will stretch less than the seawater and therefore would stay deeper than the tagged water parcel, registering a decrease in the float's temperature. A similar argument explains the increase of float's temperature for downward motions.

The cluster formed by floats 88 and 99 (figure E.2 and table E.I) drifted into the study area after two loops in the cyclonic eddy that trapped the floats after the deployment. This cluster was only in the study area during the third and fourth survey. The temperature and pressure records revealed similar behavior to that observed on the first cluster, with a range of vertical excursions up to 30 dbar but with small net vertical displacements in the study area. The correlation between the temperature and the pressure was the same as the one found for the first cluster, and then with an identical explanation.

The last cluster, formed by floats 97 and 00 (figure E.3 and table E.I), turned three times in the already mentioned cyclonic eddy, therefore entering in the study area after the fourth survey was finished. At this time the WAG was not in the western Alborán Sea, for that reason the dynamical situation sampled by this cluster is different that the one found by the other two clusters, and thus direct comparison with the vertical velocities computed from the hydrographic cannot be done. The records of temperature and pressure show a behavior similar to that described for the two others clusters, with vertical excursion up to 62 dbar in the study area, and with small variations in the measured temperatures, a proxy for the lagrangian behavior of these floats.

The vertical velocities measured by the floats ranged between 47.16 m/day and -41.65 m/day, and from 47.16 m/day to -26.78 m/day within the area covered by the hydrographic sampling, the study area (table E.I). The measured vertical velocities were smaller than the diagnosed via the QG omega equation. This overestimation may be partially explained by the already known overestimation of  $w$  by the omega

equation, given that the non-geostrophic advection is not included in the QG theory (see section D.8); and by the fact that the floats were released on the core of the AJ, drifting outside the areas of strongest vertical velocity.

To follow with the overall comparison between both estimations of the vertical velocity, a characteristic scale for the downward/upward patches has been calculated using the distance between the zeros in the measured  $w$ . For floats 10/11 and 88/99 this characteristic scale is similar (table E.I), given confidence to the data, with a mean value of 26.60 km, comparable to the length scale of the patches found in the vertical velocity fields diagnosed with the QG-omega equation. Floats 00/97 had a smaller characteristic length scale for the vertical velocity patches, with a mean value of 20.41 km. These different in the characteristic length scale can be attributed to the dynamical situation found by floats 00/97, since they entered in the sampling area after the WAG had disappeared and therefore  $w$  was measured in a context dynamically different than the one sampled by the other floats. The spatial and temporal length scales for the trajectories of the floats is similar to those simulated streamlines described in section D.5. Moreover, the ranges of the vertical excursions and of the vertical velocities are similar. The time-scale for changes in the lagrangian estimations of  $w$  is around 2/3 days, similar to the values inferred from the geostrophic simulations of streamlines presented in section 0. The time spent in the study area was longer for the real floats, given that they drifted over all the small-scale variability, spatially and temporally, not sampled in the surveys.

Figures E.1, E.2 and E.3 show strong correlation between the areas of change in curvature in the float's trajectories and the maximum measured vertical velocity, this is a clear indication of potential vorticity conservation. As water columns above the main thermocline move into an environment of increasingly anticyclonic vorticity (by moving toward a crest), the columns acquire anticyclonic spin; that is, the vorticity decrease, and to keep potential vorticity constant, the water column must shrink, which is accomplished by upwelling and the ascent of water within the main thermocline. If it

were possible to split the streamlines of the flow from the time-evolution of the Western Alborán Sea, the correlation between the changes in curvature and  $w$  would be stronger.

### **E.2.2 Comparison between the measured and diagnosed vertical velocity.**

To compare the vertical velocities measured by the floats with those diagnosed using the Q-vector form of the quasi-geostrophic omega equation, a set of simulations, where the floats' trajectories have been used as a path to sample the computed velocity fields, have been carried out. Only those vertical velocities determined with hydrographic data measured within one day of the float's data have been used (figure E.4); although a time-period of three days has been included as a dashed line in the figures for comparison. Due to the high agreement between the diagnosed QG and the DFI vertical velocity fields, the simulations have been done just using the QG diagnosis.

Right after the deployment, the six recovered floats grouped in pairs, each one traveling in a different direction, an indication of divergence and thereby of upwelling in the area. This upwelling area was diagnosed at the northwest corner of the sampled domain during the second and third survey (figures D.2 and E.5a, b). Floats 11 and 10 registered upwelling, up to 20 m/day, in that area between yeardays 281 and 282 (figure E.4c, d). The simulations done using the trajectories from floats 10/11 through the second survey reflects this upwelling, though with higher values, up to 50 m/day, than the floats' measurements. The simulation done with the same cluster and the third survey also shows upwelling, but with smaller values than the float's records.

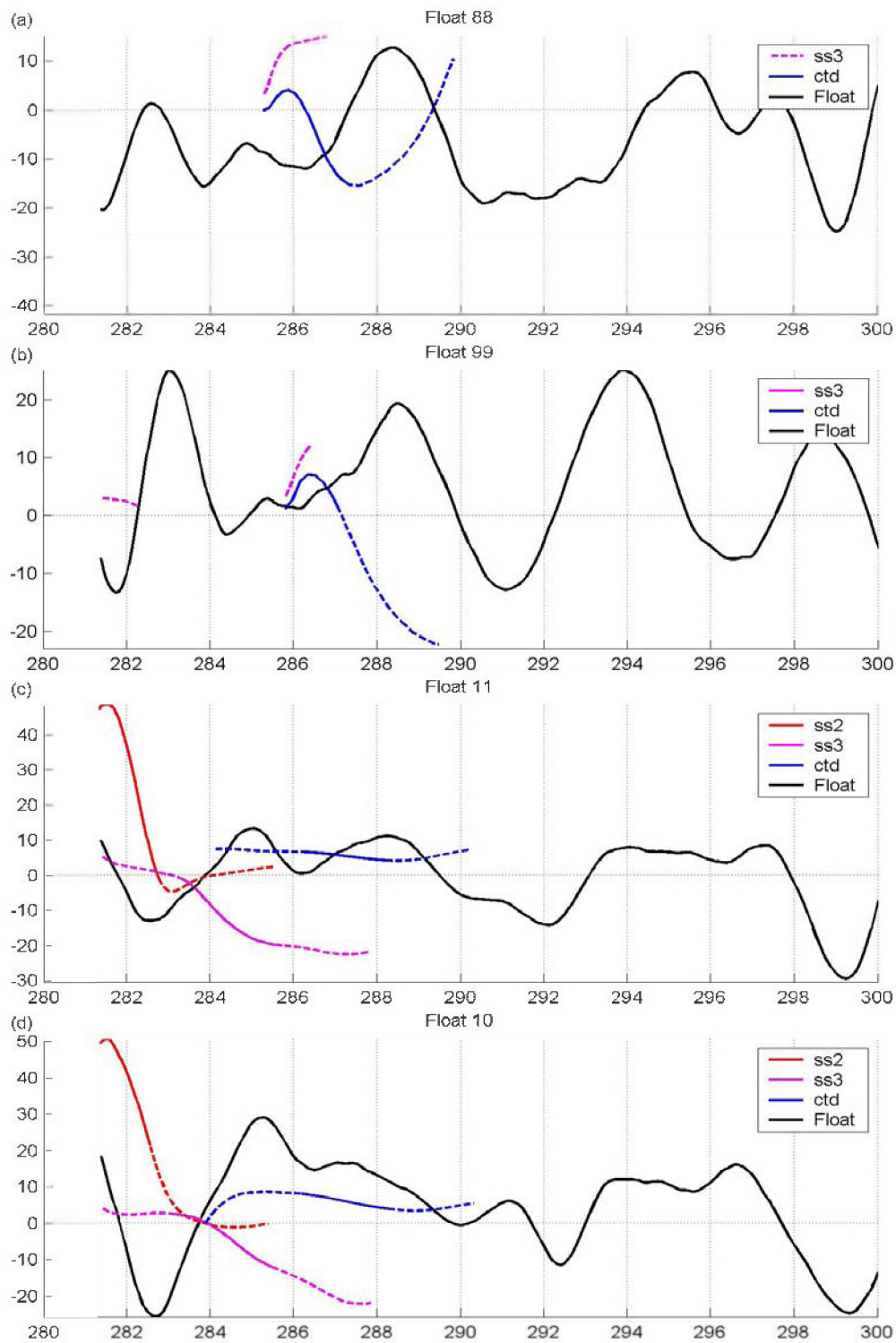


**Figure E.4.** QG diagnosed vertical velocity at the position (longitude, latitude and pressure) of float (a) 88, (b) 99, (c) 11 and (d) 10 in a time interval of 1 day (solid line) and three days (dashed line) around the float's date.

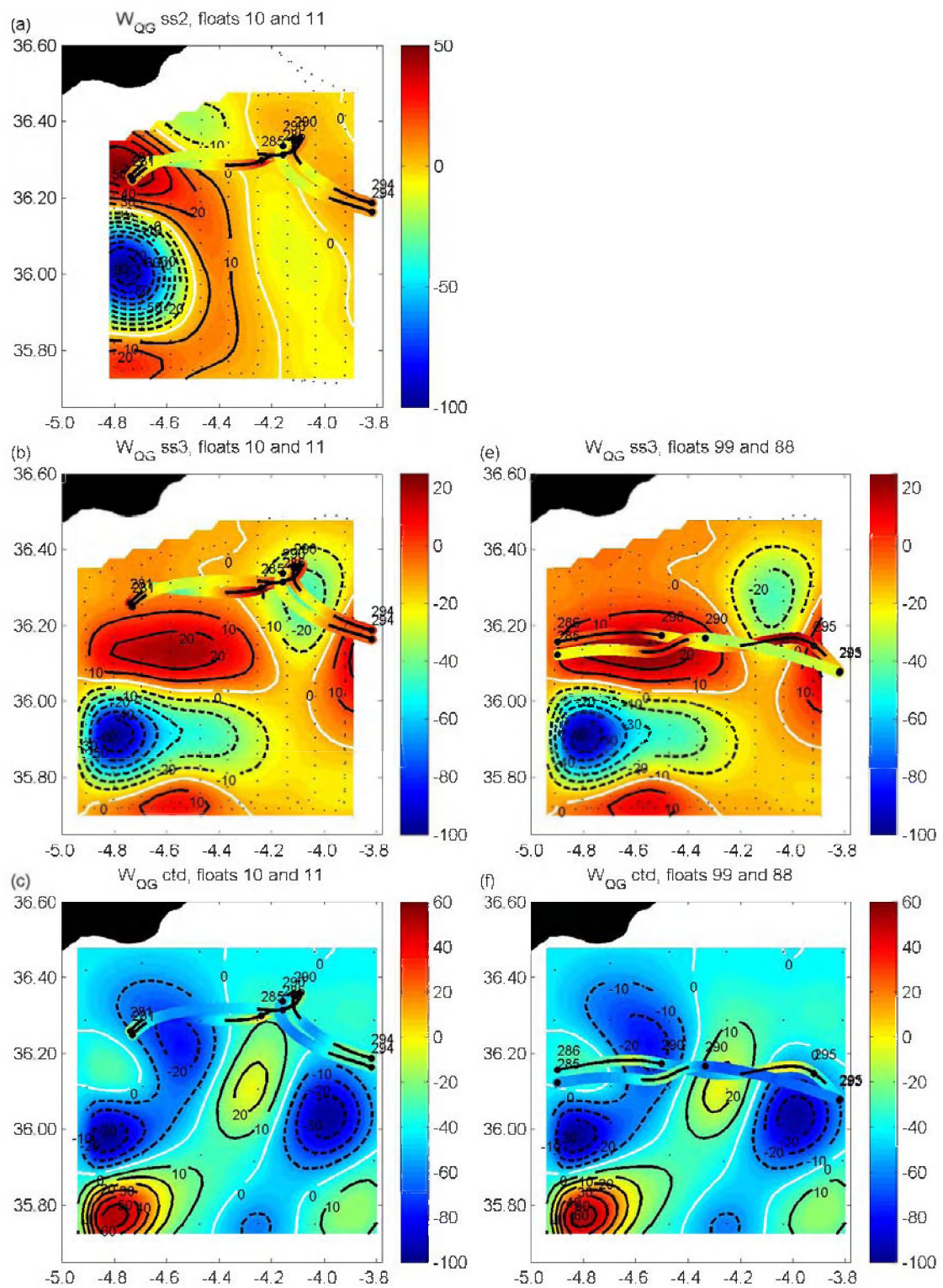


**Figure E.5.** Vertical velocities measured by the floats on top of the horizontal distributions of the QG diagnosed vertical velocity at 90 dbar. A solid line over the trajectory indicates upwelling. Dots every five days have been drawn.



The small temporal difference between the second and the third survey compared with the large difference in the simulated value using the 10/11 trajectories, point out that although the floats were able to register the correct mesoscale  $w$  value, the diagnosis from hydrographic data does not match the correct value at each particular geographical point, even though, the diagnosed velocity gives a good estimation in the area of the scale, order of magnitude, and sign of the vertical velocity field. After this upwelling patch, the cluster passed through a downwelling area, with measured values around -25 m/day at yearday 283 (Fig E.4 c, d.).

The simulations with the  $w$  obtained with the second survey revealed a decrease in the vertical velocity that only reached negative values (downwelling) for float 11 (between yeardays 282 and 284 in figure E.4 c), in spite that the timing and path for floats 10 and 11 were very similar. The simulations using the third survey, nearer in time to the measurements from floats 10/11, did not show the same tendency since the downwelling patch during this survey was eastward that during the second survey (figure E.5 b). With the fourth survey, the nearest in time to the floats' measurements, the simulations qualitatively confirm the upwelling. This cluster kept traveling eastward, remaining in an upwelling area for almost six days (between yearday day 284 and 290 in Fig E.4 c, d). The comparison has shown that there was a clear relationship between the diagnosed fields and the measurements; however, they do not exactly match the floats' measurement and the diagnosed magnitude is significantly higher than the measurement and with spatial variability at smaller spatial scales. Moreover, small changes in the trajectories or in the diagnosed fields would have increased the similarity between the floats' measurements and the computed  $w$ .

The cluster formed by floats 88/99 have few points where comparison between the diagnosed and the measured  $w$  could be done, given that after escaping from the cyclonic eddy that trapped the cluster there were only three days of coincidence between the floats and the hydrography measurements. Accordingly, the simulations have only been done for the third and fourth surveys (figures E.4a, b and E5.e, f). After

yearday day 286, float 99 recorded the upwelling patch at the northwest corner of the study area (36.2°N, 4.8°W at figE.5.e) and the simulations with the third and fourth surveys showed upwelling until yearday 287 although with higher diagnosed vertical velocities. On yearday 289, float 99 reached the maximum of this upwelling patch, to decrease the vertical velocity afterwards. The simulation done with the  $w$  determined with the hydrographic data from the fourth survey and float 99 shows a similar pattern, although the timing of the zero vertical velocity and the maximum (yearday 286 on figure 4.5.b) do not precisely match the one found in the float's measures. Simulations done using float 88 and the diagnosed fields from the third and fourth surveys (figure E.4 a, b) present similar tendency that the one described for float 99, however the coincidence between the float data and the diagnosis is weaker than for float 99.

Between floats 88 and 99 there is an offset in pressure and in vertical velocity that produces the mismatch already described. This offset in  $w$  was caused by an offset in  $w_{ROT}$  (not shown) and therefore the disagreement could be explained as consequence of the nonlinear character of the compressibility of the floats or a malfunction in the compass. A specific revision of the functioning of the floats is out of the scope of the present thesis, moreover the conclusion, presented in the next section, would not be different depending on the agreement or not of float 88's measurements.

### E.3 CONCLUSIONS

As far as we know it is the first time that floats capable of registering the full vertical velocity field have been used to compare in-situ measurements with computed vertical velocities. The floats showed an almost lagrangian behavior, with vertical displacements between the 80 and 140 dbar levels. Where direct comparison between the measured and diagnosed vertical velocity was possible, there was an agreement in the spatial and temporal scales, with a slightly overestimation of the QG diagnosis. The overall spatial and temporal scales of the vertical velocity recorded by the floats are around 25 km and 2/3 days, while the vertical excursions of the floats are about 50

$\bar{d}$ , with small net vertical displacement in the study area. All scales that characterize the measured vertical velocity field are similar to those that characterize the diagnosed fields. The range of the recorded  $w$  is slightly smaller than the diagnosed via the QG- $\omega$  equation. If the overestimation of the QG theory, and the fact that the floats only sampled the area crossed by the AJ are taken into account; the diagnosed fields are a good estimation of the real mesoscale vertical velocities. In the few spatiotemporal points where straight comparison was possible, there was little point-by-point match between the measured and the computed fields.

In summary, the diagnosed vertical velocity field gives good estimation of the scales sign and ranges of the real  $w$ , however further used of this diagnosed fields should be done with care since the particular geographical distribution do have large uncertainties.

---

## **F.-CONCLUSIONS**

---

Throughout the previous chapters, the reliability of the omega equation as an indirect method to diagnose vertical motion in mesoscale upper ocean features has been explored with the help of four surveys carried out, with unprecedented resolution and synopticity, during October 1996 in the northwestern Alborán Sea. Due to the intense hydrographic conditions found in the western Alborán Sea, this study has been an unique opportunity to test the validity of the quasi-geostrophic omega equation as a method to diagnose vertical velocities. The circulation on the western Alborán Sea was dominated by the Western Alborán gyre and the Atlantic Jet. Associated with the northern part of the WAG and the AJ, there was a density front with gradients up to  $2 \text{ kg/m}^3$  in one Rossby radius. The velocities in the Atlantic jet were above  $110 \text{ cm/s}$ , extending down to 200 dbar. The western Alborán gyre was characterized by negative vorticity, up to  $-0.6f$  at 90 dbar, while surrounding the WAG there were patches of positive and negative vorticity associated with the meandering and shear at the WAG's rim and in the AJ; the positive vorticity reached values up to  $0.5f$  at 90 dbar. The results presented in chapter B could be considered as the first time that the large-scale variability of the Alborán Sea has been related to changes in the Atlantic inflow through the Strait of Gibraltar, and that the time evolution and three-dimensional thermohaline structure of the Western Alborán Sea during a WAG migration event have been described. The main result was the description of the two necessary requirements to trigger the eastward migration of the WAG, each one associated with a different mechanism. The first one was the increase in the Atlantic inflow, that pushed the WAG eastward and that was controlled by tidal forcing since a neap tide occurred at the same time as the pulse of NACW. The second requirement was an intense decrease in the Atlantic inflow after the pulse.

In the future, we will extend the results, investigating the role that quasi-periodic mechanisms, as stochastic resonance [Vélez-Belchí *et al.*, 2001], have in the migrations of the western Alborán gyre, and therefore in the interannual variability of



the western Alborán Sea. During the Omega experiment, similar surveys to those presented here were done in the Almería-Oran front during December 1996, an exploration of the presence of NACW in that front will be done in order to characterize the geographical and temporal extension of the NACW pulses.

The frontal situation found on the northern side of the western Alborán Sea had associated strong ageostrophic circulation. The resulting vertical velocity field is a consequence of the tendency of the ocean to be in geostrophic and hydrostatic balance, for that reason the isopycnals slope by itself cannot suggest the vertical velocity distribution. The diagnosis of  $w$  in this balance has been carried out using two different techniques. The first one was the inversion of the Q-vector form of the quasi-geostrophic omega equation, the second one was the assimilation of the density field into a primitive equation ocean model. The omega equation diagnosed vertical velocities between  $-100$  m/day and  $70$  m/day, with the maximum values being found at the rim of the WAG at  $90$  dbar, where the maximum vertical density gradients occurred. The predominant lengths scales were dominated by the meandering of the WAG's rim and were similar to the local internal Rossby radius of deformation, approximately  $30$  km. Neither significant net downwelling nor net upwelling was observed, indicating a mature state of the WAG. In spite the high vertical velocities found, simulated trajectories indicated that the net vertical displacement, for those water parcels released in the interior of the WAG, was very small, less than  $5$  m/day, while net vertical displacements near  $20$  m/day was found on trajectories outside the WAG. These small net vertical motions are coherent with quasi-geostrophy, which assumes vertical displacements much smaller than horizontal displacements. It is remarkable that the main contribution to the vertical velocity field was the differential geostrophic advection of geostrophic vorticity. Confirmed by the strong correlation found between the vorticity advection and the vertical velocity; and by the small differences found, with a standard deviation for  $w_{DFI}-w_{QG}$  of approximately  $7$  m/day, between the vertical velocities diagnosed with the omega equation and those diagnosed with PE/DFI.

The vertical velocities from PE/DFI were slightly smaller, as the omega equation tends to overestimate the vertical velocity due to the lack of ageostrophic advection in the quasi-geostrophic theory. The spatial distribution of the vertical motion diagnosed with both techniques was very similar, with identical spatial scales. It can be concluded that the theoretical approach has relative small impact on the diagnosis of vertical velocities, and therefore small differences will be found if biogeochemical fluxes are computed either with the omega equation or with the assimilation into a primitive equation ocean model. Potential vorticity conservation was shown through the correspondence of geostrophic vorticity and vertical velocity along the simulated trajectories.

Mesoscale features are not the only source of vertical motion in the western Alborán Sea, since the interaction of the western Alborán gyre and the Atlantic jet with the bottom topography needs vertical motion to keep potential vorticity conserved. Simulations of the western Alborán Sea in a primitive equation ocean model are underway, in order to provide an estimation of the relative importance of both sources of vertical velocities in the area.

To diagnose dynamical variables as the described vertical velocity, high-order spatial derivatives of the observed density and geopotential fields were necessary. The uncertainties associated with both, the aliasing of unresolved scales and the discrete character of the sampling have been investigated studying the sensitivity of the vertical velocity, and the density fields, to changes in the parameters required to use optimal statistical interpolation. As a major concern for future studies, it should be taken into account that despite the density field seems to be well retrieved from the observations, the derivatives of the geopotential field are seriously contaminated by the aliasing errors due to the unresolved scales, given that the high wave components of the anomaly field are amplified in the differentiation process. It is worth saying that the inaccuracy in determining the mean field has a greater impact on  $w$ , yielding, in some cases, artificial although spatially coherent features in the vorticity and vertical velocity

fields. This arises because a non-optimal choice of the mean field produces an anomaly field that is neither stationary nor a zero-mean random function of the location. The impact of the objective analysis boundary effect on the density and the vertical velocity was tested for each survey carrying out analyses where the number of available observations was modified. The uncertainty associated with the boundary effect changes considerably depending on the dynamical conditions, increasing in critical cases, as that found during the first survey, where the maximum advection of vorticity was at the boundaries. The uncertainty due to observational and sampling error is independent of the theoretical approach used to diagnose the vertical velocities, as indicated by the fact that the vertical velocities diagnosed from the omega equation and those diagnosed from the assimilation into the primitive equation model have the same sensitivity to changes in the parameters of the OI. These results are based on a qualitative study, and it is difficult to quantitatively estimate the restrictions that the sampling and the observational errors impose when the needed parameters can not be precisely determined, but they imply some concern about the studies where balance assumptions are tested, or even in that studies where the geostrophic fields are compared with kinematics' diagnoses of horizontal velocities from observed ADCP velocities. Questioning the use of in-situ data with theoretical approaches more sophisticated than QG, at least without precise knowledge of the restriction than the sampling and the observational errors impose.

Fortunately the fact that slightly similar shapes were found throughout the sensitivity studies carried out for all the parameters needed by optimal statistical interpolation give the confidence to establish that the diagnosis, at least, allow to ascertain the order of magnitude, sign and size of the upwelling and downwelling patches.

A theoretical study of the uncertainty that an anomaly field that does not fulfill the OI requirements impose over diagnosed variables should be done. The impact of the aliasing of the unresolved scales should be verified in other areas, with different dynamical conditions. In that line, analyses similar to those effectuated here are

underway for high resolution hydrographic surveys sampled in other areas of the world' oceans.

All the work done would be uncompleted without a proper comparison of the diagnosed fields with in-situ measurements of vertical velocities; in that sense, it is the first time that floats capable of registering the full vertical velocity field have been used to compare in-situ measurements with vertical motion diagnosed from routine hydrographic surveys. The floats described a quasi-lagrangian behavior, with vertical displacements between the 80 and 140 dbar levels. In the selected float tracks where direct comparison between the measure and diagnosed vertical velocity was possible, there was agreement in the spatial and temporal scales, with slightly overestimation of the quasi-geostrophic diagnosis. The scales that characterized the measured vertical velocity fields were similar to those scales characteristic of the diagnosed fields. The overall spatial and temporal scales of the vertical velocity recorded by the floats were around 25 km and 2/3 days, while the vertical excursions of the floats were up to 50 dbar, with small net vertical displacement in the area. Furthermore, the diagnoses should be used with care, because are just a snapshot of the real world, and the time-varying structures can significantly modify the upwelling and downwelling areas, as demonstrated by the analyses of the measured vertical velocities. Therefore, quantification of any vertical transport should be done with precise knowledge of the four dimensional, space and time, velocity fields.

In summary, the most significant result obtained, put together throughout the thesis, is that the Q-vector form of the omega equation permit to diagnose correctly, from routinely observed density fields, the sign and order of magnitude of the vertical motion, as well as the characteristic spatio-temporal scales of the upwelling and downwelling patches. However, computing net vertical biogeochemical fluxes should be done with care since, in some cases, uncertainty due to the aliasing of the unresolved scales is very important.

# LIST OF TABLES AND FIGURES

## TABLES

<b>Table A.I.</b> Starting and ending dates for each survey .....	25
<b>Table B.I.</b> Maximum ADCP velocities (m/s), in the top 200 dbar at section 2, for those water parcels with salinities smaller than S. Between brackets is the maximum eastward component. ....	40
<b>Table B.II.</b> Eastward ADCP Transport (Sv), in the top 200 dbar, for those water parcels with salinities smaller than S .....	42
<b>Table B.III.</b> Percent of water parcels, in the top 200 dbar, with salinities smaller than S.....	51
<b>Table E.I.</b> Statistics of the vertical velocity measured by the floats, the value between parenthesis was calculated with the data measured while the floats were in the area covered by the hydrographic data. ....	135

## FIGURES

<b>Figure A.1.</b> Sea surface temperature (SST) for the western Alborán sea on the first day of (a) survey 1 (October 3 <sup>rd</sup> 1996), (b) survey 2 (October 6 <sup>th</sup> 1996), (c) survey 3 (October 9 <sup>th</sup> 1996) and (d) survey 4 (October 11 <sup>th</sup> 1996). The dotted contour corresponds to the 18°C isotherm, the thick contour to the 19.5°C isotherm and the dashed one to the 21°C. The track of each survey is overlaid. The circles in the westernmost section of survey 2 indicate the launching positions of the six recovered floats. The second (4.8°W) and sixth (4.36°W) sections, are indicated with a thicker line in surveys 1, 2 and 3. The geographical locations mentioned in the text are included.....	26
<b>Figure B.1.</b> Potential temperature and salinity diagram for the first survey in the 0-350 dbar range. The isolines of potential density are overlaid for reference.....	36
<b>Figure B.2.</b> Daily composites of SST from selected days, between October 1 <sup>st</sup> and November 30 <sup>th</sup> 1996. The dotted line corresponds to the 18°C isotherm, the thick line to the 19.5°C isotherm and the dashed line to the 21°C. ....	38
<b>Figure B.3.</b> Vertical meridional sections, for the first survey, of (a) $\sigma_t$ , (b) salinity and (c) temperature along 4.8°W (section 2) and (d) $\sigma_t$ , (e) salinity and (f) temperature along 4.36°W (section 6).....	41
<b>Figure B.4.</b> Horizontal distributions of (a) temperature and (b) salinity for the (ss1) first, (ss2) second, (ss3) third and (ctd) fourth survey. ....	43
<b>Figure B.5:</b> Horizontal distributions of density ( $\text{kg/m}^3$ ) at (a) 15 dbar (b) 90 dbar and (c) 200 dbar for the (ss1) first, (ss2) second, (ss3) third survey and (ctd) fourth survey. ....	45
<b>Figure B.6.</b> Horizontal distributions of geostrophic velocity (cm/s) at (a) 15 dbar (b) 90 dbar and (c) 200 dbar for the (ss1) first, (ss2) second, (ss3) third survey and (ctd) fourth survey. The 26, 27 and 28 $\text{kg/m}^3$ isopycnals are overlaid for reference. ....	47
<b>Figure B.7.</b> ADCP velocities at (a) 90 dbar and (b) 200 dbar for the (ss1) first, (ss2) second and (ss3) third survey.....	50
<b>Figure B.8.</b> Three-dimensional distribution of waters with $S < 36.35$ for the (a) first, (b) second, (c) third and (d) fourth survey. ....	52
<b>Figure B.9.</b> Trajectories of the three pairs of floats. For reference, the first survey track is overlaid. The circles and asterisks denote the following dates: 8 <sup>th</sup> , 11 <sup>th</sup> , 20 <sup>th</sup> , 26 <sup>th</sup> , 29 <sup>th</sup> October and 4 <sup>th</sup> , 7 <sup>th</sup> , 10 <sup>th</sup> November, while the dark dots are for the 8 <sup>th</sup> , 23 <sup>rd</sup> October and the 1 <sup>st</sup> November. The last data were received on November 14 <sup>th</sup> 1996 .....	54



<b>Figure B.10.</b> (a) Time series of sea level atmospheric pressure at Ceuta (solid lines) and the difference between the sea level at Ceuta and the sea level at Algeciras (dashed line). (b) Tides at Algeciras. The boxes indicate the timing of each survey. Note the different time interval covered in (b). The two thin dashed lines in (a) denote the time interval covered in (b).....	58
<b>Figure C.1.</b> Raw density data (a.n), mean field (b.n) and anomaly density field (c.n) for the first survey and polynomial of degrees $n=1, 2, 3, 4$ .....	73
<b>Figure C.2.</b> Least-squares fit of the correlation model for dynamic height in surveys (a.n) ss1, (b.n) ss2 and (c.n) ss3, where $n=1, 2$ is the degree of the polynomial used as mean field. The red line is the fitted true correlation, the black dots are the observed correlations, and the blue line is the correlations averaged throughout the water column.....	76
<b>Figure C.3.</b> Vertical velocity diagnosed at 90 dbar from analysis of dynamic height for ss1 and different values of the correlation scale: (a) $L=20$ km, (b) $L=15$ km and (c) $L=25$ ; (d) represents (b)-(a) and (e) represents (c)-(a). The other analysis parameters were kept as the optimal ones. For each map, the standard deviation and the maximum and minimum value of the represented field have been included.....	78
<b>Figure C.4.</b> Vertical velocity diagnosed at 90 dbar from analysis of dynamic height for ss1 and different values of the noise-to-signal ratio: (a) $\gamma=0.01$ , (b) $\gamma=0.2$ and (c) $\gamma=0.4$ ; (d) represents (b)-(a) and (e) represents (c)-(a). The other analysis parameters are the optimal ones. For each distribution, the standard deviation and the maximum and minimum value of the represented field have been included.....	79
<b>Figure C.5.</b> Vertical velocity diagnosed from analysis of dynamic height for ss1 and different values of the cut-off scale: (a) $\lambda_{cut-off}=20$ km, (b) $\lambda_{cut-off}=0$ km and (c) $\lambda_{cut-off}=40$ km; (d) represents (b)-(a) and (e) represents (c)-(a). The other analysis parameters are the optimal ones. For each map, the standard deviation and the maximum and minimum value of the represented field have been included.....	81
<b>Figure C.6.</b> Vertical velocity diagnosed from analysis of dynamic height for ss1 and different polynomial degree as mean field: (a) $n=2$ , (b) $n=1$ , (c) $n=3$ and (d) $n=4$ ; (e) represents (b)-(a) and (f) represents (c)-(a) and (g) represents (d)-(a). The other analysis parameters are the optimal ones. For each map, the standard deviation and the maximum and minimum value of the represented field have been included.....	83
<b>Figure C.7.</b> Analysis of density for ss1 and different polynomial degree as mean field: (a) $n=2$ , (b) $n=1$ , (c) $n=3$ and (d) $n=4$ , (d) represents (b)-(a) and (e) represents (c)-(a). The other analysis parameters are the optimal ones. For each map, the standard deviation and the maximum and minimum value of the represented field have been included.....	84
<b>Figure C.8.</b> Vertical velocity diagnosed from analysis of dynamic height for ss3 and different polynomial degree as mean field: (a) $n=2$ , (b) $n=1$ , (c) $n=3$ and (d) $n=4$ ; (e) represents (b)-(a) and (f) represents (c)-(a) and (g) represents (d)-(a). The other analysis parameters are the optimal ones. For each map, the standard deviation and the maximum and minimum value of the represented field have been included.....	87
<b>Figure C.9.</b> Vertical velocities (m/day) diagnosed from the (a.survey) complete dataset and (b.survey) a reduced dataset within the contoured region. Survey=ss1, ss2 and ss3. The standard deviation and the maximum and minimum value of the represented field have been included in each figure. ....	88
<b>Figure D.1:</b> Horizontal distributions of geostrophic vorticity, scaled by the local coriolis parameter, $(\zeta/f_0)$ at (a) 15 dbar (b) 90 dbar and (c) 200 dbar for the (ss1) first, (ss2) second, (ss3) third and (ctd) fourth surveys. ....	98
<b>Figure D.2:</b> Horizontal distributions of vertical velocity (m/day), at (a) 15 dbar (b) 90 dbar and (c) 200 dbar for the (ss1) first, (ss2) second, (ss3) third survey and (ctd) fourth surveys.....	100

<b>Figure D.3:</b> South-north sections of $w$ (m/day) along (a) $4.79^\circ\text{W}$ and $4.22^\circ\text{W}$ (b) for the (ss1) first, (ss2) second, (ss3) third and (ctd) fourth survey. The 26, 27 and 28 $\text{kg/m}^3$ isopycnals are overlaid for reference.....	107
<b>Figure D.4:</b> Horizontal distributions of vorticity advection ( $\times 10^{-9}$ ) at (a) 15 dbar (b) 90 dbar and (c) 200 dbar for the (ss1) first, (ss2) second, (ss3) third survey and (ctd) fourth survey.....	111
<b>Figure D.5:</b> Vertical profile of correlation between the vertical velocity and the vorticity advection during the first survey. ....	113
<b>Figure D.6:</b> Absolute vertical velocity (m/day), averaged over the domain, as function of the integration time (h), for the first (solid line) and the third (dashed line) surveys.....	117
<b>Figure D.7:</b> Density fields ( $\text{kg/m}^3$ ) at 100 dbar from the primitive equation model at (a) $t=-12\text{h}$ , (b) $t=0\text{h}$ and (c) $t=+12\text{h}$ . The small dots indicate the survey track.....	118
<b>Figure D.8:</b> Vertical velocity field at 90 dbar computed using the PE/DFI technique for the (a) first survey and the (c) second survey. Contour interval is 5 m/day with thick contours each 10 m/day. The thin line is the vertical velocity field computed using the QG-omega equation. The difference between the $w_{\text{DFI}} - w_{\text{QG}}$ at 90 dbar for the (b) first survey and the (d) second survey are included.....	120
<b>Figure D.9:</b> Simulated trajectories for a water parcels initially at 90 dbar for surveys (a) ss1 and (d) ss3. For reference, the dynamic height at 90 dbar is overlaid. Time series of $w$ and $\zeta_g/f$ along the trajectory for surveys (b) ss1 and (e) ss3. Net vertical displacement for the water parcels for surveys (c) ss1 and (f) ss3. The dots are drawn every 20 km.....	123
<b>Figure D.10:</b> Simulated trajectories for water parcels initially at 50 dbar (red), 150 dbar (blue) and 100 dbar (black, yellow, and magenta) for surveys (a) ss1 and (d) ss3. Net vertical displacement for water parcels initially at 100 dbar for surveys (b) ss1 and (e) ss3. Net vertical displacement for water parcels initially at 150 dbar for surveys (b) ss1 and (e) ss3.....	124
 <b>Figure E.1.</b> (a) Trajectories of the cluster formed by floats 10 and 11, the labels in the trajectories are shown every five days, beginning on October 7 <sup>th</sup> (yearday 282 in 1996). Float's pressure (dbar), (c) temperature ( $^\circ\text{C}$ ) and (d) measured vertical velocity (m/day) as function of yearday in 1996.....	131
<b>Figure E.2.</b> Same as figure E.1 but for the cluster formed by floats 88 and 99. ....	133
<b>Figure E.3.</b> Same as figure E.1 but for the cluster formed by floats 97 and 00. ....	134
<b>Figure E.4.</b> QG diagnosed vertical velocity at the position (longitude, latitude and pressure) of float (a) 88, (b) 99, (c) 11 and (d) 10 in a time interval of 1 day (solid line) and three days (dashed line) around the float's date.....	139
<b>Figure E.5.</b> Vertical velocities measured by the floats on top of the horizontal distributions of the QG diagnosed vertical velocity at 90 dbar. A solid line over the trajectory indicates upwelling. Dots every five days have been drawn.....	140

---

## REFERENCES

---

- Allen, J.T., D.A. Smeed, N. Crips, S. Ruiz, S. Watts, P.J. Vélez-Belchí, P. Jornet, O. Rius, and A. Castellón (1997), Upper Ocean underway operation on BIO Hespérides Cruise OMEGA-ALGERS (cruise 36) using SeaSoar and ADCP, *Southampton Oceanographic Centre Internal document* (17), 55 pp.
- Allen, J.T. and D.A. Smeed (1996b), Potential vorticity and vertical velocity at the Iceland-Faeroes front, *J. Phys. Oceanogr*, 26 (12), 2611-2634.
- Allen, J.T. and D.A. Smeed (1996a), Potential vorticity and vertical velocity at the Iceland-Faeroes front, *J. Phys. Oceanogr*, 26 (12), 2611-2634.
- Bakun, A. (1996), *Patterns in the ocean. Ocean processes and marine population dynamics*, California Sea Grant
- Bormans, M. and C. Garrett (1989), A simple criterion for gyre formation by the surface outflow from a strait, with application to the Alborán Sea, *J. Geophys. Res.*, 94 (C9), 12637-12644.
- Bretherton, F.P., R.E. Davis, and C.B. Fandrys (1976), A technique for objective analysis and design of oceanographic experiments applied to MODE-73, *Deep-Sea Res.*, 23, 559-582.
- Candela, J., C.D. Winant, and H.L. Bryden (1989), Meteorologically forced subinertial flows through the Strait of Gibraltar, *J. Geophys. Res.*, 94 (C9), 12667-12679.
- Cano, N. (1978), Resultados de la campaña Alborán 76, *Bol. Inst. Esp. Oceanogr.*, 3-50.
- Carlson, T.N. (1991), *Mid-Latitude Weather Systems*, Harper Collins Academic, London
- Cheney, R.E. and R.A. Doblar (1982), Structure and Variability of the Alborán Sea Frontal System, *J. Geophys. Res.*, 84 (1), 585-594.
- Chumbinho, R.P.A., (1994), Kinematics and dynamics of a cyclonic eddy off Point Arenas, PhD., Naval Postgraduate School, California
- Crepon, M. (1965), Influence de la pression atmosphérique sur le niveau moyen de la Méditerranée Occidentale et sur le flux à travers le Détroit de Gibraltar, *Cah. Oceanogr*, 1 (7), 15-32.
- Donde Va? Group (1984), Donde va?, An oceanographic experiment in the Alborán Sea., *EOS Transactions of American Geophysical Union*, 65, 682-683.
- Emery, W.J. and R.E. Thomson (1998), *Data analysis methods in physical oceanography*, Pergamon Press

- Fiekas, V., H. Leach, K.J. Mirbach, and J.D. Woods (1994), Mesoscale instability and upwelling. Part 1: Observations at the North Atlantic Intergyre Front, *J. Phys. Oceanogr*, 24 (8), 1750-1758.
- Gandin, L.S. (1963), Objective analysis of meteorological fields. *Transl. From Russian by Israel program for scientific translations (NTIS NO TT65-50007)*.
- Garabato, A.C.N., H. Leach, J.T. Allen, R.T. Pollard, and V.H. Strass (2001), Mesoscale Subduction at the Antarctic Polar Front Driven by Baroclinic Instability, *J. Phys. Oceanogr*, 311 (8), 2087-2107.
- Gascard, J.C. and C. Richez (1985), Water masses and circulation in the western Alborán Sea and in the strait of Gibraltar, *Prog. Oceanogr.*, 15, 157-116.
- Gill, A.E. (1982), *Atmosphere-Ocean Dynamics*, p. -662, Academic Press, San Francisco
- Gleizon, P., (1994), (Experimental study on the formation and the stability of anticyclonic gyres generated by baroclinic current from strait. Application to the Alborán sea). Etude experimentale de la formation et de la stabilite de tourbillons anticycloniques engendres par un courant barocline issu d'un detroit. Application a la mer d'Alborán, Ph. D., Universite Joseph Fourier, Grenoble (France)
- Gleizon, P., G. Chabert D'Hieres, and D. Renouard (1996), Experimental study of the Alborán Sea gyres, *Oceanol. Acta*, 19 (5), 499-511.
- Gomis, D., A. Pascual, and M.A. Pedder (2005), Errors in dynamical fields inferred from oceanographic cruise data - Part II. The impact of the lack of synopticity, *J. Mar. Sys.*, 56 (3-4), 334-351.
- Gomis, D. and M.A. Pedder (2005), Errors in dynamical fields inferred from oceanographic cruise data. Part I. The impact of observation errors and the sampling distribution, *J. Mar. Sys.*, 56 (3-4), 317-333.
- Gomis, D., S. Ruiz, and M.A. Pedder (2001), Diagnostic analysis of the 3D ageostrophic circulation from a multivariate spatial interpolation of CTD and ADCP data, *Deep-Sea Research*, 48 (1), 269-295.
- Haney, R.L. and R.A. Hale (2001), The use of digital filter initialization to diagnose the mesoscale circulation and vertical motion in the California coastal transition zone, *J. Mar. Sys.*, 29, 335-363.
- Heburn, G.W. and P.E.L. Violette (1990), Variations in the structure of the anticyclonic gyres found in the Alborán Sea, *J. Geophys. Res.*, 95 (C2), 1599-1613.
- Holton, J.R. (1992), *An introduction to dynamic meteorology.*, Academic Press, San Diego
- Hoskins, B.J., I. Draghici, and H.C. Davies (1978), A new look at the infinite equation, *Quartely Journal of the Royal Meteorological Society*, 104, 31-38.
- Hoskins, B.J., M.E. McIntyre, and Robertson W. (1985a), On the use and significance of isentropic potential vorticity maps, *Quartely Journal of the Royal Meteorological Society*, 111, 877-946.

- Hoskins, B.J., M.E. McIntyre, and Robertson W. (1985b), On the use and significance of isentropic potential vorticity maps, *Quarterly Journal of the Royal Meteorological Society*, 111, 877-946.
- Kinder, T.H. and H. Bryden (1987), The 1985-1986 Gibraltar experiment: data collection and numerical results, *EOS Transactions of American Geophysical Union*, 68, 786-795.
- La Violette, P.E. (1984), Aircraft and satellite measurements of surface currents and submesoscale thermal features with the Alborán Sea gyre during Donde Va?, *Informes técnicos*, Instituto Espanol de Oceanografia, Madrid.
- La Violette, P.E. (1986), Short-term measurements of surface current associated with the Alborán Sea Gyre during Donde Va?, *J. Phys. Oceanogr.*, 16 (2), 262-279.
- La Violette, P.E. (1990), The Western Mediterranean Circulation Experiment (WMCE): Introduction, *J. Geophys. Res.*, 95 (C2), 1511-1514.
- La Violette, P.E. and H. Lacombe (1988), Tidal-induced pulses in the flow through the Strait of Gibraltar., *Oceanol. Acta*, 9, 13-27.
- Lafuente, J.G., N. Cano, M. Vargas, J.P. Rubin, and A. Hernandez-Guerra (1998), Evolution of the Alborán Sea hydrographic structures during July 1993, *Deep-Sea Res. I*, 45 (1), 39-65.
- Lanoix, F. (1974), Projet Alborán. Etude hydrologique et dynamique de la Mer d'Alborán., *NATO Tech. Rep.* (66), 39 pp, Brussels.
- Leach, H. (1987), The diagnosis of synoptic-scale vertical motion in the seasonal thermocline, *Deep-Sea Res.*, 34 (12), 2005-2017.
- Lindstrom, S.S. and D.R. Watts (1994), Vertical motion in the Gulf Stream near 68 degree W, *J. Phys. Oceanogr.*, 24 (11), 2321-2333.
- Lorenz, E.N. (1992), The slow manifold- What is it?, *J. Atmos. Sci.*, 49, 2449-2451.
- Lynch, P. and X.-Y. Huang (1992), Initialization of the HIRLAM model using a digital filter, *Mon. Wea. Rev.*, 120, 1019-1034.
- Martin, A.P. and P. Pondaven (2003), On estimates for the vertical nitrate flux due to eddy pumping - art. no. 3359, *J. Geophys. Res.*, 108 (C11), 3359.
- Martin, A.P. and K.J. Richards (2001), Mechanisms for vertical nutrient transport within a North Atlantic mesoscale eddy, *Deep-Sea Res. II*, 48 (4-5), 757-773.
- McGillicuddy, D.J., A.R. Robinson, D.A. Siegel, H.W. Jannasch, R. Johnson, T. Dickeys, J. McNeil, A.F. Michaels, and A.H. Knap (1998), Influence of mesoscale eddies on new production in the Sargasso Sea, *Nature*, 394 (6690), 263-266.
- Oschlies, A. and V. Garcon (1998), Eddy-induced enhancement of primary production in a model of the north Atlantic Ocean, *Nature*, 394 (6690), 266-269.
- Parrilla, G. (1984), Situation of the anticyclonic gyre in the Alborán Sea in April 1980, *Bol. Inst. Esp. Oceanogr.*, 11 (2), 106-113.



- Parrilla, G., T.H. Kinder, and R.H. Preller (1986), Deep and intermediate Mediterranean Water in the western Alborán Sea, *Deep-Sea Research*, 33 (1A), 55-88.
- Pascual, A., D. Gomis, R.L. Haney, and S. Ruiz (2004), A quasigeostrophic analysis of a meander in the Palamos Canyon: Vertical velocity, geopotential tendency, and a relocation technique, *J. Phys. Oceanogr*, 34 (10), 2274-2287.
- Pedder, M.A. (1993), Interpolation and filtering of spatial observations using successive corrections and gaussian filters, *Mon. Weather Rev.*, 121, 2889-2902.
- Peixoto, J.P. and A.H. Oort (1992), *Physics of Climate*, American Institute of Physics, New York
- Perkins, H., T. Kinder, and P. La Violette (1990), The Atlantic inflow in the western Alborán Sea, *J. Phys. Oceanogr.*, 20 (2), 242-263.
- Pinot, J.M., J. Tintoré, J.L. Lopez-Jurado, M.L. Fernandez De Puellas, and J. Jansa (1995), Three-dimensional circulation of a mesoscale eddy/front system and its biological implications, *Oceanologica Acta*, 18 (4), 389-400.
- Pinot, J.M., J. Tintoré, and D.P. Wang (1996), A study of the omega equation for diagnosing vertical motions at ocean fronts, *J. Mar. Res.*, 54 (2), 239-259.
- Pollard, R.T. and L.A. Regier (1992), Vorticity and vertical circulation at an ocean front, *J. Phys. Oceanogr*, 22 (6), 609-625.
- Rodriguez, J., J. Tintoré, J.T. Allen, J.M. Blanco, D. Gomis, A. Reul, J. Ruiz, V. Rodriguez, F. Echevarria, and F. Jimenez-Gomez (2001), Mesoscale vertical motion and the size structure of phytoplankton in the ocean, *Nature*, 410, 360-363.
- Ross, B.B. and I. Orlansky (1982), The evolution of an observed cold front. Part I: numerical simulation., *J. Atmos. Sci.*, 39, 296-327.
- Rudnick, D.L. (1996), Intensive surveys of the Azores Front 2. Inferring the geostrophic and vertical velocity fields, *J. Geophys. Res.*, 101 (C7), 16.
- Sarhan, T., J.G. Lafuente, M. Vargas, J.M. Vargas, and F. Plaza (2000), Upwelling mechanisms in the northwestern Alborán Sea, *J. Mar. Sys.*, 23 (4), 317-331.
- Shearman, R.K., J.A. Barth, J.S. Allen, and R.L. Haney (2000), Diagnosis of the Three-Dimensional Circulation in Mesoscale Features with Large Rossby Number, *J. Phys. Oceanogr*, 300 (11), 2687-2709.
- Shearman, R.K., J.A. Barth, and P.M. Kosro (1999), Diagnosis of the Three-Dimensional Circulation Associated with Mesoscale Motion in the California Current, *J. Phys. Oceanogr*, 299 (4), 651-670.
- Siegel, D.A., D.J. McGillicuddy, and E.A. Fields (1999), Mesoscale eddies, satellite altimetry, and new production in the Sargasso Sea, *J. Geophys. Res.*, 104 (C6), 13359-13379.
- Speich, S., G. Madec, and M. Crepon (1996), A strait outflow circulation process study: The case of the Alborán Sea, *J. Phys. Oceanogr.*, 26 (3), 320-340.

- Strass, V.H. (1992), Chlorophyll patchiness caused by mesoscale upwelling at fronts, *Deep-Sea Res.*, 39, 75-96.
- Strass, V.H. (1994), Mesoscale instability and upwelling. Part 2: Testing the diagnostics of vertical motion with a three-dimensional ocean front model, *J. Phys. Oceanogr.*, 24 (8), 1759-1767.
- Tintoré, J., D. Gomis, and S. Alonso (1991), Mesoscale dynamics and vertical motion in the Alborán Sea, *J. Phys. Oceanogr.*, 21 (6), 811-823.
- Tintoré, J., P.E. La Violette, I. Blade, and A. Cruzado (1988), A study of an intense density front in the eastern Alborán Sea: The Almeria-Oran Front, *J. Phys. Oceanogr.*, 18 (10), 1384-1397.
- Vargas-Yáñez, M., F. Plaza, J. Garcia-Lafuente, T. Sarhan, J.M. Vargas, and P. Velez-Belchi (2002), About the seasonal variability of the Alborán Sea circulation, *J. Mar. Sys.*, 35 (3-4), 229-248.
- Vélez-Belchí, P., J.T. Allen, and V.H. Strass (2002), A new way to look at mesoscale zooplankton distributions: an application at the Antarctic Polar Front, *Deep-Sea Res. II*, 49 (18), 3917-3929.
- Vélez-Belchí, P., Tintoré, J, Haney, R. L., and Allen, J. T. (1999), Observations and diagnostic modelling of three-dimensional fields in an upper ocean front, in *31st International Liège Colloquium on Ocean Hydrodynamics*, Three-dimensional ocean circulation: Lagrangian measurements and diagnostic analyses.
- Vélez-Belchí, P. and J. Tintoré (2001), Vertical velocities at an ocean front, *Scientia Marina*, 65, 291-300.
- Vélez-Belchí, P.J., A. Alvarez, P. Colet, J. Tintoré, and R.L. Haney (2001), Stochastic resonance in the thermohaline circulation, *Geophys. Res. Lett.*, 288 (10), 2053-2056.
- Vélez-Belchí, P.J., N.A. Crisp, A. Castellón, M.C. Hartman, and J.T. Allen (1997), Underway observations of Mean Volume Backscatter Strengths (MVBS) from the SIMRAD EK500 echosounder and shipboard ADCP during BIO Hespérides Cruise 36., *Southampton Oceanographic Centre Internal Document* (28), 86 pp.
- Vélez-Belchí, P.J., M. Vargas-Yáñez, and J. Tintoré (2005), Observation of a western Alborán gyre migration event, *Prog. Oceanogr.*, 66(2-4), 190-210, doi:10.1016/j.pocean.2004.09.006.
- Viúdez, A. and R.L. Haney (1998), The deflection and division of an oceanic baroclinic jet by a coastal boundary: A case study in the Alborán Sea, *J. Phys. Oceanogr.*, 28 (2), 289-308.
- Viúdez, A., R.L. Haney, and J. Tintoré (1996a), Circulation in the Alborán Sea as determined by quasi-synoptic hydrographic observations. Part 2: Mesoscale ageostrophic motion diagnosed through density dynamical assimilation, *J. Phys. Oceanogr.*, 26 (5), 706-724.
- Viúdez, A., J.M. Pinot, and R.L. Haney (1998), On the upper layer circulation in the Alborán Sea, *J. Geophys. Res.*, 103 (C10), 21653-21666.

- Viúdez, A., J. Tintoré, and R.L. Haney (1996b), Circulation in the Alborán Sea as determined by quasi-synoptic hydrographic observations. Part 1: Three-dimensional structure of the two anticyclonic gyres, *J. Phys. Oceanogr*, 26 (5), 684-705.
- Williams, R.G. and M.J. Follows (1998), Oceanography - Eddies make ocean deserts bloom, *Nature*, 394 (6690), 228-229.